NOVEL *IN SITU*-GELLING, ALGINATE-BASED COMPOSITES FOR INJECTABLE DELIVERY: TUNING MECHANICAL AND FUNCTIONAL CHARACTERISTICS

A Dissertation

by

JASON RICHARD ROBERTS

Submitted to the Office of Graduate and Professional Studies of
Texas A&M University
in partial fulfillment of the requirements for the degree of

DOCTOR OF PHILOSOPHY

Chair of Committee,	Michael J. McShane
Committee Members,	Kenith E. Meissner
	Melissa A. Grunlan
	Alison C. Rice-Ficht
Head of Department,	Gerard Coté

August 2014

Major Subject: Biomedical Engineering

ABSTRACT

The development of fully-implantable therapeutic and diagnostic devices represents a new paradigm in biomedical device design. However, designing materials that can perform as injectable matrices for the delivery of sensing and therapeutics chemistries while retaining control over sensor and drug release behaviors is a complex problem. The novel material described herein, microporous alginate composite (MPAC), allows for controllable *in situ* gelation—and hence enables injection—as well as encapsulation of functional elements such as sensing chemistries or therapeutics. As this material has never been described before, individual component materials, bulk mechanical and gelation properties, and sensing composite response characteristics were examined.

The use of polyelectrolyte multilayers (PEMs) in fabrication of MPACs resulted in a porous composite in which macromolecules and nanoparticles were retained within the pores, while allowing for free movement of these materials. Entrapped enzyme molecules were shown to react with diffusing substrates from outside the matrix, confirming the ability of materials from within the pores to interact with small molecules in the local environment.

Increasing numbers of PEMs used in composite fabrication was found to result in increased gelation times of hydrogels, while increasing particle concentration reduced gelation times. Changes in pH during MPAC gelation was also dependent on microsphere concentration and PEM numbers. After gelation, MPAC hydrogels

immersed in water displayed complex swelling and stiffening behavior dependent on particle concentration and PEM numbers.

Oxygen-sensing MPAC hydrogels displayed minor PEM-dependent behavior, while glucose-sensing MPAC hydrogels displayed strong dependence on concentration and PEM numbers. As concentrations increased, sensitivities increased and analytical ranges decreased indicating cooperative behavior among enzyme-containing pores. Utilizing low permeability nanofilms, sensitivities and ranges of sensors could be modulated based upon the number of layers used in fabrication.

The development of this new composite system architecture permits an added level of control over injectable hydrogel physical and functional properties such as gelation time and sensor response characteristics. This added control could broaden the usage of alginate as an injectable material and lead to the development of a wide variety of new functional injectable devices.

DEDICATION

I would like to dedicate this work to my soon-to-be wife, Vi, for all her patience and support throughout my undergraduate and graduate school career.

ACKNOWLEDGEMENTS

Firstly, I would like to thank my committee chair, Dr. McShane, and my committee members, Dr. Meissner, Dr. Grunlan, and Dr. Rice-Ficht, for their guidance and support throughout the course of this research.

Secondly, I would like to acknowledge and thank my friends and colleagues Brad Collier and Ashvin Nagaraja for their assistance and contributions to my/our work over the years. I would also like to acknowledge my colleagues in lab, without whom my research experience would be less rich: Rachel Unruh and Sulolit Pradhan from Mike McShane's lab as well as my colleagues from Profusa Scott Nichols and Becky Gant.

In addition, I would like to acknowledge two contributors to this dissertation work. Firstly, I acknowledge Jeffery Raymond for his guidance in the analysis of dynamic mechanical testing of MPAC hydrogels. Secondly, I recognize a spectacular undergraduate student, Allen Liu, for contributing preliminary work towards the development of SERS-based sensing MPACs, which is a future direction for MPAC sensors.

Finally, I would particularly like to acknowledge my colleague, business partner, and friend, Dustin Ritter, for contributing to this dissertation topic, promoting creativity in our collaborative research, and inspiring us all to be better researchers.

TABLE OF CONTENTS

LIST OF FIGURES

Page

LIST OF TABLES

1. INTRODUCTION

Chronic disease can be defined as a persistent state of disease that continues despite (or as a cause of) the body's attempts to regulate itself. In many cases, these conditions can be controlled, but are usually not curable. Due in part to the advances of medical science in the treatment of conditions resulting from infectious diseases, increased life expectancies, and the epidemic levels of obesity and sedentary lifestyles, chronic disease has become the major contributor to health concerns among the world's population.[1] In the United States alone, chronic diseases represent over 75% of healthcare costs and are the leading cause of death and disability.[2]

Treatment of these conditions has been notoriously difficult, as the underlying mechanisms of the diseases are extraordinarily complex and not yet fully understood. As of yet, pharmaceutical techniques, which classically have involved the administration of small-molecule therapeutics in pill form, have been insufficient to control these diseases or completely reduce the associated risks. As such, there has been a large drive to develop new approaches utilizing biomedical technology in place of, or in combination with, pharmaceutical therapeutics. The advent of certain technologies, namely nanotechnology and specially-designed biocompatible biomaterials, has accelerated the development of treatments by providing a wide range of new mechanistic tools for scientists and doctors to utilize.[3-6] Biomedical approaches utilizing these tools aim to improve the lives of people suffering from chronic disease by either directly

curing the diseases themselves or controlling the disease state to minimize or eliminate the negative effects of the disease on the person and their body.

While there are many biomedical strategies for combating chronic disease, certain approaches have the potential to improving outcomes. Two such examples include the continuous monitoring of bioanalytes for predictive/adaptive treatment and the controlled local delivery of therapeutics. Although these two management/treatment strategies can be implemented separately, the two approaches could, in principle, be coupled together in a fully-implantable device to improve outcomes beyond what could be achieved with an individual approach alone. In either case, sensing chemistry and/or therapeutics must be delivered to the site of interest in a minimally-invasive, controllable manner where they can reside for an extended period of time to perform their function. Fully implantable materials administered *via* injection offer a means to accomplish this.

Injectable systems must be tailored to their specific applications, and control over mechanical and functional properties of the system is crucial to their success. For continuous sensing applications, sensing molecules within an injectable system must be able to be encapsulated within it, retained during the lifetime of the sensor, and allowed to access the surrounding body fluid or tissue in a manner which allows for precise, accurate measure of the analyte of interest within the range of values expected *in vivo*. For therapeutic delivery, the system must be able to encapsulate and release therapeutic elements in an effective manner (controlled release). Control over these functional properties can be accomplished by altering bulk material properties in systems comprising a single function. However, when multiple functional elements are

combined into a single system, changing bulk material properties can affect the function of all elements contained within. Therefore, in designing multifunctional systems for sensing and/or therapeutics delivery, it is desirable to have additional tools/mechanisms for *independent* modulation of the system's functional characteristics.

To address the need for a tunable injectable system with sensor and therapeutics delivery capability, a novel composite system combining the tunable properties of polyelectrolyte nanofilms with the biocompatible nature of hydrogels was proposed. This dissertation work describes the preliminary development and characterization of this platform technology: one that can be utilized for the monitoring of analytes and delivery of therapeutics at sites of interest with easily tunable properties that could be tailored for a variety of applications. This material results from the mixing of the biomaterial alginate along with nanofilm-coated $CaCO_3$ particles and the acidifier glucono-δ-lactone. The combination of these materials forms in a hydrogel composite with nanofilm-coated microdomains, where encapsulated material is selectively retained or released. As this composite material has never before been evaluated, independent but related studies investigating the physical and functional attributes of the material were performed for the purpose of providing a basis for its further use in multimodal and/or multifunctional applications.

The content of this dissertation has been organized in a way to best explain the development and characterization of the material from inception to functional evaluation with a focus on the effects of tunable fabrication parameters. After a brief overview of relevant background information in Section 2, subsequent Sections (3-5) represent

separate publication material with focus on respective aspects or functions of the composite material. Section 3 describes the initial functional evaluation of the composite, with a focus on the fundamental system design requirements including encapsulation of materials, morphological characterization, and basic interactions with external analytes. Portions of the work in this section were published in *Journal of Materials Chemistry B*.[7] Section 4 describes the physical and mechanical characterization of the composite material, including gelation kinetics, mechanical properties and mechanical stability as a function of nanofilm architecture and particle concentration (porosity). Section 5 describes the characterization of sensor composites including oxygen and glucose-sensing constructs. This section describes the tuning of sensor response characteristics utilizing composite fabrication parameters of porosity and nanofilm architecture. Finally, Section 6 describes the future direction of the work, including progression of the material into a multifunctional and/or multimodal sensing platform, as well as its initial *in vivo* evaluation. Preliminary work with additional functional composites including model therapeutic delivery and RAMAN-sensitive chemistry are discussed.

2. BACKGROUND*

In the field of biomedical engineering, the use of hydrogels is ubiquitous. Hydrogels, which are three-dimensional, hydrophilic, polymeric networks capable of imbibing large amounts of water or biological fluids, have had a long and impactful history in biomedical engineering since their first appearance.[8-10] In recent years, interest has shifted to *in situ*-gelling hydrogels for biomedical implants over other implantable hydrogels due to the numerous advantages such systems can offer, such as minimized invasiveness and cost (Figure 1).[9, 11-14]

2.1 Injectable hydrogel materials

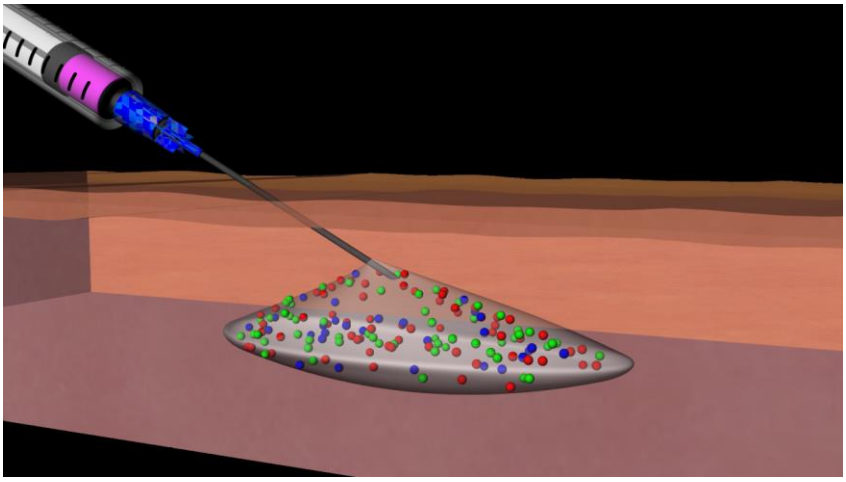

Figure 1: An *in situ*-forming hydrogel material injected under the skin.

*Parts of this section have been reprinted from J. R. Roberts, D. W. Ritter and M. J. McShane, *Journal of Materials Chemistry B*, 2013, **1**, 3195-3201 – Reproduced by permission of The Royal Society of Chemistry.

Injectable hydrogel materials, and more specifically *in situ*-gelling materials, are injected in liquid form to the site of interest, allowing the material to form to the environment. After placement, a stimulus is provided to cause the material to transition into a gel state. There have been many approaches to *in situ*-gelling systems, involving a variety of different materials and gelation stimuli.

2.1.1 Covalently crosslinked materials

Many hydrogel systems comprise synthetic polymers such as poly(hydroxyethyl methacrylate), poly(ethylene glycol), poly(vinyl alcohol) or other methacrylate-containing monomers and crosslinkers.[15-17] Classically, these systems have utilized chemical reactions such as free radical polymerization or other chemical mechanisms to control crosslinking/stiffening of the hydrogel material. While these systems' gelling kinetics are proven reliable and robust, they can have drawbacks as injectable systems because they can have toxic/immunogenic monomers and degradation products, free radical production, or the need for UV radiation.[18] As a result, many groups have worked on creating *in situ*-forming hydrogels from synthetic polymer or synthetic/natural blend materials that do not require excessive heat, damaging UV radiation and that do not produce toxic byproducts. There have been several approaches to creating such materials under mild conditions, including Michael-type Addition,[19-26] disulfide bond formation,[27-29] Schiff base formation,[29-32] and more recently, Click chemistry[33-35] and enzymatic-mediated crosslinking.[36] These methods benefit from the much stronger covalent bonding formed during crosslinking, which can increase the strength of the hydrogels and increase the retention time of the polymer in the site of

interest. Additionally, though the gels must be limited to certain functional groups for chemistries to function, there are nearly infinite numbers of monomer/polymer combinations that could produce a wide variety of materials. However, making small changes in monomer/polymer structure or monomer ratios can have dramatic impact on the gel physical structure that can be difficult to predict and optimize. This has led to the excruciatingly slow iteration of formulation testing with polymeric biomaterial systems.

2.1.2 Physically crosslinked materials

Parallel to research in covalent crosslinked systems, investigators have looked to systems utilizing physical crosslinking mechanisms, in which hydrogels are held together by non-covalent interactions and no chemical reactions take place during gelation. These interactions can include, but are not limited to, electrostatic, ionic, stereocomplexation, hydrophobic, or other chemical interactions that can be modulated by temperature, pH, or ionic strength.[9, 18] Physically-gelled hydrogels have some significant advantages over covalently-crosslinked hydrogels including biocompatibility and mild formation conditions.[18] However, the materials that can be utilized are significantly more limited due to their chemical complexity. These systems, such as peptide gels, extracellular matrix analogs, and special synthetics, can be induced to gel by temperature,[37-40] ionic/electrostatic interactions,[41-43] or hydrophobic interactions.[44, 45]

Of physically crosslinking hydrogels, investigators have a renewed interest in natural materials such as the polysaccharides alginate, pectin and chitosan due to their unique physical properties and biocompatibility as well as their low cost and sustainable production.[46-48] These materials can be stimulated to gel with exposure to ionic species,

with calcium-gelled alginate in particular seeing widespread use.[7, 49-78] However, the gelation rate of these materials has been notoriously difficult to control due to the rapid diffusion of ionic crosslinking species through their hydrophilic matrices.[68, 79] For these materials to function as an *in situ*-gelling system, the gels must either be exposed to large amounts of crosslinking ions in the environment in which they are injected or the transport/production of ionic crosslinkers to/in the pregel must be slowed as to prevent gelation prior to implantation. For alginate, this presents an obstacle as there are very low levels of calcium ions in body fluid and there is little in the way of control of ion transport within the alginate itself, short of lowering the concentration of ions, which limits the hydrogel's overall mechanical strength.[80]

As of yet, there have not been any mechanistic advances since the development of internal gelation that have allowed for ionically-crosslinked materials such as alginate to be used as a true *in situ*-gelling material. The proposed composite material solves the current problems with injectable ionically-crosslinked materials by utilizing polyelectrolyte multilayers to slow the delivery of crosslinking ions to the matrix, allowing for the composite to stay in liquid form for longer, permitting injection of the material. This advance could allow for the development of a variety of different functional materials based utilizing the advantageous properties of natural biomaterials.

2.2 Alginate and other naturally-derived materials

Alginate, pectin, chitosan, collagen, and gelatin represent just a few of the natural biomaterials being utilized in biomedical research.[25, 29, 47, 53, 59, 70, 81-88] These materials have distinct advantages over synthetic materials in a variety of ways. Primarily, these

materials resemble extracellular matrix, and so generally have good biocompatibility.[76] In addition, the gelation of these materials can be done under extremely mild conditions, allowing for minimal adverse effects on surrounding tissue and allowing for the encapsulation of whole cells for tissue engineering or tissue transplantation.[54, 83, 89, 90]

2.2.1 Naturally-derived materials

Naturally-derived materials are simply materials produced by organisms or modified directly from such materials. Some examples of these materials include alginate (harvested from various seaweed species), pectin (harvested from plant species), and gelatin (harvested from animal species). Many of these substances serve as or resemble native extracellular matrix for the organisms that produce them, and so have comparable properties to human extracellular matrix materials, and generally have favorable biocompatibility when purified properly. [41, 70, 91, 92]

2.2.2 Alginate

One well-studied bulk encapsulation material is the biomaterial alginate, a linear polysaccharide consisting of the negatively-charged sugars β-D-mannuronate and α-L-guluronate (Figure 2).[93, 94]

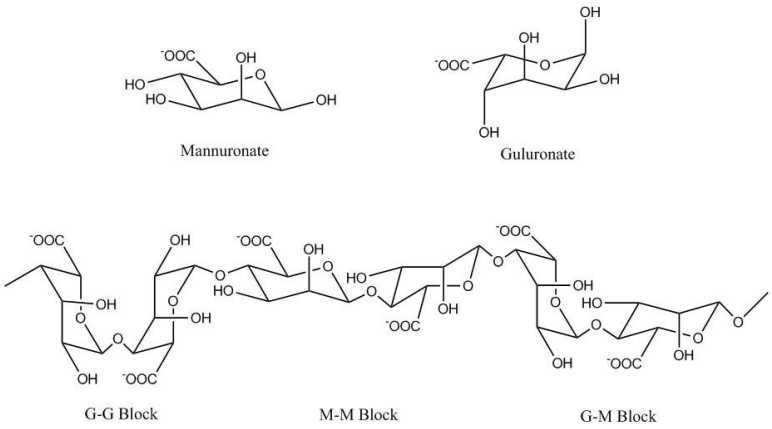

Figure 2: Structure of alginate comprising mannuronate and guluronate residues in random fashion.

Alginate is derived from several different seaweed species, and serves as extracellular matrix, protective coating, and energy storage for the algal cells.[78, 95] Depending on the organism, alginate can be a variety of molecular weights and compositions, though alginate varieties will only contain mannuronate and guluronate moieties.[57, 96] These negatively charged moieties allow for alginate to form a hydrogel in the presence of divalent cations such as calcium, barium, strontium, *etc.*[96, 97] Guluronic acid blocks are generally accepted as the groups primarily responsible for the divalent ion crosslinking of the macromolecular units and the hydrogel formation.[96] Guluronic acid groups form an "egg box" structure around divalent cations, physically linking two alginate chains together (Figure 3).[98-100]

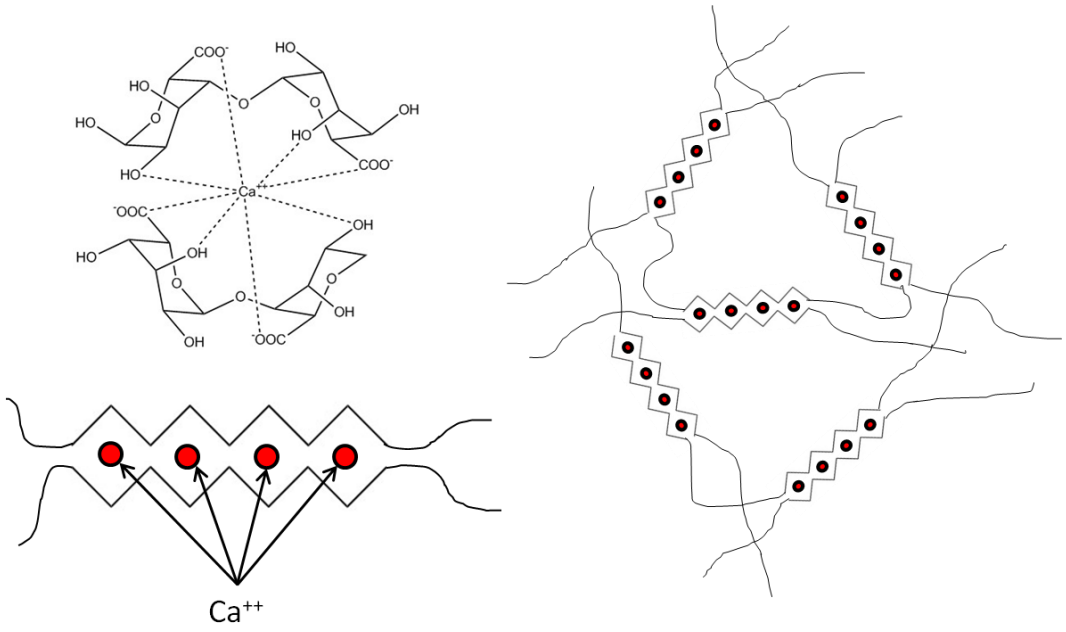

Figure 3: Alginate physical crosslinking by calcium ions. Guluronic acid blocks associate with calcium ions to form the "egg box" structure.

Higher quantities of guluronic acid groups within an alginate result in stronger hydrogels when exposed to divalent cations and have increased stiffness.[71] Mannuronic acid moieties can associate with divalent cations, but the interaction is much weaker. Mannuronic acid moieties are more labile than guluronic acid moieties, and so serve as a plasticizing element within the hydrogel.[71]

Alginate hydrogels have many attractive physicochemical properties, such as relatively high mechanical strength, high water content, and gel formation under mild conditions.[50, 58, 71, 72, 101, 102] Additionally, the biocompatibility of purified alginate hydrogels has generally been shown to be very high, though there remains an ongoing investigation into the many factors affecting the material's biocompatibility (*e.g.*, purification process, mannuronic-guluronic acid ratio, *etc*).[54, 66, 91, 92, 103, 104] Due to the

numerous advantageous properties of alginate, there has been great interest in the material for a wide variety of biomedical applications.

2.2.3 Gelation mechanisms and strategies

Alginate gelation simply requires the presence of divalent cations. However, the delivery and diffusion of the divalent cations has a dramatic impact on the gelation kinetics and the resulting hydrogel physical structure. Most alginate gels have historically been gelled by what is referred to as "external gelation" in which a solution containing a soluble divalent cation salt is put into contact with a sodium alginate-containing solution (Figure 4, left).[57, 76, 78, 105-108]

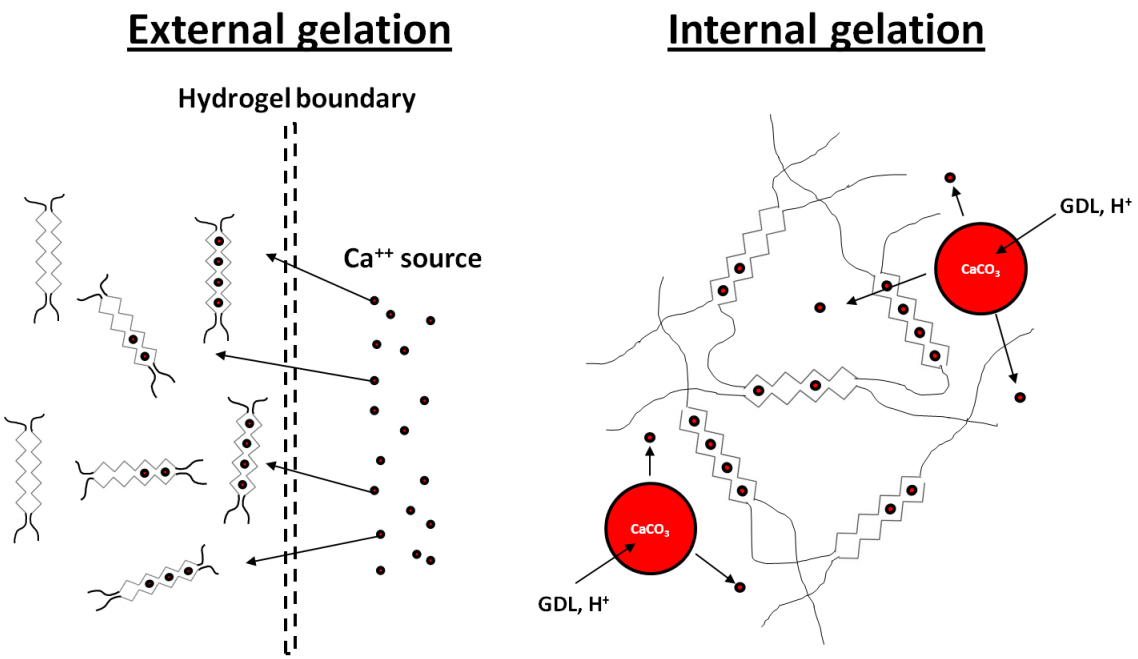

Figure 4: Mechanisms of alginate gelation. Left: External gelation by addition of calcium ions externally. Right: Internal gelation utilizing $CaCO_3$ and GDL in a well-mixed suspension.

In this case, diffusion of ions into the alginate matrix is the primary driver behind gel crosslinking. The divalent cations cross the hydrogel-solvent boundary and interact with the exterior of the alginate first. This interaction results in organization of the hydrogel-solvent boundary and a heavy local crosslink density.[105] As the cations diffuse into the hydrogel, there are fewer G-blocks available for crosslinking due to their occupation at the boundary, and therefore lower crosslink densities.[105] Overall, this process results in a non-homogenous gel, with stronger exterior regions and much softer inner regions and an overall lower smechanical strength.[105] However, in systems such as micro and nanospheres, the hydrogel-solvent boundary represents nearly the entire volume of the hydrogel, and so this is an effective method for creating micro and nanogels.[83, 107, 109, 110]

More recently, alginate has been gelled using a technique referred to as "internal gelation." In this method, insoluble divalent cation salts, such as $CaCO_3$ and $CaSO_4$ are mixed with alginate.[68] As a result of their low solubility, the salts cannot crosslink the hydrogel alone. A secondary reagent, glucono-δ-lactone (GDL) is added to the mixture to begin the gelation process (Figure 4, right). The GDL is an acidifier, and hydrolyzes in water to become gluconic acid. The acidification of the solution increases the solubility of the salts, and releases the ions into the environment. Due to the salts being well mixed into the alginate matrix, the release of ions into the alginate happens through the hydrogel volume. This results in a much stronger and more homogenous hydrogel overall.[68] It is important to note that this method depends upon many processes including the hydrolysis of GDL, diffusion of GDL, dissolution of insoluble salts and

diffusion of ions after dissolution. As such, control over these processes, such as temperature modulation, buffering effects, or diffusional changes could affect the gelation behavior.

2.3 Layer-by-layer deposition

Layer-by-layer (LbL) self-assembly has been used in a variety of applications to control diffusion of solutes and modify surface interfacial properties.[111-116] LbL films can be deposited onto a substrate—ranging in size and geometry from large planar substrates to micro- or nanoparticles—*via* a repetitive process of adsorption of interacting species, such as oppositely-charged polyelectrolytes.[117] The resulting multilayers can be manufactured in a controllable manner with respect to their physical and functional characteristics (*e.g.*, thickness, permeability, and interfacial properties), making them useful in biomedical applications such as bionanoreactors,[118] nanofiltration,[114, 115] drug delivery,[119-121] and biosensors.[122-125]

2.3.1 Electrostatic adsorption

Electrostatic adsorption refers to a layer-by-layer deposition technique that involves the deposition of alternatively charged polymers onto a substrate.[117] In this process, a substrate, which could be a variety of geometries, is exposed to a polyelectrolyte solution (Figure 5).

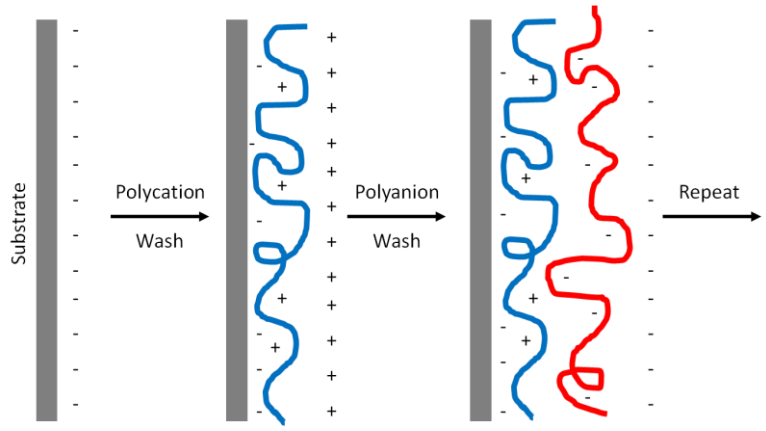

Figure 5: Layer-by-Layer adsorption of polyelectrolytes by electrostatic interactions.

The polymer chains in the solution will adsorb to the surface *via* charge interactions and will continue to adsorb until the changing surface charge leads to repulsion of additional polymer.[117] The substrate can then be washed and exposed to oppositely charged polymers, which adsorb to the coated substrate surface in a similar fashion. This process can be repeated until the desired number of layers are deposited. The process is self-limiting, and so can be done in a predictable and repeatable fashion for many cycles.[117] Control over polymer types, charge density, layer numbers and salt concentrations are a few of the parameters that can be modulated to control the thickness, permeability and interfacial properties of the films, allowing for a great variety of different film architectures and characteristics.[112, 115, 116, 122, 123, 126-131] Diffusion control of substances throught the nanofilms is of particular importance to a variety of applications. The ability to tune the permeability of nanofilms has lead to widespread interest in their use in drug delivery devices and as sensor coatings.[128, 132-134]

2.3.2 Calcium carbonate-based capsules

Calcium carbonate is a insoluble calcium salt formed spontaneously by the combination of Na_2CO_3 and $CaCl_2$ in aqueous media. Microspheres of $CaCO_3$ can be manufactured in a facile manner by controlling the relative concentrations of the precursor salts as well as the temperature of precipitation.[135, 136] In addition, material present in the precipitation solution can be co-precipitated with the $CaCO_3$ and therefore entrapped within the $CaCO_3$ microspheres.[137] This process is mild, and can be utilized to encapsulate small and large molecules as well as well as nanoparticles.[7, 134, 138, 139]

Due to the ease of manufacture and the naturally charged surface, LbL has been widely used in conjunction with $CaCO_3$ microspheres to form microcapsules (Figure 6).[131, 139-146] PEMs are deposited onto the $CaCO_3$ surface, and once the desired number of layers has been deposited, the $CaCO_3$ core can be dissolved in a slightly acidic solution or with a calcium-chelating agent to form a capsule. A high degree of control over the physical and functional properties of the microcapsules can be achieved; capsule size, thickness, permeability, and interfacial interactions can all be *designed* by choosing the appropriately-sized $CaCO_3$ template and materials, as well as controlling the deposition conditions (*e.g.*, salt concentration, pH, *etc.*), number of layers, and the appropriate terminating layer.

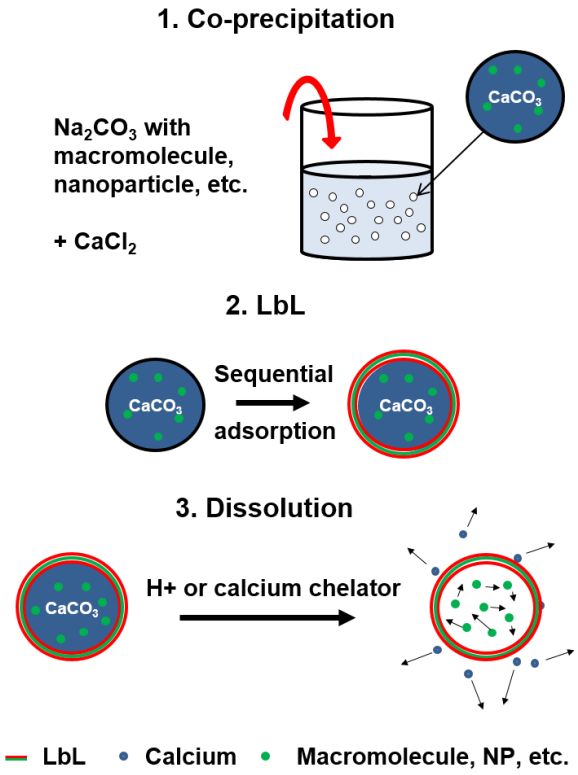

Figure 6: Sequential steps for fabrication of $CaCO_3$ capsules containing molecules or particles of interest.

While encapsulation of materials in $CaCO_3$-based capsules and some steps towards their use in drug delivery and sensing devices have been explored,[143, 145-149] usually, these nano-engineered constructs are used or studied as suspensions or, in some cases, immobilized onto another surface. However, little work has been done towards integrating these units into larger-scale bulk materials to form complex composites with added functionality.[150]

2.4 Applications of injectable materials: optical oxygen and glucose sensing technologies

Oxygen and glucose represent important analytes of interest in the diagnosis and continuous monitoring of chronic conditions such as peripheral vascular disease and diabetes mellitus.[151-155] In particular, diabetes is an area which has great need for the development of continuous monitoring technologies. In the management of diabetes, measuring levels of glucose can aid patients and their physicians in making treatment and lifestyle decisions that can better keep blood glucose within normal levels. Better control over glucose levels has been shown to reduce the occurrence of and/or minimize the long-term side effects associated with diabetes.[156, 157] Current state of the art for glucose monitoring in people with diabetes involves either *ex vivo* measurement *via* point-of-care devices or transcutaneous devices such as continuous glucose monitoring systems (CGMS). Point-of -care devices, due to their discrete sampling, do not provide the resolution required to determine important changes in analyte levels on a relevant time scale. As a result, long-term side effects of prolonged glucose imbalance, such as retinopathy and kidney disease, can occur.[157] In contrast, transcutaneous devices provide a way to monitor analyte levels *continuously*, but suffer from inaccuracy and short functional lifetimes due to the continuous inflammatory response to the probe.[158] As a result, there has been significant interest in the development of alternatives in the form of *fully-implantable* continuous monitoring systems for minimally-invasive measurement of glucose.[159]

Optical sensing of these analytes has many advantages in particular over electrochemical sensing, especially in the case of fully-implantable sensors.[160, 161] Optical sensing technologies offer a means to interrogate resident sensing chemistries *in vivo*, with no requirement for physical connection external to the body. This advantage allows for the development of sensors which can be fully implantable, as visible to IR light can travel through tissue with minimal impact on the tissue itself.[162] While there are many optical glucose sensing methods, the one which will be the focus of this discussion is based upon oxygen-sensitive phosphors, which alone can serve as optical oxygen sensors and have been used to measure oxygen levels *in vivo*.[163-165]

2.4.1 Luminescence lifetime and oxygen sensing

Luminescence lifetime is the measure of the average dwell time of a luminophore's electrons in a excited state before their return to ground state and concurrent release of photons.[166] Phosphors in particular have relatively long lifetimes when compared to organic fluorophores. Due to the long residence times, the phosphor can be collisionally quenched by oxygen, which interacts with the dye molecule within the same time scale as the electron residence time.[166] In these cases, the phosphorescence lifetime or intensity can be directly related to the oxygen concentration by the Stern-Volmer equation (1), where τ and I are the measured phosphorescence lifetime and intensity respectively, τ_0 and I_0 are the phosphorescence lifetime and intensity at zero oxygen concentration respectively, and K_{SV} is the Stern-Volmer constant, which is specific to the system.[166]

$$(2.1) \quad \frac{\tau_0}{\tau} = \frac{I_0}{I} = 1 + K_{sv} \cdot [O_2]$$

Oxygen sensing-phosphors can be incorporated into a variety of materials, but the K_{SV} of the material will be altered based upon the nature of the interaction between the phosphor and quencher.[166]

2.4.2 Enzyme-based systems for glucose sensing

Highly-specific optical glucose sensors have been developed by McShane *et al*. utilizing the enzyme glucose oxidase along with a long-lifetime oxygen-sensitive phosphor (Figure 7).[132]

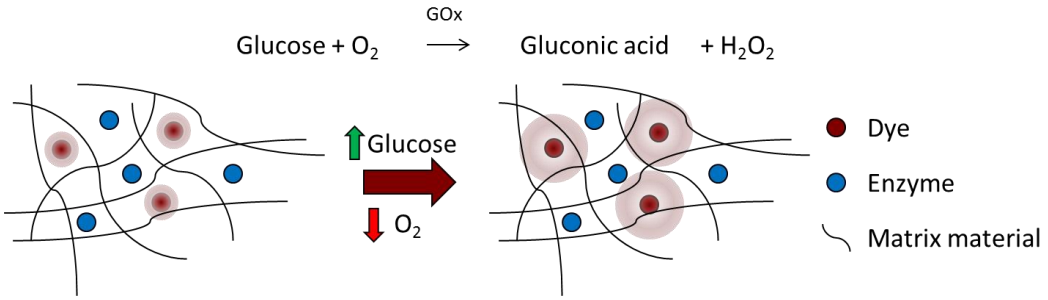

Figure 7: Optical enzymatic sensing chemistry utilizing glucose oxidase (GOx) and oxygen-sensitive dye. As glucose is consumed by the enzyme, oxygen levels decrease, causing the dye to become less quenched, increasing intensity and lifetime of the phosphorescence.[167]

As glucose is consumed by glucose oxidase in the sensor, oxygen concentration is diminished. This results in a proportional *increase* in phosphorescence lifetime and intensity, both of which can be measured optically. Because this system is light-based, the material can be interrogated through the skin, with no need for transcutaneous connection. This makes glucose sampling non-invasive, unlike current commercially available electrochemical devices. Additionally, the sensing elements (enzyme and dye)

can be immobilized in a variety of architectures to suit the application. For example, this sensing chemistry can be immobilized in microparticles, multilayer nanofilms, or in larger slab materials.[168-170]

2.5 Multianalyte sensors and multifunctional systems

As biomaterials, sensing technologies, and our understanding of the intricacies of chronic disease have advanced, there has been increasing interest in the use of multianalyte and multifunctional systems.[171-173] These systems perform multiple functions such as the measurement of multiple analytes (multianalyte sensors) and/or the application of therapeutics (mutlifunctional). Utilization of closed-loop systems involving sensing of important analytes and the application of therapeutics, such as with the artificial pancreas, is the ultimate goal for treatment and monitoring of chronic disease.[174]

2.5.1 Multianalyte/mulitmodal sensing

Multianalyte sensing involves the sensing of multiple molecular species simultaneously. Though this can be done using multiple sensors and multiple devices, in the ideal case, a single device would produce the measurements. However, in a single device, there are limitations to utilizing a single sensing mode. Specifically, using a single sensing mode, such as fluorescence intensity, makes the separation of individual analyte signals difficult in a system where sensing chemistries are in close proximity to one another. Sensing chemistries designed to produce changes in a particular transduction mechanism need to be different from one another and interfere minimally. One approach to doing this is to utilize multiple sensing modes (multimodal). This

could involve the use of any number of different transduction mechanisms, but in the case of fully implantable sensors, optical methods have clear advantages.[132, 171] Utilizing multiple modes such as fluorescence intensity, Raman spectroscopy, or phosphorescence lifetime, signals from different analytes or the simultaneous measurement of the same analyte can be performed. In these systems, the primary challenge is the coimmobilization and optimization of each different sensing chemistry within a single sensor. Despite the challenges, the development of such multianalyte sensors has enormous potential for diagnosis, monitoring and prediction in chronic conditions, as well as for individualized medicine.[175]

2.5.2 Multifunctional implants

Smart, multifunctional implants represent the end goal of implantable sensor and therapeutics. Individualized medicine will need to have technologies that gauge the effectiveness of treatments or provide custom treatments to produce better outcomes. Closed-loop systems could allow for much tighter regulation of disease states and better management of adverse conditions, and multianalyte sensors could provide new insight into the diagnostic markers in the development of chronic disease and effective treatments. To date, while there has been interest in producing multifunctional sensing and therapeutic devices, none have made it into the hands of patients.

Due to the great potential for impact in the management of chronic disease by utilizing multifunctional implants, I have proposed a composite material, made from calcium carbonate, polyelectrolyte multilayers, and alginate, in which multiple sensing or therapeutic elements can be encapsulated within a single, injectable matrix. This

system utilizes the tunable qualities of polyelectrolyte multilayers, the material encapsulation qualities of calcium carbonate, as well as the biocompatibility and mild gelation properties of alginate. As this material has never before been characterized, the basic properties of the material required investigation. To prove the composite's ability to function as an injectable, multianalyte sensing platform, the composite was characterized for material encapsulation potential, gelation and mechanical properties, and sensor response characteristics, each of which are discussed in the follow sections.

3. MICROPOROUS ALGINATE COMPOSITE (MPAC) FABRICATION*

Calcium carbonate microspheres in combination with polyelectrolyte multilayers have been widely utilized to house sensing chemistries and other molecules for therapeutic and diagnostic purposes.[122, 130-137] Capsules have the advantage over other immobilization techniques because they allow the free movement of encapsulates within them (important for affinity or binding chemistries) while allowing for a selective permeability of their walls.[142, 146] However, injection of capsules alone into the subcutaneous space (a common target region for injectables) has drawbacks, with the primary pitfalls being the potential for phagocytosis and migration of capsules from the original site.[176] Therefore, it is desirable to provide extra structure or linkage between capsules to mitigate this risk. There are several examples of carrier materials for microsphere injection, including the natural extracellular matrix-like materials collagen, hyaluronic acid and alginate.[176] These materials serve only to separate particles and ease the injection of microspheres, and do not provide significant, long-term mechanical support once the solution is injected. It is therefore desirable to create a crosslinked network in the carrier solution after injection, so that a mechanically stable support can be provided to the capsules.

---

*Parts of this section have been reprinted from J. R. Roberts, D. W. Ritter and M. J. McShane, *Journal of Materials Chemistry B*, 2013, **1**, 3195-3201 – Reproduced by permission of The Royal Society of Chemistry.

Alginate has been used as a biocompatible carrier material in a wide variety of applications. However, similar to the capsules, ungelled alginate carrier can migrate (or be cleared) from the site of interest.[176, 177] Alginate hydrogels can be formed based upon the addition of calcium ions to the system. This can be accomplished by utilizing $CaCO_3$ and GDL in an internal gelation mechanism.[68] However, in order to create alginate hydrogels with significant mechanical integrity, enough calcium must be provided to create a reasonable number of crosslinks. When using large amounts of $CaCO_3$, gelation can occur extremely quickly making injection more difficult.

In order to create an injectable system that has the advantages of $CaCO_3$-based capsules and gelled alginate, a composite system utilizing nanofilm-coated $CaCO_3$ and alginate was conceived. It was hypothesized that addition of nanofilms to the calcium carbonate would allow simultaneous, controlled gelation of the alginate while retaining materials of interest within microcapsules inside the alginate matrix. The resulting composite would be a polymer matrix material that contains diffusion-controlled regions that could serve as "microreactors" or drug depots that could be injected and remain in place for a reasonable period of time (Figure 8).

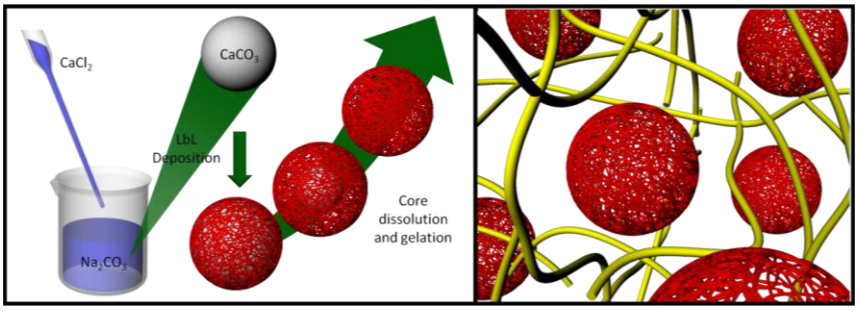

Figure 8: Schematic of the gelation process of MPAC hydrogels.

Microporous alginate composite (MPAC) hydrogels accomplish this by use of delayed diffusion of crosslinking calcium ions into the alginate matrix. The addition of nanofilms to the calcium carbonate microspheres causes this delayed diffusion, but also serves to create pores in the composite which could contain functional materials such as drugs, biomolecules, or nanoparticles. However, this system has never been attempted or evaluated, and so the basic assumptions about the functional properties (pore formation and nature, material encapsulation and retention, environmental interaction) of the composite were evaluated.

3.1 Theory and methods

The initial characterization of MPAC gels focused on the ability of the material to form in a predictable way and perform basic application functions. In order to determine the feasibility of MPACs for use as an injectable sensor and therapeutics depot, several different properties of the material were evaluated.

Firstly, morphological differences of alginate made with and without polyelectrolyte-coated $CaCO_3$ microspheres were compared. Scanning electron and confocal microscopy were used together to determine the basic structural properties of the composite. Scanning electron microscopy provides a high resolution view of the macrostructure of the composite (including the alginate and the polyelectrolyte capsules), while confocal imaging provides a means to visualize material within the pores of a fully-hydrated composite.

In order to prove the ability of the composite system to encapsulate and retain functional material, model materials including a model macromolecule (bovine serum

albumin, BSA), nanoparticles (FluoSpheres), and enzyme (glucose oxidase, GOx) were incorporated into the composite *via* loading of the material into the $CaCO_3$ microspheres by coprecipitation. Material to be encapsulated was first labeled with fluorescent tags for visualization and quantification. Due to its high resolution and reduction of background fluorescence, confocal microscopy was utilized to visualize the tagged material within the hydrogels fabricated with and without polyelectrolyte multilayers and determine if the tagged material was confined to the defined volume of the pores in the case of the composite. Standard fluorescence microscopy, which has much faster image acquisition than confocal microscopy, was performed to visualize movement of encapsulated nanomaterials within the polyelectrolyte pores to confirm that the pores of the composite allow the free movement of encapsulated material after dissolution of the template (an important property for binding chemistries). In both cases, utilizing fluorescence microscopy allows for the real-time visualization and characterization of the fully-hydrated system. In addition to direct visual observation, encapsulated macromolecules were confirmed to be retained in the hydrogels by exposing the composites to excess buffer and sampling the external environment over time for the presence of fluorescent material *via* fluorescence spectroscopy.

As a final measure of feasibility, apparent activity of the encapsulated model enzyme was measured by colorimetric assay to show that catalytic activity of encapsulated material. While not a direct measure of *specific* enzyme activity, the measurement of activity from a composite hydrogel does confirm that the encapsulated enzyme can react with substrate supplied from outside the bulk material, and retains a

significant portion of its original activity. This is important, as each process step in the manufacture of the composite, including coprecipitation/adsorption on the $CaCO_3$ surface and dissolution by GDL, could potentially cause inactivation of the enzyme due to denaturation or chemical reaction. Retention of enzyme activity is crucial to the function and stability of enzyme-based sensing chemistries, and so confirmation of formulation stability is essential.

3.1.1 Materials

Poly(sodium 4-styrenesulfonate) (PSS, average M_w = 70,000 Da), poly(allylamine hydrochloride) (PAH, average M_w = 51,495 Da), rhodamine B isothiocyanate (RITC, mixed isomers), albumin from bovine serum (BSA, >99% by agarose gel electrophoresis, *ca.* 66 kDa), alginic acid sodium salt from brown algae (281 cps for a 2% aqueous solution at 25 °C), and peroxidase from *Amoracia rusticana* (type II, 188 U/mg solid) were obtained from Sigma and used without further purification. Glucose oxidase from *Aspergillus niger* (GOx, 257 U/mg solid, 71.1% protein by Lowry, *ca.* 160 kDa) was obtained from BBI Enzymes. FluoSpheres® (2% solids, carboxylate-modified microspheres, λ_{ex} = 505 nm, λ_{em} = 515 nm) were obtained from Invitrogen.

3.1.2 Calcium carbonate coprecipitation

All calcium carbonate microspheres utilized in these initial experiments were prepared by precipitation and growth resulting from the reaction of the two soluble salts Na_2CO_3 and $CaCl_2$. Material present in the solution prior to precipitation will be co-precipitated inside the microspheres resulting in "loaded" microspheres.[139] Briefly,

loaded $CaCO_3$ microspheres were prepared by adding 8 mL $CaCl_2$ (0.25 M) to 8 mL Na_2CO_3 (0.25 M) containing 4 mg/mL PSS and the material to be encapsulated (*ca*. 1 mg/mL rhodamine-labeled BSA (RITC-BSA), 24 nm FluoSpheres at 0.01% solids, 100 nm FluoSpheres at 0.01% solids, or 200 nm FluoSpheres at 0.01% solids). PSS is normally added to stabilize the surface of the $CaCO_3$ microspheres.[178] However, for $CaCO_3$ microspheres containing GOx, the Na_2CO_3 solution consisted of 8 mg/mL GOx only (*i.e.*, no PSS) as the polyelectrolyte greatly inhibits encapsulation of materials with high adsorptive potential. After addition of the $CaCl_2$, the solution was stirred vigorously for 30 s, after which time the agitation was removed and the particles were allowed to mature under static conditions for 12.5 min. The suspension was centrifuged (500g, 60 s) and the supernatant was removed. The microspheres were then rinsed three times with deionized water prior to further processing.

3.1.3 Layer-by-layer deposition

PEMs were deposited onto the loaded $CaCO_3$ microspheres using electrostatic LbL self-assembly, in which oppositely charged polyelectrolytes are deposited onto the particle surface in alternating fashion (Figure 9).[57]

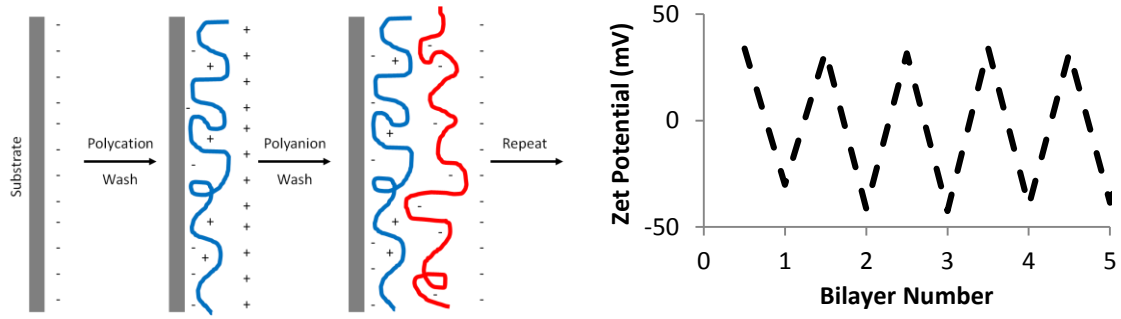

Figure 9: Left: Schematic of electrostatic adsorption process. Right: Example zeta potential data for particles coated with alternating polyelectrolyte.

For the initial study, commonly used polyelectrolytes, poly(4-styrene sulfonate) (PSS) and poly(allylamine hydrochloride) (PAH) were utilized as these materials are widely characterized and a staple of previous work within our laboratory.[113, 132, 133, 179] To deposit layers, microspheres were suspended in polyelectrolyte solutions (PSS or PAH at 2 mg/mL containing 0.5 M NaCl in deionized water) for 12 min, rinsing with deionized water between each deposition step to remove unbound polyelectrolyte. PSS was deposited initially, and then PAH and PSS were alternated until 10.5 bilayers of PSS/PAH were deposited. Successful LbL deposition on the particles was confirmed *via* zeta potential measurements.

3.1.4 Alginate internal gelation

Based on the findings of Kuo and Ma for maximum strength internal ionotropically gelled alginate,[55] the $CaCO_3$: carboxylic acid (from alginate): GDL molar ratio was maintained at 1:0.27:2 for all alginate hydrogels. A 16.8 mg/mL solution of $CaCO_3$ microspheres (250 µL, PEM-coated or uncoated) was thoroughly mixed with 500 µL of 3% (w/v) alginate. To this solution, 250 µL of 29.8 mg/mL GDL was added.

After further mixing, the solution was placed into the appropriate mold and allowed to gel for 24 h. Figure 10 and Figure 11 schematically illustrate the process of forming microporated alginate (MPA) hydrogels and depositing them into molds respectively.

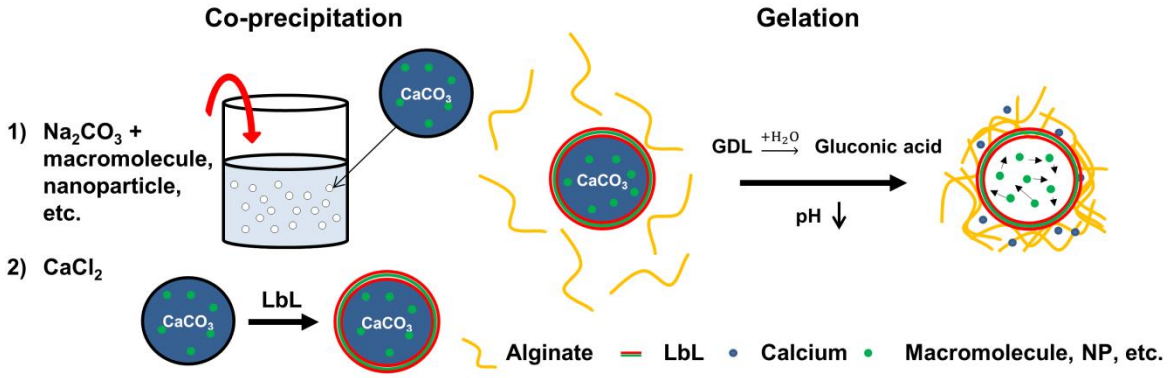

Figure 10: Schematic illustrating the MPAC fabrication process. $CaCO_3$ particles are precipitated, coated in polyelectrolytes (left), and then mixed with alginate and GDL to form the composite (right).

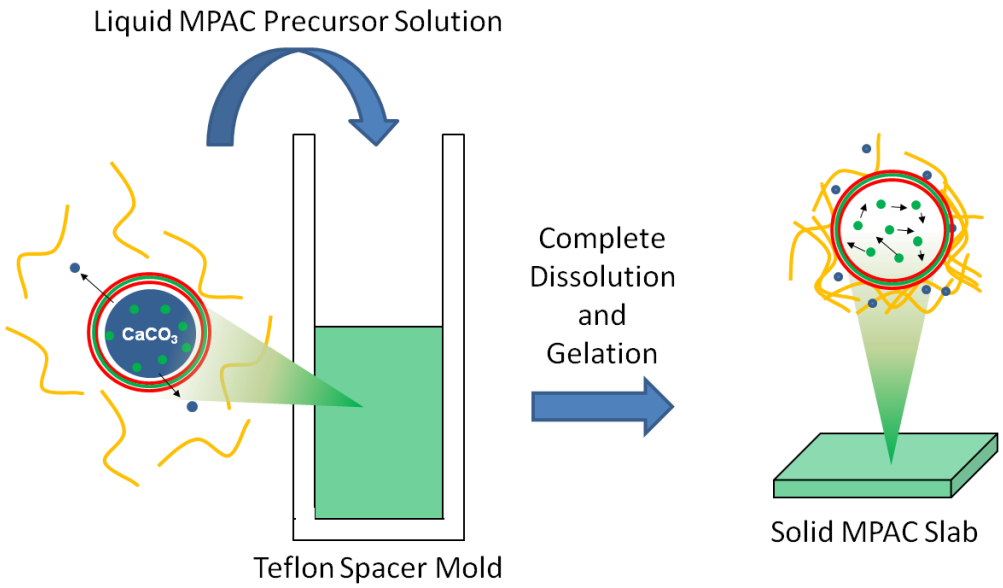

Figure 11: Molding of MPAC gels utilizing Teflon spacers. Precursor solution is deposited in the molds and allowed to completely gel (left). Gelled MPAC slabs (right) can then be removed from the mold and samples can be tested for mechanical and functional properties.

3.1.5 Physical characterization of microspheres, microcapsules, and hydrogels

Alginate hydrogels constructed with PEM-coated and uncoated $CaCO_3$ microspheres containing RITC-BSA or FluoSpheres were cast between two glass slides with 0.03" Teflon spacers for electron and optical microscopy (Figure 11). A benchtop scanning electron microscope (JEOL model JCM-5000 NeoScope) was used to image microcapsules, PEM-coated and uncoated $CaCO_3$ microspheres, and hydrogels constructed using $CaCO_3$ microspheres. Samples were placed on conductive tape, air-dried at room temperature for 24 hours, and sputter-coated with a thin layer of gold to prevent charging. Samples were held under high vacuum and an accelerating voltage of 10 kV was used when collecting images.

Optical micrographs were obtained using a confocal microscope (Leica model TCS SP5) equipped with a 63x oil immersion objective. An Ar ion laser (λ_{em} = 488 nm) was used to excite the FluoSpheres, while a HeNe laser (λ_{em} = 543 nm) was used to excite the RITC-BSA; in all cases in which hydrogels were imaged, the pinhole diameter was minimized to eliminate out-of-focus light from the scattering samples. A second confocal microscopy system (Leica model TCS SP5-RS) equipped with a high-speed resonant scanner and a 63x water immersion objective was used to collect a z-stack of an MPA hydrogel containing 100 nm FluoSpheres. ImageJ was used to produce reconstructions of the images. An epifluorescence microscope (Nikon model Eclipse TE2000-U) equipped with a monochromatic camera (Photometrics model CoolSNAP HQ^2) was used to collect the video demonstrating the 200 nm FluoSpheres moving within the microcavities of the alginate hydrogel.

3.1.6 Release and retention of macromolecules

Hydrogels made with PEM-coated and uncoated $CaCO_3$ microspheres loaded with RITC-BSA (100 μL each) were cast into individual wells of a 96-well microplate. After the initial gelation period of 24 h, an extreme excess of GDL (100 μL of 0.1 M) was added to each hydrogel-containing well to ensure full dissolution of the $CaCO_3$. After 30 min, the GDL solution was removed and placed in an empty well, and 100 μL of release buffer (*i.e.*, 0.1 M HEPES, pH 7) was added to the alginate hydrogel-containing well. After the appropriate incubation time (0.5, 1, 2, 4, 24 and 48 hours), release buffer from each sample was then removed and placed in an empty well, and fresh buffer was added to the wells containing the alginate hydrogels. Fluorescence

intensity (λ_{ex} = 560 nm, λ_{em} = 590 nm) was measured for each sample and time point (including the first GDL wash) using a microplate reader (Tecan model Infinite F200).

3.1.7 Encapsulated enzyme activity

Activity assays on MPAC hydrogels were performed using an enzyme-coupled colorimetric assay.[180] Equations (3.1) and (3.2) represent the two enzymatic reactions utilized. In these reactions, the production of oxidized *o*-dianisidine at substrate saturation produces a linear change in 500 nm absorbance of the solution over time (Figure 12), with the slope of the linear portion representing the *apparent* activity of GOx in the matrix. It is important to note that the apparent activity represents a convolution of enzyme concentration, specific activity and diffusion differences. These differences cannot be separated in the complex architecture of the composite.

(3.1) β-D-Glucose + O_2 + H_2O ⟶ D-Glucono-1,5-Lactone + H_2O_2 (GOx)

(3.2) H_2O_2 + *o*-dianisidine (reduced) ⟶ *o*-dianisidine (oxidized) (POx)

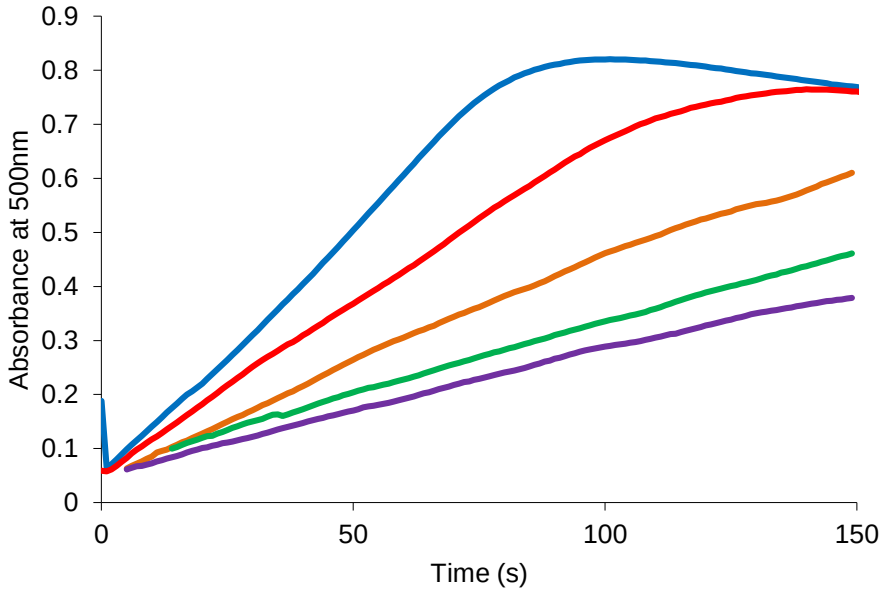

Figure 12: Representative data collected from activity assays with *o*-dianisidine. Slope of the linear portion of the curve represents apparent activity of the material and is a result of a convolution of enzyme concentration, specific activity and diffusion differences.

MPAC hydrogels made with PEM-coated $CaCO_3$ microspheres containing the model enzyme GOx (100 µL each) were cast into individual wells of a 96-well microplate. After 24 h gelation time, reaction cocktail containing the assay chemistry was added to the gelled MPACs within the microplate and assayed. Briefly, 200 µL of the reaction cocktail (0.17 mM *o*-dianisidine, 1.72% (w/v) glucose, 2 units/mL peroxidase in 50 mM sodium acetate buffer, pH 5.1) were added to each well using the automated dispensing system on the microplate reader. All measurements were performed at pH 5.1 and 35 °C. Absorbance of each well was then monitored at 500 nm for 10 min, and the slope of the absorbance change was used to determine apparent activity.

3.2 Results and discussion

3.2.1 Physical characterization of microspheres, microcapsules, and hydrogels

Full characterization of MPAC hydrogels compared to those without PEMs requires an examination of each of the component parts. Alginate hydrogels were prepared using an adapted internal ionotropic gelation method.[68] This method involves the use of PEM-coated and uncoated $CaCO_3$ loaded with model materials, allowing for direct comparison of the effects of the PEMs. Initially, materials were loaded into $CaCO_3$ microspheres by co-precipitation followed by LbL deposition of PEMs onto the loaded microspheres (Figure 10). Three materials—Rhodamine B-labeled bovine serum albumin (RITC-BSA), FluoSpheres, and glucose oxidase (GOx)—were used to produce three different types of loaded microspheres representing incorporation of a model macromolecule, model nanoparticle, and model enzyme, respectively.

Before manufacture of alginate hydrogels, microspheres containing RITC-BSA were exposed to GDL to confirm particle dissolution and demonstrate capsule integrity. Figure 13 shows PEM-coated $CaCO_3$ microspheres containing RITC-BSA exposed to deionized water (Figure 13A and B) or GDL (Figure 13C and D). While particles exposed to water remain solid, complete dissolution of the $CaCO_3$ template by GDL is evident by electron microscopy (Figure 13C); the microcapsules, which are composed of PEMs that remain after GDL treatment, appear collapsed due to dehydration of the once solvent-filled core. Fluorescence microscopy confirms that the microspheres contain RITC-BSA (Figure 13B), and that the encapsulated material is retained within the microcapsules following GDL exposure (Figure 13D).

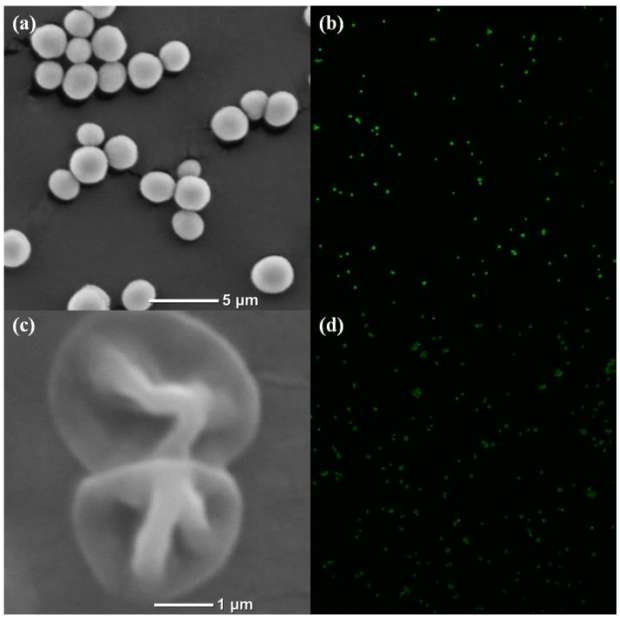

Figure 13: SEM micrographs (left) and confocal images (right) of coated $CaCO_3$ microspheres (top) and polyelectrolyte multilayer capsules (bottom).

After determination of capsule integrity, $CaCO_3$ microspheres with or without polyelectrolyte coatings were used to fabricate alginate hydrogels. Resulting gels were compared using SEM and confocal microscopy. Figure 14 illustrates the remarkable difference between alginate hydrogels formed using uncoated (Figure 14A-D) and PEM-coated (Figure 14E-H) $CaCO_3$ microspheres containing RITC-BSA. When uncoated $CaCO_3$ microspheres were used in the manufacture of alginate hydrogels, no noticeable pores were observed in the electron micrographs (Figure 14A-C). Instead, they exhibit a smooth appearance with some wrinkling due to dehydration.

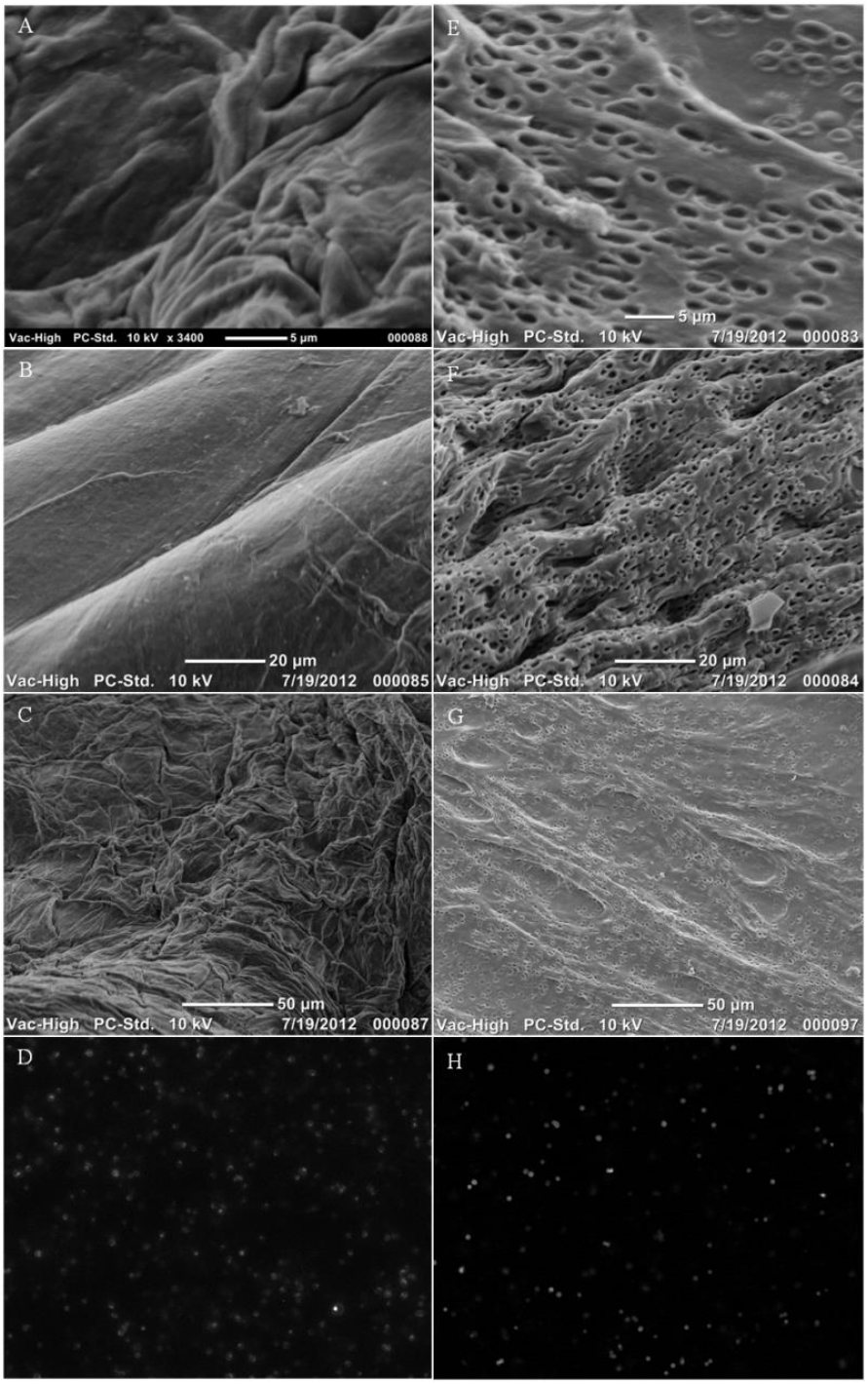

Figure 14: SEM micrographs of alginate hydrogels fabricated with no polyelectrolyte multilayers (PEMs) on $CaCO_3$ (A-C) and with PEMs (E-G). Bottom: Confocal images of the same alginate gels fabrication with uncoated $CaCO_3$ (D) and coated $CaCO_3$ (H).

The nonporous nature of the hydrogels manufactured with uncoated microspheres is expected, as this is similar to the internal gelation mechanism employed by Kuo and Ma, which resulted in homogenous alginate hydrogels.[68] When these hydrogels were inspected using confocal microscopy immediately after gelation, fluorescent material can be found in close proximity to where microspheres were dissolved (Figure 14D). However, these patches have undefined boundaries due to the free diffusion of material in the alginate. This can be seen more clearly in Figure 15, where fluorescence intensity within hydrogels made with coated $CaCO_3$ is concentrated in distinct points (right) while intensity within uncoated $CaCO_3$ hydrogels is not. It is noteworthy that after a period of hours, distinct patches of fluorescent material can no longer be found in hydrogels formed using uncoated $CaCO_3$ (data not shown).

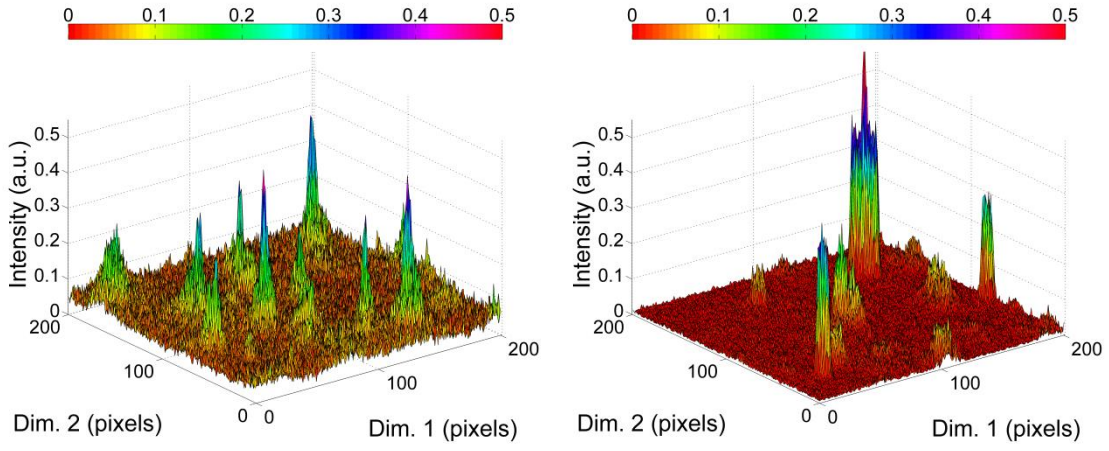

Figure 15: Fluorescence intensity maps of alginate hydrogels made with uncoated $CaCO_3$ (left) and coated $CaCO_3$ (right).

This absence of visible fluorescence further demonstrates the free diffusional nature of the macromolecule in the matrix, which eventually results in the complete loss of material from the bulk alginate into the surrounding solution. In contrast, when PEM-coated $CaCO_3$ microspheres were used in the manufacture of alginate hydrogels, a clearly distinguishable microporous structure was observed (Figure 14E-G). Upon dehydration of the MPAC hydrogels in preparation for electron microscopy, they exhibited a wrinkled morphology with randomly distributed micropores. In confocal micrographs, the encapsulated RITC-BSA appears to occupy distinct regions of the hydrogel within defined boundaries (Figure 14H), demonstrating confinement of the fluorescent macromolecules within the micropores.

MPAC hydrogels manufactured with PEM-coated $CaCO_3$ microspheres containing FluoSpheres had a comparable microporous structure to that of hydrogels containing RITC-BSA (Figure 16); however, the PEM-coated pores did not fully collapse under vacuum as in the RITC-BSA-containing MPAC gels, presumably due to the greater volume of encapsulated material.

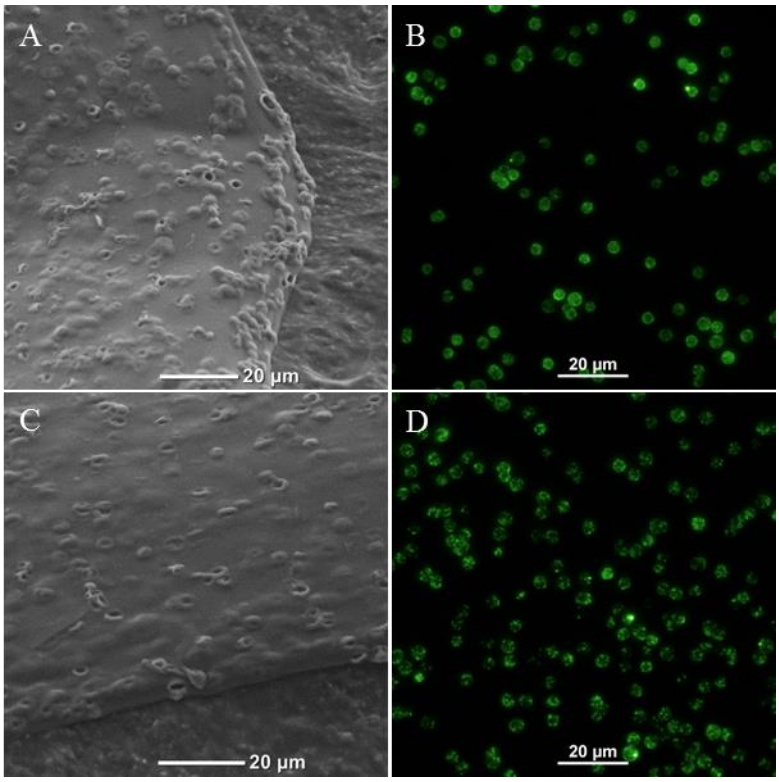

Figure 16: SEM micrographs (left) and confocal images (right) of MPAC gels fabricated with 100nm Fluospheres (top) and 200nm Fluospheres (bottom).

As with RITC-BSA-loaded MPACs, confocal micrographs of FluoSphere-loaded MPAC display distinct regions of fluorescent material (Figure 16), indicating confinement within the PEM pores. Additionally, three-dimensional reconstruction of confocal images of a MPAC hydrogel containing the FluoSpheres demonstrates the distribution of PEM-lined micropores within the alginate matrix and the confinement of the encapsulated material within those pores (not shown). Utilizing non-confocal fluorescence microscopy, free movement of the nanoparticles was confirmed by observation of their random motion within the micropores of the MPAC hydrogels (not shown).

3.2.2 Release and retention of macromolecules

While it was qualitatively observed in the previous section that macromolecules (RITC-BSA) are retained within the pores, a quantitative assessment of retention was required to confirm the observation. It is expected from previous work with alginate that large macromolecules can diffuse through the alginate matrix.[62] As such, alginate gels fabricated with uncoated calcium carbonate spheres were expected to release protein into the local environment. Polyelectrolyte multilayers, however, have been shown to exclude large molecules from passage through them.[113-115] To evaluate the release of encapsulated macromolecules from the alginate hydrogels and determine the effects of PEM coatings on this behavior, hydrogels prepared with PEM-coated and uncoated $CaCO_3$ microspheres loaded with RITC-BSA were cast into wells of a microplate. Release of the labeled macromolecule into the surrounding media was then monitored over a period of 55 h.

Alginate hydrogels formed using PEM-coated $CaCO_3$ microspheres loaded with RITC-BSA showed significantly improved retention of the encapsulated material as compared to hydrogels formed using uncoated microspheres (Figure 17, left). Release of RITC-BSA from hydrogels formed using uncoated microspheres was approximately 50 times higher than the release observed from hydrogels formed using PEM-coated microspheres. However, in the ideal case in which PEM coatings are completely devoid of defects, no release of the encapsulated macromolecules from the microcapsules is expected.

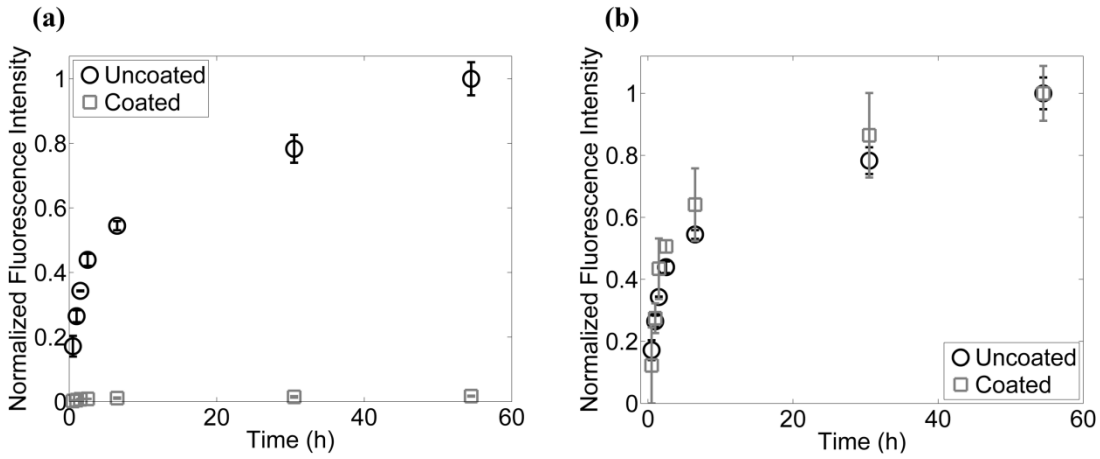

Figure 17: (a) Normalized release characteristics of alginate hydrogels fabricated with uncoated $CaCO_3$ (○) and coated $CaCO_3$ (□). (b) Release characteristics when normalized to each sample. Error bars represent 95% confidence intervals (n=4).

The similar shape of the individually normalized curves (Figure 17, right) suggests similar transport behavior (*i.e.*, similar diffusional characteristics of the RITC-BSA through the bulk alginate) in both types of hydrogels. This can be confirmed mathematically by utilizing Fick's Laws of Diffusion. In both alginate gels, the same concentrations of particles were used, and so the concentration of encapsulated material is the same, as uncoated particle containing materials were simply coated in polyelectrolyte after fabrication. Therefore, the same quantity of material could potentially be released from both systems. Fick's Second Law states:

$$\frac{d\varphi}{dt} = D\nabla^2\varphi \quad (3.3)$$

Here, the change in concentration of the diffusing material is proportional to the concentration gradient $\nabla\varphi$, and the diffusivity D. In the case of the uncoated versus coated MPAC systems, two D values could be assumed: D_2 represents the diffusivity of

the material through alginate matrix, and D_1 represent the diffusivity of material through the polyelectrolyte. In order to determine the change in material outside the alginate, the following simple equation can be applied to the case of uncoated alginate: $\frac{d\varphi}{dt} = D_2\nabla^2\varphi$.

In this specific case, as material diffuses out of the alginate, the gradient $\nabla\varphi$ decreases over time, as there is a set amount of total material and a set amount of volume. As a result, $\frac{d\varphi}{dt}$ decreases over time, causing the release behavior to follow an exponential decay behavior, where $\frac{d\varphi}{dt} \rightarrow 0$ as $t\rightarrow\infty$ observed in Figure 17. Additionally, the end concentration will trend to the total amount of material over the fixed volume. In the case of PEM-containing alginate, the change in concentration of the diffusing material is subject to a more complicated system in which there is a diffusion barrier created by the polyelectrolyte multilayers. This adds a considerable amount of complexity to the system, but can be simplified by treating the system as two components, where there is a boundary condition immediately outside the nanofilms. In this case, there are two different diffusion equations: $\frac{d\varphi_2}{dt} = D_2\nabla^2\varphi_2$ and $\frac{d\varphi_1}{dt} = D_1\nabla^2\varphi_1$. The change in concentration of material outside the alginate is subject to the diffusivity through the alginate, D_2, but also the concentration at the boundary, which follows from $\frac{d\varphi_1}{dt} = D_1\nabla^2\varphi_1$. Therefore, the rate of change in concentration outside the alginate is dependent on the rate of change in concentration through the nanofilm. In the case where $D_1 << D_2$, equilibration outside the alginate occurs much faster than the rate of change at the boundary, and so $\nabla\varphi \rightarrow 0$, and $\frac{d\varphi_1}{dt} = D_1\nabla^2\varphi_1$ will be rate-limiting and will govern the overall behavior. In the case where $D_1 >> D_2$, the boundary concentration

is at a maximum and $\frac{d\varphi_2}{dt} = D_2\nabla^2\varphi_2$ will govern. Based upon this simplification, we can see that the ideal coated case, in which D_1=0, no change in boundary concentration occurs, and $\frac{d\varphi_2}{dt}$=0 (there should be no release). However, in the case where $D_1 >> D_2$, $\frac{d\varphi}{dt}$ will have the same release behavior as the uncoated case, as the boundary essentially does not exist. Since the time-dependent release characteristics of the coated particles match those of the uncoated, we can conclude that the case where $D_2 << D_1$ is occurring. However, the magnitude difference between total amounts released in each case indicates that only a proportion of the total material is being released for the PEM-coated system. Therefore, the release of a minuscule amount of material in the hydrogels formed using PEM-coated microspheres is likely due to defects in a small fraction of the microcapsules (*e.g.*, incomplete film coverage, tearing of the microcapsule wall, *etc.*) where diffusivity through these layers ~0, and the remaining material is locked with capsules, where $D_1 >> D_2$ and $\frac{d\varphi}{dt}$=0.

3.2.3 Encapsulated enzyme activity

The preservation of an encapsulated enzyme's activity, as well as the system's ability to interact with the surrounding environment is paramount to the utility of the system in catalytic and/or biosensing functions. Therefore, hydrogels prepared with PEM-coated $CaCO_3$ microspheres loaded with GOx were cast into wells of a 96 well microplate and assayed for relative enzymatic activity to determine whether catalytic function is preserved during fabrication of an MPAC hydrogel and whether the encapsulated enzyme can react with substrate from outside the hydrogel composite. A

substrate cocktail (*i.e.*, glucose, peroxidase, and the chromophore *o*-dianisidine) was added on top of the GOx-containing MPAC hydrogel, resulting in an observable absorbance change within the hydrogel and in the surrounding media (Figure 18).

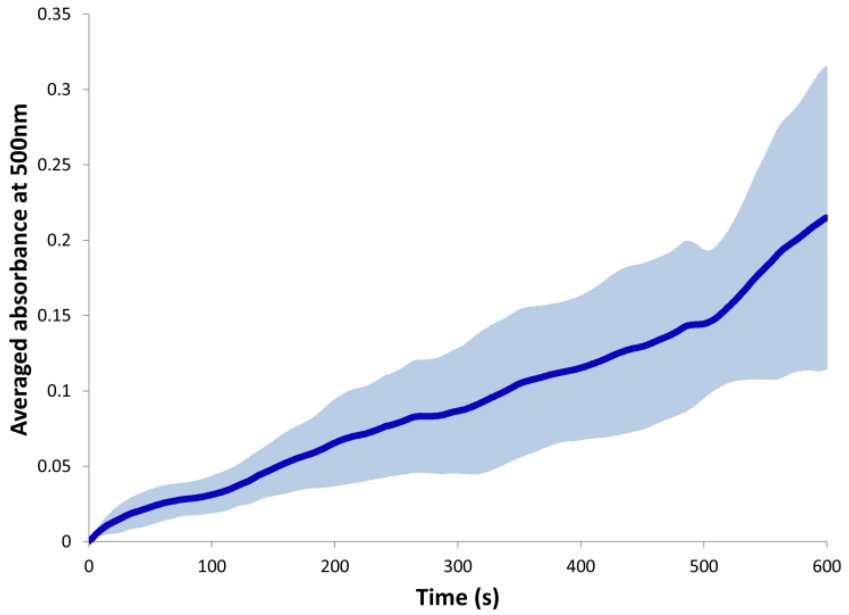

Figure 18: Absorbance change of MPAC gels and surrounding solution as a result of addition of reaction cocktail indicating relative GOx activity. Solid line represents the average absorbance at a particular time while light blue area represents the 95% confidence interval of the absorbance at a particular time (n=5).

This absorbance change results from coupled enzymatic reactions catalyzed by GOx confined within the microcavities of the hydrogels, as well as peroxidase within the media. It is important to notice that the rate of absorbance increase represents the *apparent* activity, and is affected by the concentration and reaction rate of both enzymes,

as well as diffusional limitations of the various substrates imposed by the alginate matrix and the PEMs. Figure 18 shows the average and confidence intervals of individual points in time for multiple samples, and so shows increasing variability over time due to slight differences in slope. When individual sample curves were fit linearly and averaged, the apparent activity was found to be $8.0 \pm 0.7 \times 10^{-3}$ units/mL composite, where 1 unit will oxidize 1.0 μmole of β-D-glucose to D-gluconolactone and H_2O_2 per minute. These data confirm that the encapsulated GOx retains enzymatic activity throughout the entire MPAC hydrogel formation process (*i.e.*, from entrapment within the $CaCO_3$ microspheres to dissolution of the template by GDL). Moreover, it demonstrates that small molecules can quickly permeate the alginate matrix and diffuse into and out of the micropores, while confining the larger, enzymatically-active material within the micropores.

3.3 Conclusions

The results presented in this section provide the initial evidence of feasibility that composite alginate hydrogel materials can be manufactured in a way that produces defined regions in which molecules and nanoparticles can be spatially confined. Unlike standard internal gelation techniques which utilize uncoated $CaCO_3$ particles, the dissolution of the PEM-coated $CaCO_3$ results in pore formation and material retention. Within the composite matrix, PEMs surround the individual pores and form a semi-permeable membrane which retains large molecules and nanoparticles while allowing for small molecules, such as glucose and H_2O_2, to diffuse in and out of the composite. This controllable diffusion barrier is the key advance in the development of injectable

alginate materials, as it allows for incorporation of chemistries in a way that allow for control of flux-dependent function such as drug elution profile or sensor response characteristics.

While these initial findings are very promising, some additional fundamental understanding of the composite system is needed to fully grasp the potential for different applications. For example, the development of *in situ*-gelling materials for injection requires a basic understanding of their gelation kinetics so that gelation times can be engineered for the appropriate application. For this system in particular, it is unknown how diffusion barriers will affect the balance between GDL hydrolysis and $CaCO_3$ dissolution, which could affect gelation times as well as the pH balance during the process. Furthermore, internal gelation techniques have been shown to cause variations in hydrogel material properties related to the speed of gelation,[68] and so the relationship between any changes in gelation kinetics and resulting composite mechanical properties needs to be understood. Once these fundamental properties are understood, further development of MPAC systems containing functional elements, such as sensing chemistries or therapeutics, can be developed.

4. COMPOSITE GELATION AND MECHANICAL PROPERTIES

While it has been shown that MPAC hydrogels can encapsulate and retain functional materials, the relationship between PEMs, gelation behavior and mechanical properties is as yet unknown. Understanding gelation kinetics and physical properties of injectable matrix materials is fundamental to the further development of functional implants containing sensing or therapeutic molecules. *In situ*-gelling materials in particular require that gelation occur in residence after injection, requiring the precursor mixture to remain in liquid form long enough to allow for handling of the precursor prior to injection.

As described in Section 2, alginate transitions from liquid solution to hydrogel in the presence of calcium ions. Exposure to calcium can come from externally applied calcium (external gelation) or from an insoluble salt within the alginate liquid (internal gelation). Fabrication of alginate hydrogels by either external or internal gelation is highly dependent on the diffusion of calcium ions to the binding sites within the alginate. In the case of external gelation, the gelation of the material results simply from the movement of added calcium ions from the outside of the alginate through the pregel. For internal gelation, the relationship is much more complicated. The internal gelation mechanism utilizes insoluble salts, such as $CaCO_3$, that can be dissolved *via* acid hydrolysis to release ionic crosslinkers. $CaCO_3$, a commonly utilized salt, aids in internal gelation according to several simultaneous processes including the following reactions:

$$\text{(4.1)}\quad \text{Glucono-}\delta\text{-lactone} + H_2O \overset{k1([OH^-])}{\longleftrightarrow} \text{Gluconate}^- + H^+ \text{ (hydrolysis)}$$

$$\text{(4.2)}\quad CaCO_3 \overset{k_2([H^+])}{\longleftrightarrow} Ca^{2+} + CO_3^{2-}$$

$$\text{(4.3)}\quad CO_3^{2-} + H^+ \overset{k_3}{\leftrightarrow} HCO_3^-$$

$$\text{(4.4)}\quad HCO_3^- + H^+ \overset{k_4}{\leftrightarrow} CO_2 + H_2O$$

The reaction (4.1) is a relatively slow reaction that is catalyzed by the presence of acid or base present in the solution. The reaction rate in this case is then dependent on the pH of the solution, where increasing difference from pH 7 results in a faster reaction. In addition to the hydrolysis of GDL, There are three equilibrium reactions of carbonates (4.2-4.4). Each one of the equilibrium reactions has an associated rate constant (k_x) for both forward and backwards directions that is dependent on the concentration of each of the constituents on either side of the equilibrium reaction. What can be taken from the carbonate equilibrium reactions is that if hydrogen ion concentration increases, $CaCO_3$ will tend to break down and form carbonates of lesser charge. This is the basic mechanism of internal gelation, as the hydrolysis of GDL produces hydrogen ions which, in turn, fuel the dissolution of $CaCO_3$ and the production of calcium ions. Previous work has shown increases in gelation time when comparing internal to external gelation.[68] Thus, it can be concluded that reaction (4.1) plays a central role in standard internal gelation techniques. However, while the standard internal gelation mechanism is driven by the reactions previously described, MPAC gelation is not. MPAC structure creates a diffusion barrier between sources of GDL/hydrogen ions in the alginate from the calcium carbonate source of the microparticles. In MPACs, PEMs provide these

barriers, which have been shown to significantly slow transport of small molecules and ions.[114, 115, 134, 181] Therefore, MPAC gelation, while certainly influenced by GDL hydrolysis and the dynamic carbonate equilibrium, should also be dependent on the diffusion of materials in and out of the particles/pores. This slowed transport of ions through the films is hypothesized to result in increased gelation time of MPAC gels.

As with any injectable material, tissue near the implanted material must be protected from exposure to hostile conditions such as toxic substances, excessive heat or acidity. Fortunately, alginate gelation utilizing calcium is by nature a mild process that does not produce heat or toxic byproducts. For the internal gelation of alginate, calcium carbonate and GDL levels are usually stoichiometrically balanced as per reactions (4.2-4.4) to produce near neutral conditions at equilibrium.[68] However, the nanofilms utilized in MPAC fabrication have the potential to cause disruption in the intermediate equilibrium kinetics resulting in undesirable transient drops in pH during the gelation process. Thus, it is important to study this process and quantify these effects to ensure the retention of mild gelation conditions.

In addition to the effects of nanofilms on transient properties of the gelation of MPACs, films may also contribute to the mechanical properties of the fully-gelled composite. Desired final mechanical strength of an *in situ* gel depends, to a great extent, on the application. To develop a material for use in a variety of applications, it would be ideal to have control over the mechanical strength in a facile manner. Alginate mechanical properties are generally controlled through crosslink organization and density from a variety of means.[55] Specifically, studies have indicated that increasing

gelation times of alginate material (internal *vs.* external gelation), while keeping the overall calcium quantity the same, results in more homogenous gelation (more uniform crosslink density) and hence greater mechanical strength of the bulk.[68] It would therefore seem plausible that in the case of MPACs, where gelation times would be increased beyond those of traditional alginate gels, the alginate would be very homogenously gelled and mechanically robust. However, MPAC gels have added mechanical complexity over standard alginate hydrogels as they contain a certain volume of pores which should affect the overall mechanical properties of the material by increasing the water volume and altering the density. Therefore, it was hypothesized that MPAC gel strength will not only be influenced by gelation times, but also the concentration of calcium crosslinker and the resulting increase in porosity.

Swelling behavior and mechanical attributes of hydrogels are extremely interconnected properties.[182] Swelling is an important parameter for development of functional implants utilizing hydrogels, as swelling can be advantageous or problematic depending on the application.[183] Hydrogels that swell greatly can effectively lower the concentration of molecule(s) within the pores of the hydrogel, which could result in undesirable functional changes in the implant such as sensor response changes. In addition, stability of the gel in the long term as well as potential host response to the material will be dependent on the swelling behavior and mechanical properties of the gel during the transition. Swelling behavior of alginate, which is commonly influenced by crosslink density and gelation parameters, is hypothesized to be different in MPAC gels due to their porous nature and delayed gelling kinetics.[48, 68, 71, 79]

4.1 Theory and methods

To better understand the complex relationship between the addition of nanofilm coatings and crosslinker/porosity in MPAC fabrication and the mechanical properties and gelation kinetics of the matrix, several sets of experiments were performed at various steps in the hydrogel formation. Small amplitude oscillatory rheological measurements were utilized to determine the effects of nanofilm permeability on gelation kinetic behavior and composite strength. Fluorescence assays were used to determine transient changes in pH during gelation. After gelation, swelling behavior of MPAC hydrogels was evaluated using gravimetric techniques, and mechanical stability of gels immersed in solvent over time was evaluated through immersion dynamic mechanical analysis.

4.1.1 Materials

Poly(sodium 4-styrenesulfonate) (PSS, average M_w = 70,000 Da), poly(diallyldimethylammonium chloride) (PDADMAC, typical M_w range = 100,000-200,000Da) , poly(allylamine hydrochloride) (PAH, average M_w = 15,000 Da), poly(sodium 4-styrenesulfonate-*co*-maleic acid) (PSS-*co*-MA, 1:1 monomer ratio, average M_w = 20,000 Da), alginic acid sodium salt from brown algae (281 cps for a 2% aqueous solution at 25 °C), and 8-hydroxypyrene-1,3,6-trisulfonic Acid (HPTS) were obtained from Sigma and used without further purification.

4.1.2 MPAC fabrication

4.1.2.1 $CaCO_3$ microsphere preparation

$CaCO_3$ microspheres were prepared by precipitation. Briefly, Na_2CO_3 (0.25 M, 8mL) containing 4 mg/mL PSS was stirred vigorously in a 25 mL beaker with a 10 mm triangular stirbar. $CaCl_2$ (0.25 M, 8 mL) was then added to the solution under stirring. The solution was stirred for 30 seconds after mixing, and then agitation was removed and the colloid was allowed to rest for 10 minutes thereafter for particle maturation. Particles were then collected, centrifuged and washed in 5 mM Na_2CO_3 pH 8.0 prior to layer-by-layer deposition.

4.1.2.2 Polyelectrolyte multilayer deposition

The first five bilayers of particles were constructed using the strong positive polyelectrolyte PDADMAC and the strong negative polyelectrolyte PSS in the absence of additional counterions to ensure strong base surface charge with minimal charge sheilding. Additional layers after these first five bilayers were constructed using PAH and PSS-*co*-MA as the weak positive and negative polyelectrolytes respectively for the purpose of creating greater diffusion limitation. Briefly, the particle suspension in 1 mL of 5 mM $NaHCO_3$ (pH 8.0) was centrifuged at 500 g for 30 seconds and resuspended in 1 mL 5 mM $NaHCO_3$ (pH 8.0) with 20 mg/mL PDADMAC and allowed to incubate for 30 seconds. The particles were then centrifuged down at 500 g, supernatant removed, and washed once with 1 mL 5 mM $NaHCO_3$ (pH 8.0). The washed particles were centrifuged down again and resuspended in 1 mL 5 mM $NaHCO_3$ (pH 8.0) with 20 mg/mL PSS and allowed to incubate for 30 seconds. This process was repeated until

there were 5 bilayers of PDADMAC/PSS. After these layers, PAH and PSS-*co*-MA were deposited. A 1 mL solution of 20 mg/mL PAH in 5 mM $NaHCO_3$ (pH 8.0) was added to the packed particles with 5 bilayers, mixed, and allowed to incubate 30 seconds. Particles were then centrifuged at 500 g and resuspended in 5 mM $NaHCO_3$ (pH 7.2). Washed particles were then centrifuged and resuspended in 5 mM $NaHCO_3$ (pH 7.2) with 20mg/mL PSS-*co*-MA and allowed to incubate 30 seconds. PSS-*co*-MA-coated particles were then centrifuged, washed, and resuspended in 5mM $NaHCO_3$ (pH 8.0). This alternating process was repeated until the desired number of bilayers was achieved. LbL deposition was confirmed with zeta potential measurements of aliquots collected during the LbL process. Particles to be analyzed were dispersed in 5 mM $NaHCO_3$ pH 7.2 for zeta potential analysis. Particles were labeled by the total number of bilayers of polyelectrolyte deposited, including both architecture types (*e.g.* 5 bilayers includes only PDADMAC/PSS, while 10 bilayers includes 5 bilayers PDADMAC/PSS and 5 bilayers PAH/PSS-*co*-MA).

4.1.2.3 Alginate composite preparation

Microporous hydrogels were formed by combining PEM-coated calcium carbonate microspheres with alginate and GDL. For all experiments, the molar ratio of $CaCO_3$ to GDL was kept constant at 1:2. Relative levels of $CaCO_3$ and GDL to alginate were varied to observe the resulting effect on mechanical and gelation properties. For the purposes of brevity, a molar ratio of 1:0.27:2 of $CaCO_3$:(carboxylic acids in alginate):GDL, which was shown to have favorable mechanical properties by Kuo and Ma,[68] was considered to be 1x, with 2x being twice the molar quantity of $CaCO_3$ and

GDL, 3x being three times the molar quantity of these elements, *etc*. In all cases, the molar quantity of alginate was kept the same. Gel precursors were made by centrifuging the appropriate amount of $CaCO_3$ particles, removing the storage buffer (5 mM $NaHCO_3$, pH 8.0), and adding deionized water (200uL). Alginate (400 µL of 3% (w/v) in DI water) was then added and mixed. GDL solution of the appropriate concentration (200 uL) was then added and the solution was mixed vigorously and placed in a mold or testing appartus. For each set of characterization experiments, different fabrication parameters including different particle concentrations and numbers of bilayers were tested (Table 1).

Table 1: Fabrication parameters tested in gelation studies utilizing small amplitude oscillatory measurements (I), pH evolution (II), swelling studies (III), and DMA (IV)

		Bilayer					
		5	**10**	**15**	**20**	**25**	**30**
Concentration	**0.5x**	II,III,IV	II,III,IV	II,III,IV	II,III,IV	II,III,IV	II,III,IV
	1x	I, II, III, IV	I, II, III, IV	I, II, III, IV	I, II, III, IV	I, II, III, IV	I, II, III, IV
	2x	II,III,IV	I, II, III, IV	II,III,IV	I, II, III, IV	II,III,IV	I, II, III, IV
	3x	II,III,IV	I, II, III, IV	II,III,IV	I, II, III, IV	II,III,IV	I, II, III, IV

4.1.3 Rheology and gelation points

Measurement of gelation points of crosslinking polymers has historically been accomplished utilizing small amplitude oscillatory measurements. In these tests, reacting sample is placed between a rotating cone and a fixed plate (Figure 19).

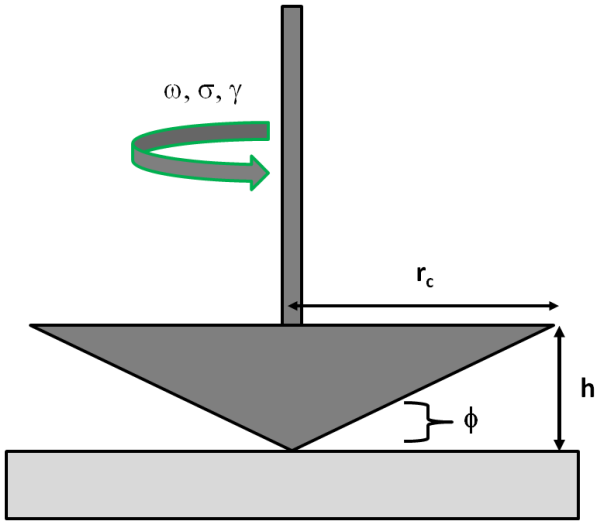

Figure 19: Schematic of a rheology apparatus consisting of a cone and plate.

A strain (γ) is applied in a fixed frequency (ω) sinusoidal form (4.5), while the stress (σ) is measured (4.6). Due to the viscous behavior of viscoelastic materials such as gels, the stress will be phase shifted by the angle δ (4.6). Utilizing the known strain γ, measured stress σ, and measured phase shift δ, the complex shear modulus G*(ω) can be determined, and its components, storage modulus (G') and loss modulus (G'') can be extracted (4.8, 4.9).

$$\gamma(t) = \gamma_o \sin(\omega t) \quad (4.5)$$

$$\sigma(t) = \sigma_o \sin(\omega t + \delta) \quad (4.6)$$

$$G^*(\omega) = G'(\omega) + iG''(\omega) \quad (4.7)$$

$$G'(\omega) = \frac{\sigma_0}{\gamma_0}\cos(\delta) \quad (4.8)$$

$$G''(\omega) = \frac{\sigma_0}{\gamma_0}\sin(\delta) \quad (4.9)$$

$$\tan(\delta) = \frac{G''(\omega)}{G'(\omega)} \quad (4.10)$$

Storage modulus and loss modulus represent the elastic, or "solid-like", and viscous, or "liquid-like", components of the shear modulus respectively. From these measured values, we can determine the interval in time when a material transitions from a viscous-dominant state to an elastic-dominant state as in polymerization and/or gelation of a polymer. This transition point is known as the *gelation point* of the material, and has been shown to occur when G'= G'' and tan(δ)=1 (4.10) in materials that have a stress relaxation exponents of ½, or when the frequency dependence of G' and G'' is equal.[184, 185]

Rheological characterization was performed utilizing an Anton Paar Physica MCR301 with a CP50-1 Cone of 50mm diameter and an angle of 1°. MPAC hydrogel precursors of different microsphere concentrations and different numbers of nanofilm bilayers (Table 1) were mixed and immediately placed on the rheometer. Small amplitude oscillatory measurements were performed with 1% strain and 1Hz frequency (linear viscoelastic region). Crossover of G' and G'' was used to determine gelation points between sample types based upon the observations of frequency-dependent behaviors over time (relaxation exponents at crossover points were observed ≈ ½ and G' and G'' were observed to have equal frequency dependence at crossover). Mechanical

properties G', G'' and tan(δ) values for comparison of end gel strength were determined from the same small amplitude oscillatory measurements 80 minutes after fabrication.

4.1.4 pH changes during gelation

pH evolution during gelation was monitored utilizing the pH-sensitive dye 8-hydroxypyrene-1,3,6-trisulfonic Acid (HPTS). This dye has a single emission peak at ~512 nm and two different excitation peaks located at ~370/400 nm and ~450 nm (Figure 20). As the pH changes, the peak ratio of HPTS changes in a sigmoidal fashion around the isoelectric point, which is near the physiologically-relevant value of ~7.4. Due to the dye's ratiometric nature, differences in excitation source intensity, dye concentration or photobleaching have a greatly reduced effect on signal. This is particularly important in a highly scattering system such as the MPAC hydrogel.

Calibration of HPTS emission ratios for determination of unknown pH within MPAC hydrogels requires certain assumptions to be made. Calibration can be done in two ways: calibrating to dye emission in solutions of differing pH, or calibrating to dye emission within a hydrogel. In the first case, the pH of the calibration solutions are directly measureable utilizing a pH meter, and so precise pH to emission relationships can be determined. However, emission of the dye from an unknown MPAC sample must be assumed to be the same as the solutions utilized in calibration for absolute pH to be accurately determined. In the second calibration method, pH cannot be measured directly within the hydrogel, and so pH within the hydrogel must be assumed to be equal to the solution containing the hydrogel. If the pH within the hydrogel differs from the solution it resides within, error in calibration will result.

To determine pH in unknown hydrogel samples, both calibration curves of the dye (solution and in hydrogel) were constructed. The first calibration was a solution-phase calibration involving dye in titrated buffers. HPTS was dissolved in 0.5 M buffers ranging from pH 3-11 to a concentration of 25 µM. Buffered solutions (200 µL) containing dye were deposited in 96 well plates and 100 µL of paraffin oil was deposited on the aqueous surface to prevent evaporation. Emission at 512 nm was measured using a Tecan model Infinite M200 Pro plate reader utilizing 454 nm and 400 nm excitation with a manual gain of 45 and a z position of 20 mm. The ratio of emission intensities for each buffer solution was used to construct a solution-phase calibration curve. A second calibration curve utilized MPAC hydrogels equilibrated in buffer solutions of varying pH. For this, 200 µL of MPAC precursor solutions of the formulation variables 20BL and 1x (described above) were deposited into individual wells in a 96 well plate and allowed to gel 24 hours. The gels were removed and placed in 0.5 M buffer solutions containing 25 µM HPTS at pH ranging from 3-11. After 24 hours incubation, gels were placed back into the 96 well plates and measured for emission using 454 nm and 400 nm excitation wavelengths to construct calibration curves. Calibration data was fit to a curve utilizing a sigmoidal fit of the form $y = \frac{a}{b+e^{-c \cdot x}} + d$.

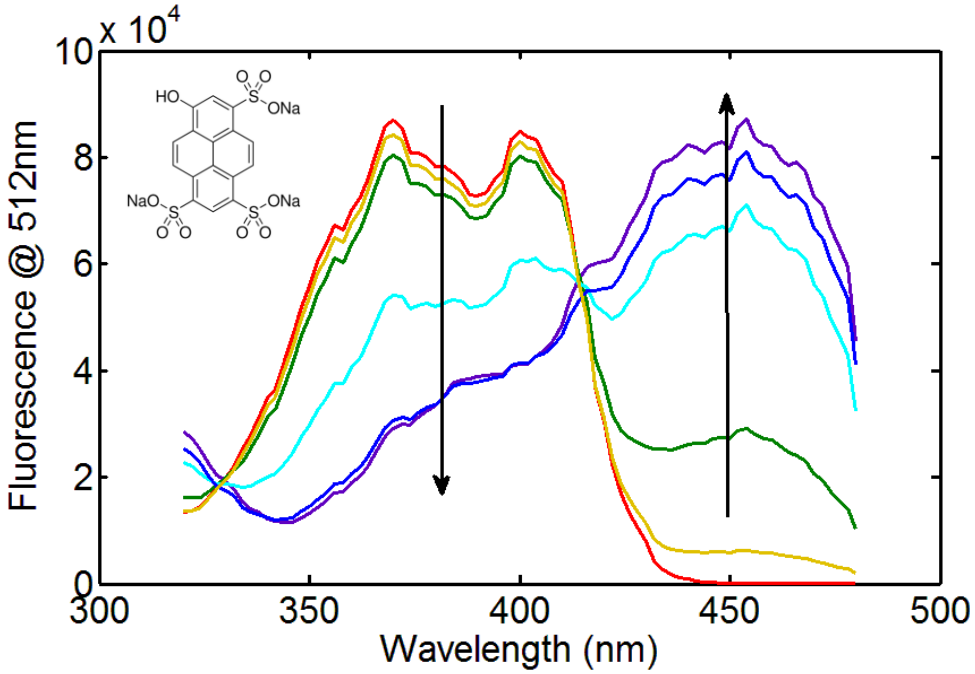

Figure 20: Excitation spectra of 8-Hydroxypyrene-1,3,6-Trisulfonic Acid (HPTS) measured at the emission peak of 512nm.

For pH determination in unknown samples, PEM-coated $CaCO_3$ spheres were suspended in 190 µL DI H_2O, and 10 µL of 2 mM HPTS in DI H_2O was added to this solution. A 400 µL solution of 3% alginate in DI H_2O was added and mixed by vortex. A 200 µL aliquot of GDL solution was then added, and the solution was again mixed by vortex. The pH-sensitive pregels (200 µL each) were deposited into 96-well plates and 100 µL of paraffin oil was deposited on top to prevent evaporation of solvent. Emission of the HPTS (512 nm) from each of its two excitation wavelengths (400 nm and 454 nm) was monitored over a period of hours in a Tecan model Infinite M200 Pro plate reader with a manual gain of 45 and a z position of 20 mm. The ratio of the two emission

values (454/400 nm) was used along with the fitted calibration curve to determine pH within the gelling material.

4.1.5 Composite swelling

Hydrogel swelling is a thermodynamic process involving the solvation of the polymer chains. Solvent molecules (water in the case of hydrogels) move into the polymer network and associate with the polymer chains. This process is complex and depends on many attributes of the polymer such as hydrophilicity of backbone and side groups, polymer flexibility, crosslink density and charge, to name just a few. The swelling behavior for MPAC is particularly important to understand, as it will affect the relative spacing of microdomains within the composite (Figure 21). This has implications for the functional aspect of the gels, as distance dependence between regions may affect sensor or drug delivery function. To determine the extent of swelling for different MPAC formulations, gravimetric analysis of gelled and swollen hydrogels was performed.

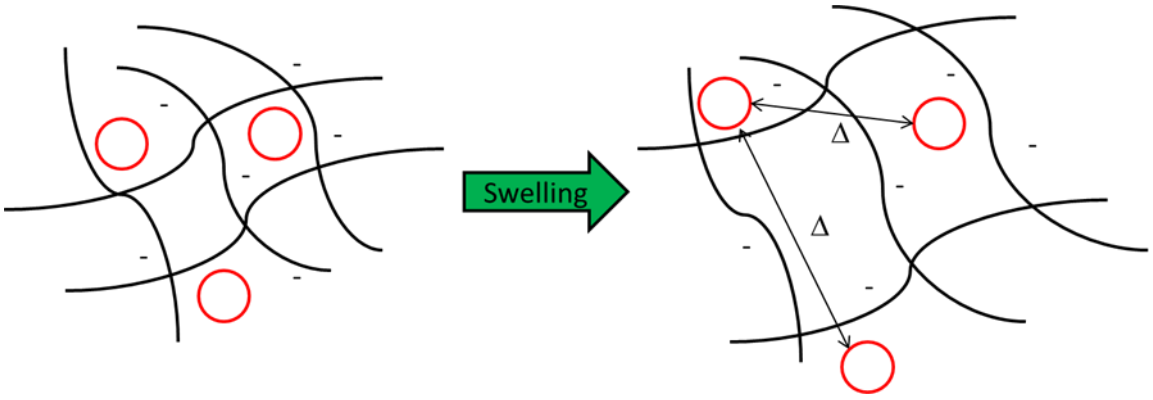

Figure 21: Schematic of the basic structure of the crosslinked hydrogel network. As the hydrogel network swells, distances between pores (Δ) become greater.

MPAC hydrogels of different microsphere concentrations and different numbers of nanofilm bilayers (Table 1) were mixed and cast between two glass slides separated by a 1.5 mm Teflon spacer. Biopsy punches (2.5 mm) were used to punch individual samples from each hydrogel slab. Gel punches were measured for weight prior to swelling (gelled weight) and after 48 hours in 400 µL DI water (swollen weight). Gels were kept at room temperature for the entire experiment. Swelling ratio, though classically defined as swollen weight over dry polymer weight,[186] was instead defined as the difference in swollen weight and gelled weight over gelled weight as this value better represents the property that will be most relevant in an *in situ*-forming system (drying will never occur).

4.1.6 Gel stability and dynamic mechanical analysis

Experiments to determine the extent of swelling, while important, do not provide an insight into of the mechanical changes within the hydrogel during swelling. During swelling, addition of water molecules can cause stretching of the crosslinked polymer

chains, increasing the stress on each (Figure 22). This can manifest as stiffening in the macroscale, and can greatly affect the overall mechanical properties of the hydrogel slab such as modulus and yield strength. As the biocompatibility of a material will depend on the mechanical properties of the material, it is extremely important to understand material stability as a means to improve implant function within various application areas inside the body.[187, 188] Dynamic mechanical analysis (DMA) provides a way to determine mechanical changes in a material during the evolution from one state to another, such as in a hydrogel during swelling. Looking closely at these changes over time, inferences about how the hydrogel physical structure is changing can be made.

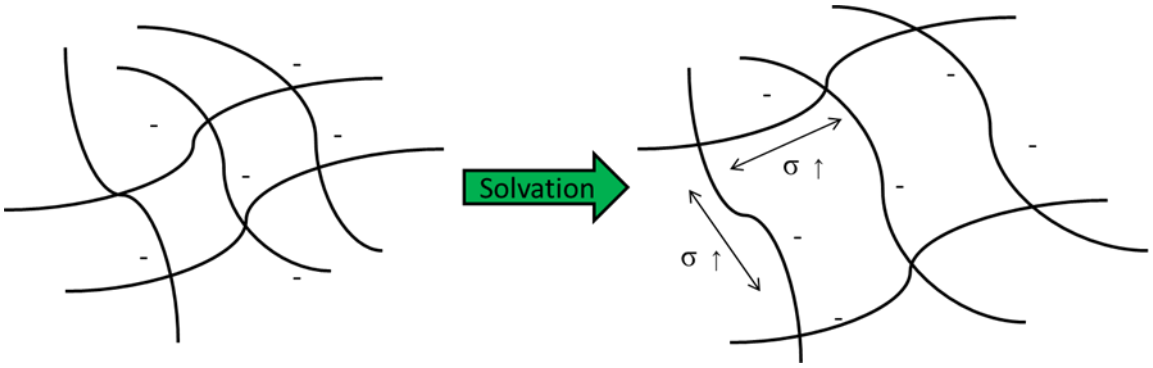

Figure 22: Schematic of the basic structure of the cross-linked hydrogel network. As the hydrogel network swells, individual polymer chains become stressed.

Dynamic mechanical analysis involves the cyclic stress or strain of a material. This can be compression, tension, torsion or in the case of rheology: shear. Due to the nature of the *in vivo* environment, materials for implantation are commonly evaluated for shear and compression moduli, with shear moduli being derived from rheology and

compressive moduli derived from compressive DMA. The same basic viscoelastic characterization principles discussed earlier for rheology apply in compression DMA. Utilizing an instrument such as the one depicted in Figure 23, sample slabs can be compressed sinusoidally in a strain or stress-controlled manner. Compression modulus, dampin

g factor and other relevant mechanical information can be extracted over a period of time. In addition, samples can be immersed in liquid during compression and evaluated for changes in viscoelastic behavior. This technique was applied to determine the changes in compressive moduli of samples of various formulations of MPAC hydrogels.

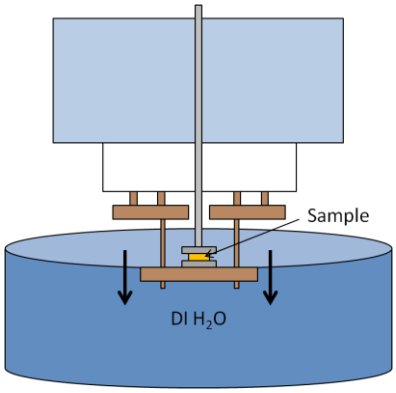

Figure 23: Schematic of the immersion apparatus for dynamic analysis of material swelling.

Dynamic mechanical analysis was performed utilizing a Triton Technology TT Dynamic Mechanical Analyzer. MPAC hydrogel precursors were molded between two glass slides separated by 1.5 mm Teflon spacers. Gels were stored in a humidity

chamber prior to testing. MPAC samples were punched from the slab using 6 mm biopsy punches and placed on the DMA. Samples were then analyzed under cyclic compression at 1 Hz with dynamic strain control and a static force ratio of 1.1. Samples were immersed in DI water and monitored over a period of hours for changes in mechanical properties.

4.2 Results and discussion

4.2.1 Rheological measurements

Rheological measurements were performed on gelling MPAC hydrogels in order to determine the effect of increasing polyelectrolyte multilayers on $CaCO_3$ microspheres on the gelation times of the composite. Increasing numbers of bilayers, representing one of each positive and negative polyelectrolyte polymer layer, would be expected to decrease the permeability of the nanofilm and therefore decrease the flow of molecules in and out of $CaCO_3$ microspheres/pores.

4.2.1.1 Gelation points

Gels fabricated for rheological measurement can be seen in Figure 24, which is a representative example of a 3x gel (maximum porosity) after complete gelation. Pores are dispersed in random fashion within the gelled alginate matrix, as was seen in data presented in Section 3.

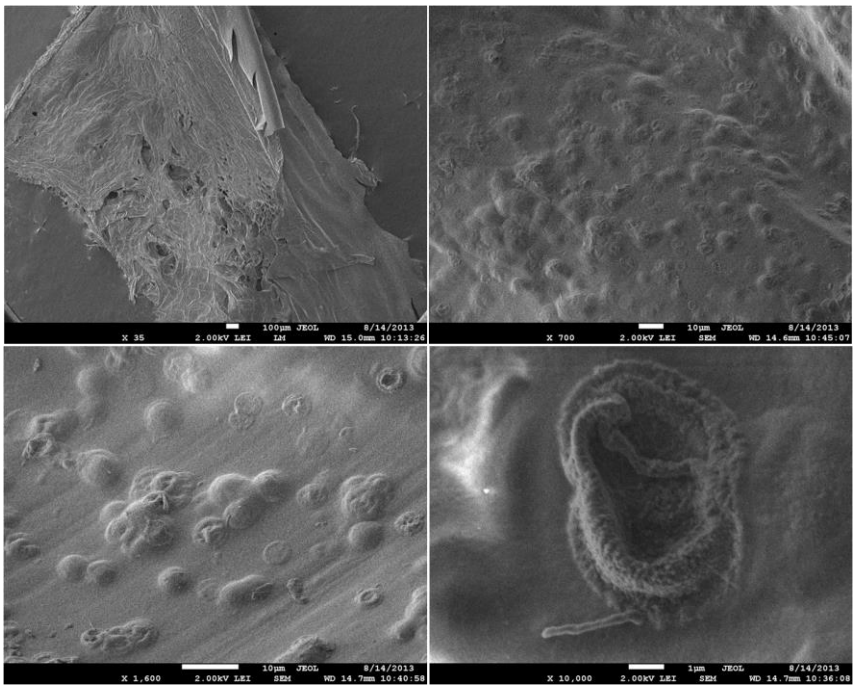

Figure 24: Scanning electron micrographs of 3x MPAC gels used in rheological experiments.

Small amplitude oscillatory measurements were performed on MPAC hydrogels to determine the changes in G', G'', and tan(δ) for gelling samples. In this system, the crossover point of G' and G'' can represent the gel point if the relaxation exponent at gel point is ½ and G' and G'' have the same dependence on frequency. However, unlike other polymer systems with thermal or photocrosslinkable gelation, the MPAC system cannot be interrupted during gelation and tested over a range of frequencies, as it takes several minutes to complete a frequency sweep. Because of this, only frequency sweeps on the slowest gelling system (30BL) could be performed, and only on continuously gelling material. Slopes were approximated and compared to crossover points of G' and G'' during gelation to determine if these crossover points can be used to approximate

gelation point. Slopes of G' and G'' over frequency at different time points were compared as well as complex viscosity over time and frequency. In both cases, approximation of gelation point is required, as the gelation occurs over a shorter period of time than the frequency can be changed. This results in an apparent nonlinearity in frequency dependence. However, it can be clearly seen from G',G'' versus frequency (Figure 25) that the gelation point must occur between time points 21 minutes and 27 minutes, which agrees well with observed crossover points of G' and G'' at 23 min. In addition, looking at complex viscosity, it was determined that the approximate slopes (relaxation exponent) fit the slopes with time, and determine where the relaxation exponent should be ≈0.5 (Figure 26). In this case, we see again that this approximation agrees well with observed crossover point.

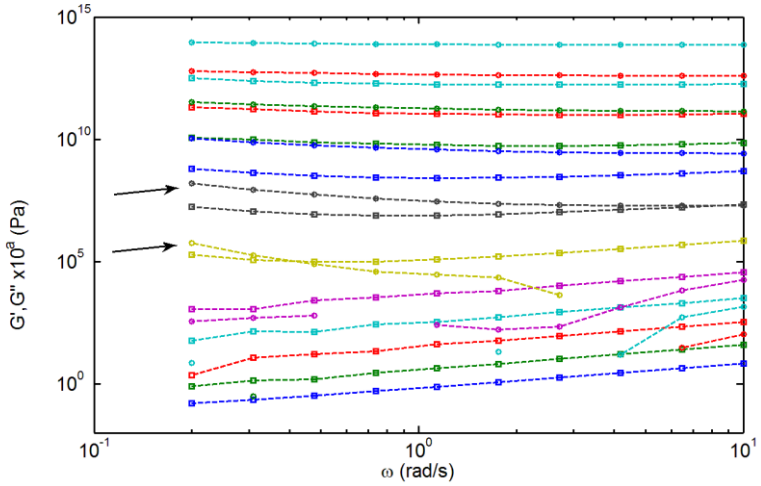

Figure 25: Frequency sweeps of 1x 30BL MPAC gel during gelation plotted against G' and G''. Lines are separated by orders of magnitude for visualization purposes. Circles represent G' while squares represent G''. Arrows point to sweeps where G' and G'' have similar slope values, and hence gel point should occur between these sweeps.

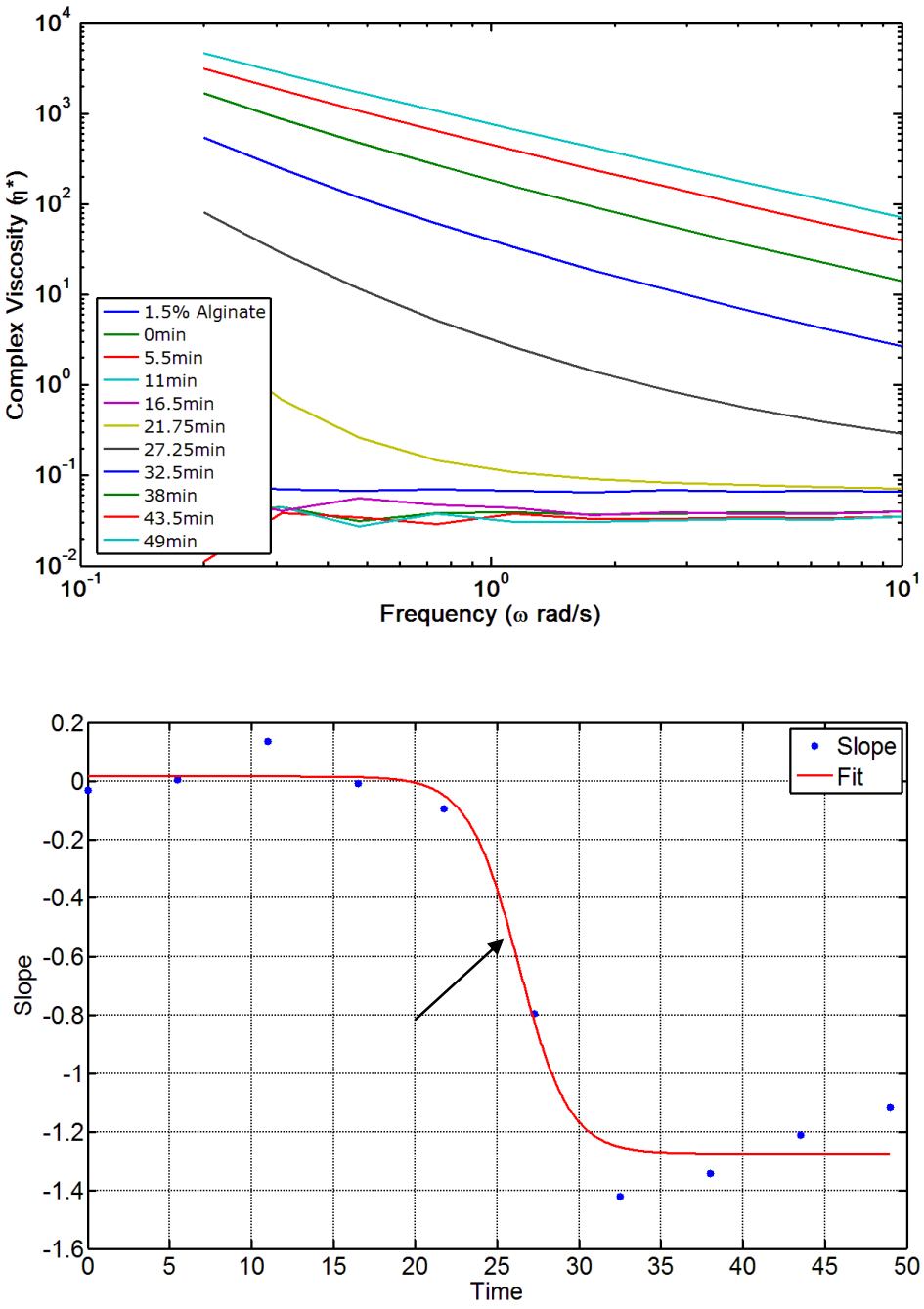

Figure 26: Top: Frequency sweeps plotted against complex viscosity (η*). The point where the slope of the relationship is 0.5 represents the gel point. Using an interpolation of slope values (bottom), we find this point to be in good agreement with transient data of these MPAC gels.

MPAC samples fabricated with different numbers of polyelectrolyte bilayers show significantly different gelation kinetic behavior (Figure 27).

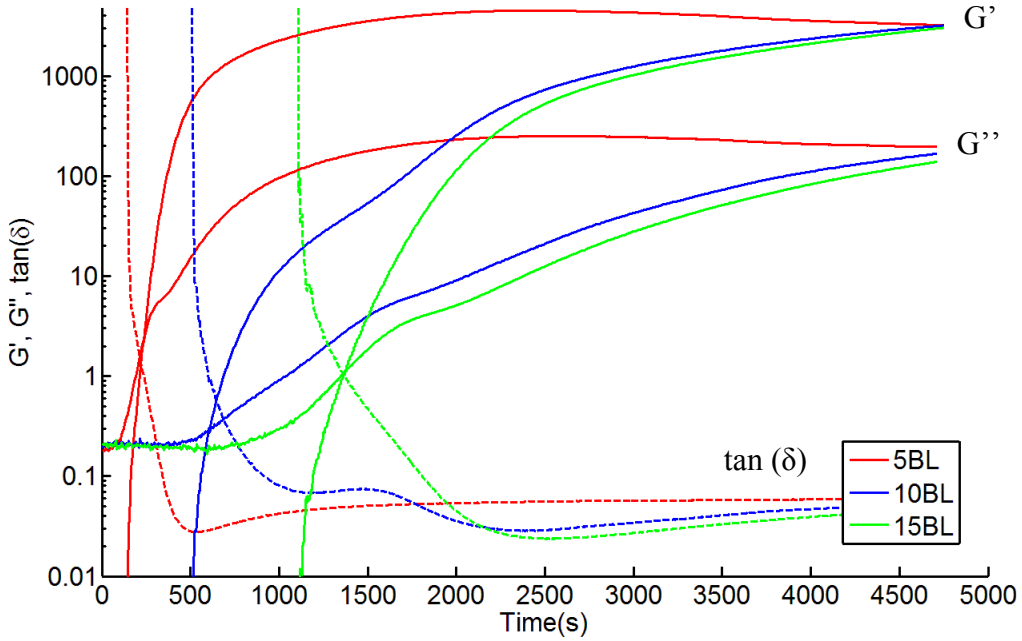

Figure 27: Sample transient data showing the relationship between G', G'', and tan(δ) as a function of time. Crossover points of G' and G'' are defined as the gelation points of the material.

The crossover points of G' and G'' are shifted to greater elapsed time (Figure 28). This indicates that gelation time is being extended with increasing diffusion barrier from the nanofilms. However, above 20 bilayers of polyelectrolyte, the effect of this diffusion barrier seems to fall off.

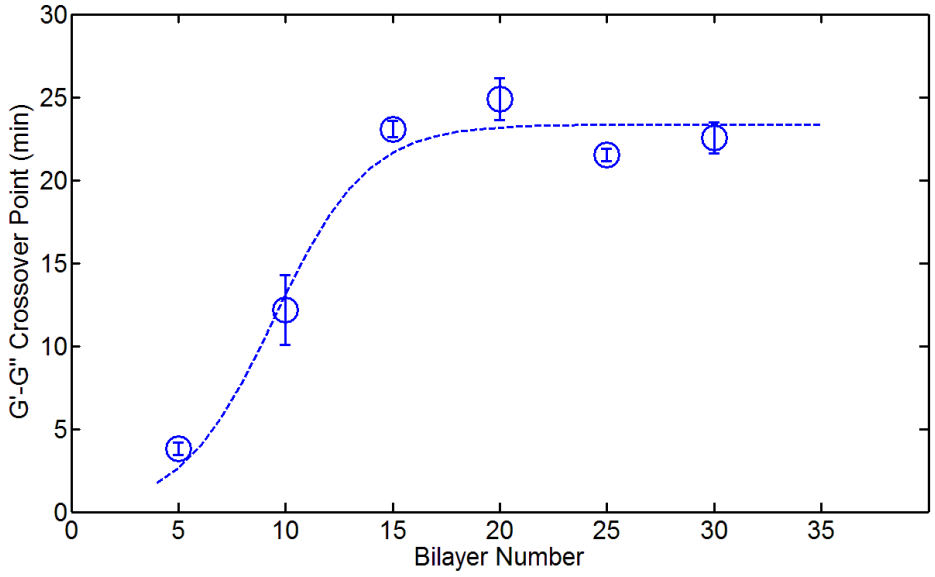

Figure 28: Crossover points of G' and G'', representing the gelation points of 1x MPAC gels with varying numbers of polyelectrolyte bilayers. Error bars represent 95% confidence intervals (n≥3).

This is an interesting observation, as it might be expected that crossover times would continue to increase as diffusion of molecules decreases. This could partially be explained by an observation of the permeability of planar LbL (same formulation) to glucose in the next section, where drastic changes in permeability occur from 0 to 5 bilayers and from 5 to 10 bilayers, but at decreasing magnitude from there on. While the magnitude of diffusivity of carbonates, ions and GDL will be different from that observed for glucose, similar trends are expected for these small molecules.[114, 115, 181] Looking at MPAC hydrogels of different concentrations of particles (Figure 29), we see that a similar relationship between bilayer number and crossover time is seen for all concentrations. However, as concentration of particles increases, crossover time

decreases dramatically. This makes sense, as MPAC made with larger numbers of particles have a larger $CaCO_3$ and GDL concentration and particle surface area. Larger quantities of the crosslinker and increased particle surface areas should correspond to higher magnitude and faster release of ions respectively, resulting in faster gelation of the alginate.

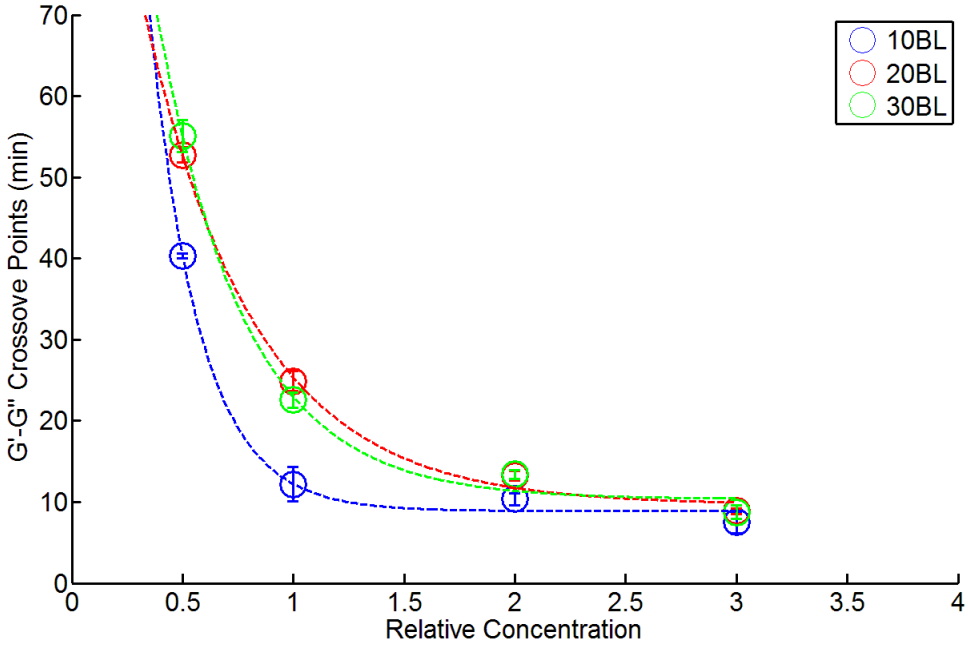

Figure 29: Crossover points of G' and G'', representing the gelation points of 10, 20 and 30BL MPAC gels with varying concentrations of particles utilized in fabrication. Error bars represent 95% confidence intervals (n≥3).

4.2.1.2 Mechanical properties

Shear moduli of gelled MPAC hydrogels was determined utilizing the same small amplitude oscillatory measurements as in gelation kinetic experiments. Gels display dependencies on both concentration and bilayer number (Figure 30, Figure 31, Figure 32). However, dependency on concentration is much more marked than bilayer number. Storage and loss moduli both increase with increased concentration up to 2x, but then decrease in 3x gels. Looking at this trend, it is important to recall that increasing the concentration of $CaCO_3$ particles not only increases the number of crosslinking ions, but also increases the overall porosity of the hydrogel. These are convoluted and opposite effects, and they are not linear. At a certain concentration of ionic crosslinkers (dependent on the concentration and type of alginate), the hydrogel will become saturated with crosslinks and no more can be made. At that point, addition of crosslinking ions in the form of $CaCO_3$ microspheres serves only to weaken the gel, as it produces higher porosity without any increase in crosslinking. This effect, which is observed in similar porous matrices,[189] seems to be occurring between 2-3x concentrations, and will be an important consideration for future work that is dependent on the mechanical integrity of the MPAC system.

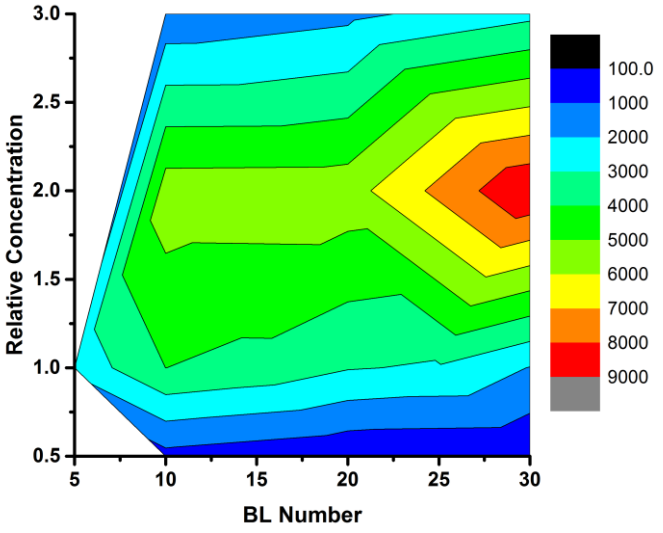

Figure 30: Storage modulus, G', of MPAC gels as a function of differing concentrations of particles and different numbers of polyelectrolyte bilayers.

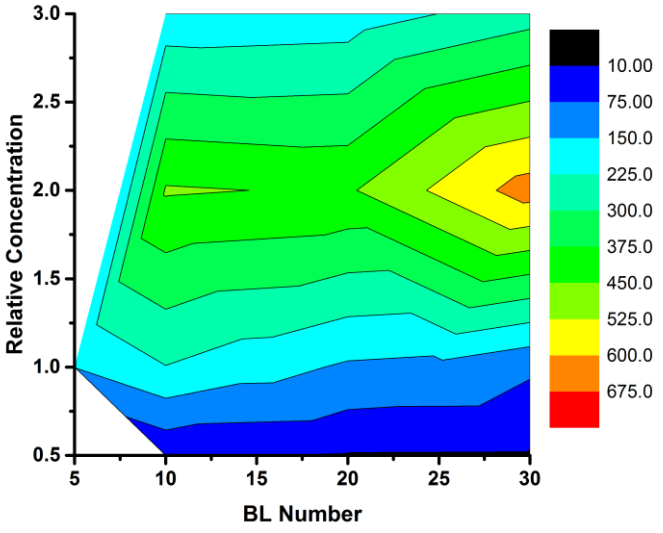

Figure 31: Loss modulus, G'', of MPAC gels as a function of differing concentrations of particles and different numbers of polyelectrolyte bilayers.

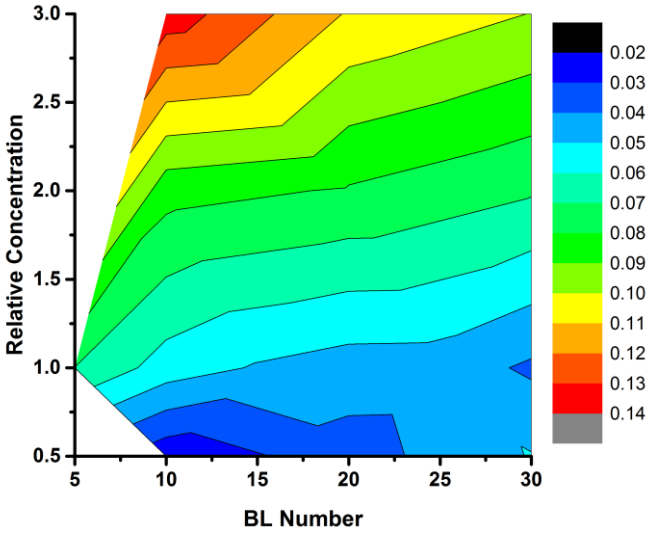

Figure 32: Damping factor, tan(δ), of MPAC gels as a function of differing concentrations of particles and different numbers of polyelectrolyte bilayers.

Dependence of shear moduli upon bilayer number is much less striking than dependence upon particle concentration. However, there is a clear relationship of increasing numbers of bilayers resulting in increased shear moduli. Looking at damping factor, tan(δ), it can be concluded that increasing numbers of bilayers decreases the elastic behavior of a MPAC. So, while the MPAC gels with higher numbers of polyelectrolyte bilayers have generally increased strength, they display a much more viscous behavior overall.

4.2.2 pH changes during gelation

In the alginate internal gelation mechanism, the hydrolysis of glucono-δ-lactone in water produces gluconic acid, lowering the pH of the solution. This drop in pH in turn causes the dissolution of the $CaCO_3$ and a subsequent increase in pH.[68] This complex interdependent process produces overall changes in hydrogel pH during the gelation process. However, in MPAC gelation, there is the added complexity of transport of GDL/gluconic acid and calcium through the nanofilms. This is the basic physical phenomenon responsible for the gelation extension, and this effect alters the pH evolution during gelation. Changes in pH during gelation could have a dramatic impact on the utility of MPAC hydrogels for *in vivo* application. Ideally, pH values should remain near neutral to reduce the stress experienced by tissue near the injection site. While the systems are stoichiometrically balanced to remain near neutral, there is a possibility that pH evolution during gelation could produce extremes in a severely-delayed system such as in MPACs.

Calibration utilizing both solution phase and "in hydrogel" methods can be seen in Figure 33. Both fit methods result in a sigmoidal relationship between emission ratio and pH with inflection at ~7.4,which is characteristic of HPTS.

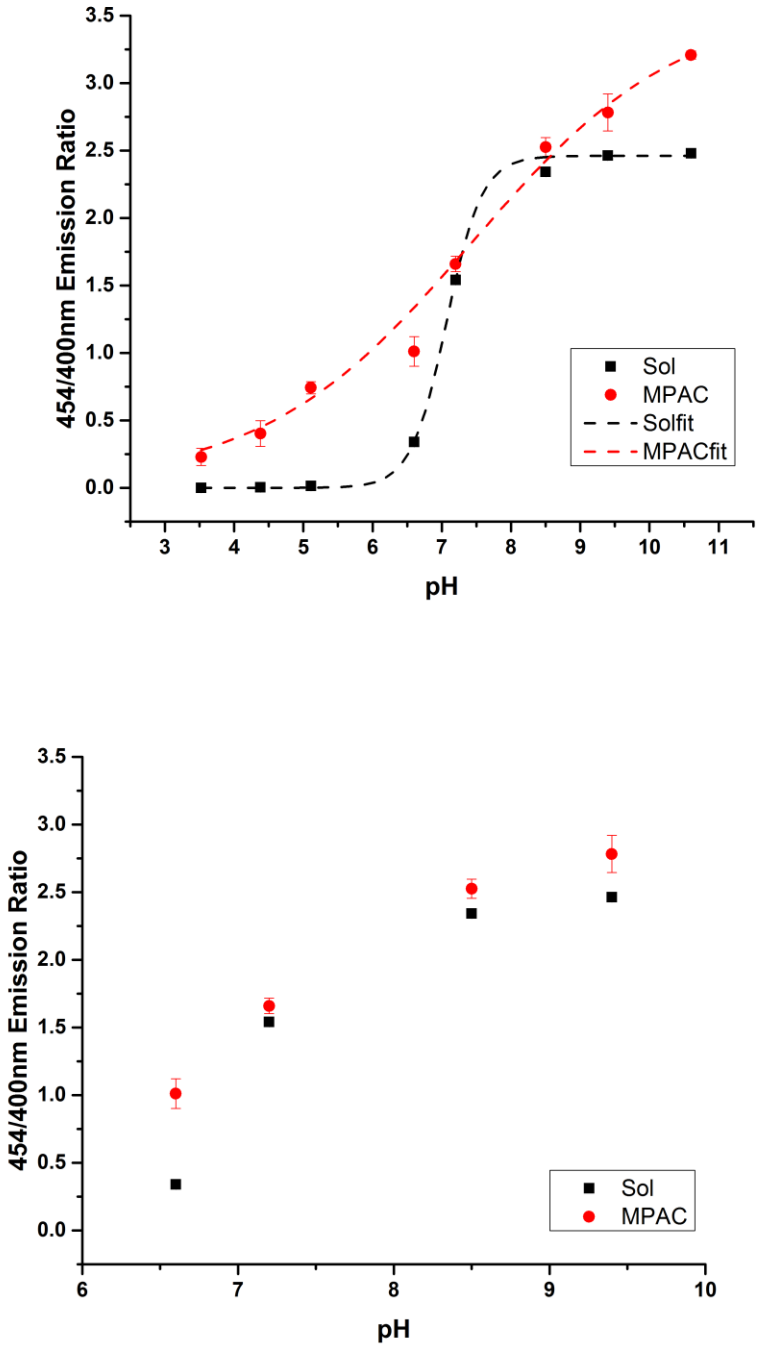

Figure 33: Calibration curves for HPTS in solution (black) and in MPAC gels equilibrated in buffer solution (red). Top: Full scale from pH 3.5 to pH 10.5. Bottom: Region of interest between pH 6.5 and 8.5. Error bars represent 95% confidence intervals (n=3).

In the case of the "in hydrogel" calibration, ratios deviate from solution phase calibration at pH values outside 6.5-9.5. This is to be due to deviation between inner gel pH and solution pH. At low pH, it was observed that hydrogels had measurable absorbance/excitation at 454nm, which should not occur for HPTS at these apparent pHs (Figure 34). This absorbance difference can be observed macroscopically (Figure 34).

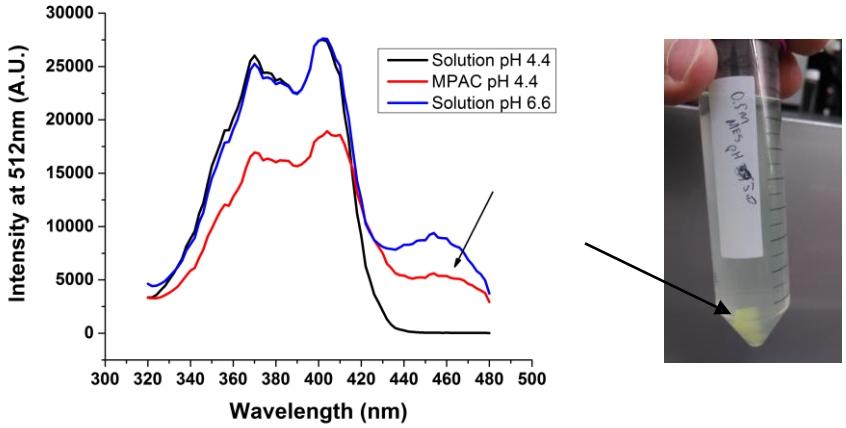

Figure 34: Left: Representative excitation scans of solution and MPAC calibrants. Right: Observable absorbance differences in gels compared to surrounding solutions.

In these calibration samples, the pH inside of the hydrogel is different than the solution it is equilibrated within. As such, this calibration method cannot be utilized for pHs below ~6. This is of little consequence, as HPTS cannot be used effectively to measure pH below 6 even in solution, as emission ratios below this value are not significantly different from one another. Within usable and relevant pH ranges (~6 -9.5), solution and "in hydrogel" calibrations appear to be very similar (Figure 33, bottom).

However, due to the inclusion of accurate and precise calibration points at the low pHs, the solution phase calibration fit is a better choice for accurate determination of pH in unknown samples and was utilized to determine pH in MPAC samples during gelation.

Evolution in pH of MPAC hydrogels during gelation display dependence on concentration of $CaCO_3$ particles and bilayer numbers (Figure 35). Change in pH within MPAC hydrogels show a consistent tri-phasic pattern during the gelation process for all gel types (Figure 35). Upon mixing, the pH increases to a local maximum for all samples except the lowest number of polyelectrolyte bilayers. This effect is the dominant effect in MPAC hydrogels fabricated with higher concentrations of particles. As such, this effect is likely due to the release of carbonate ions, as these are more numerous in higher particle concentrations, and these ions represent the only source of base in the system.

After the initial increase, the pH evolution then enters a secondary phase, where differences between bilayers and particle concentrations are more readily apparent. Here, the pH continues to increase to another local maximum, with absolute value at a range of pH values dependent on concentration and bilayer numbers. This phase dominates in MPACs fabricated with lower concentrations of particles and lower numbers of bilayers. Though in general, higher concentrations of particles and bilayer numbers results in a higher local maximum in this phase. Additionally, the local maximum occurs earlier in the pH evolution for samples prepared with higher concentrations of particles and increasing numbers of bilayers. Due to the increase in pH during this phase, it is likely caused by carbonate ions as in the first phase.

However, in this case, the release is delayed significantly from the initial burst. There could be several possible reasons for this, including diffusion of the dye into the higher pH capsules or a secondary release of carbonate ions due to a time-dependent effect such as GDL diffusion or hydrolysis. Due to the complexity of the system, it is unclear what is causing this secondary phase, but it can be inferred that it is dependent on numbers of bilayers, and hence diffusion in and out of the hydrogel pores.

In the final phase of the pH evolution, pH decreases to an equilibrium value for all samples. In nearly all cases, this value is around pH 6.5, but in the cases of 0.5x, the value approached depends greatly on bilayer number. This phase is likely due to the hydrolysis of GDL into gluconic acid. The acidification of the environment shifts the equilibrium of the carbonate-bicarbonate-CO_2 reaction, and eventually settles at a specific pH. Difference in end pH can theoretically only be due to species leaving the system, as the amount of GDL and $CaCO_3$ in the system is controlled and should always reach the same pH equilibrium value. The only species able to leave the system is CO_2 in gas form, and so production of CO_2 in some systems could be the cause of different equilibrium pH values.

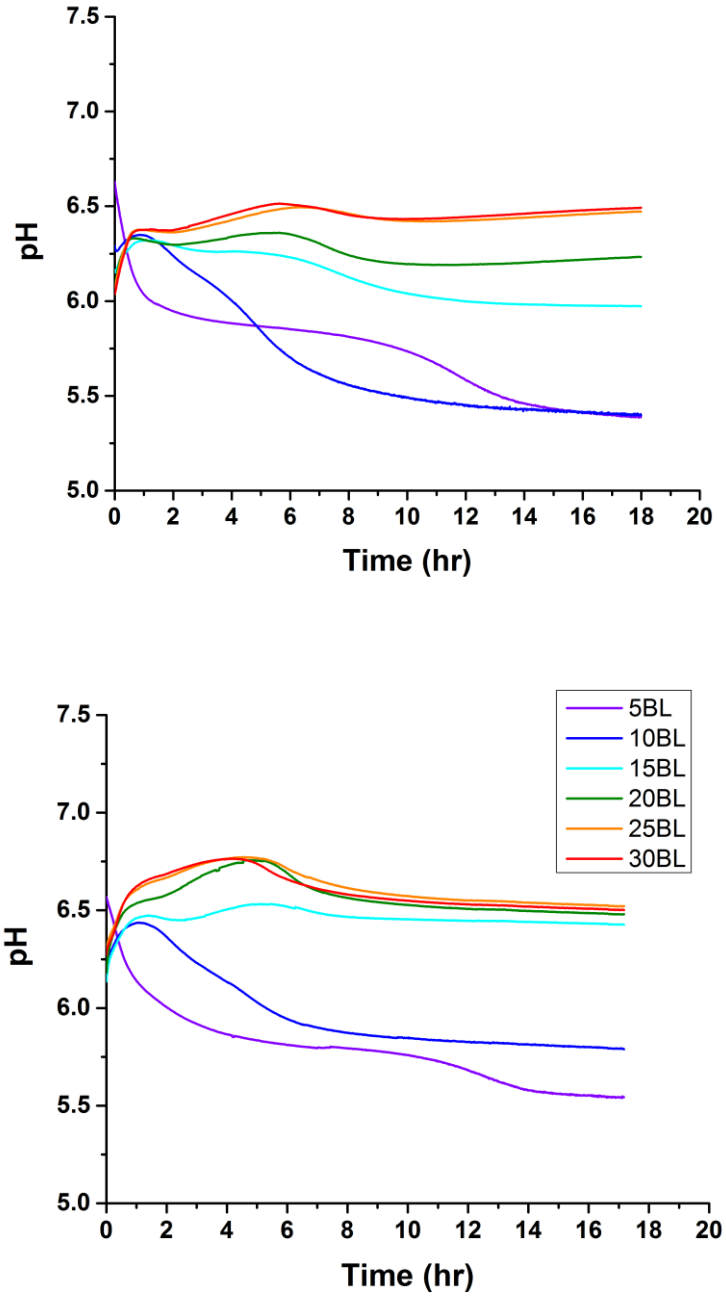

Figure 35: pH evolution of MPAC hydrogels as a function of time. Separate graphs from top to bottom represent gels of different particle concentration (0.5x, 1x, 2x, 3x) while individual curves represent gels of different numbers of polyelectrolyte bilayers (5, 10, 15, 20, 25, 30 BL).

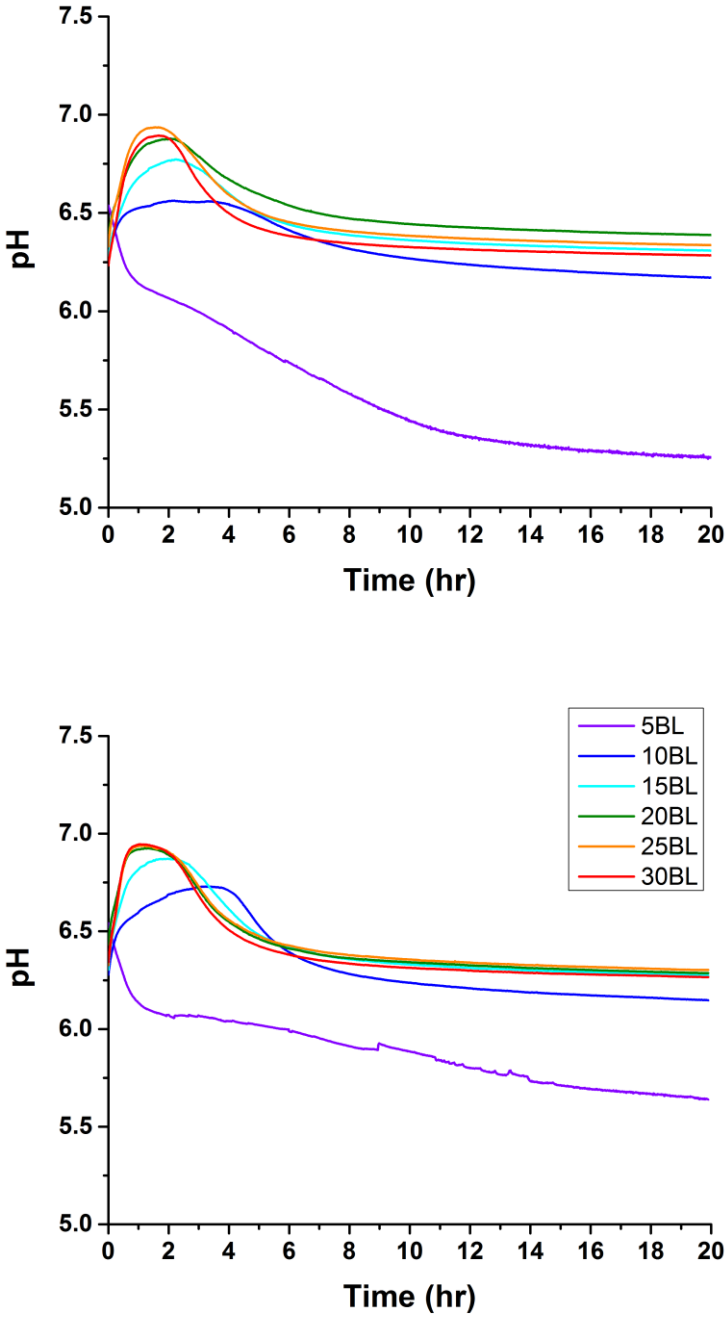

Figure 35: Continued.

4.2.3 Composite swelling

Swelling of the gelled MPAC hydrogels is an important property to understand both for *in vitro* and *in vivo* applications. This is particularly true for sensors, where differences in distance between pores could drastically impact sensor response. To determine the extent of swelling for different MPAC formulations, gravimetric analysis of gelled and swollen hydrogels was performed.

MPAC gel swelling displayed a strong dependence on concentration (Figure 36). Generally, gels made with fewer particles resulted in a higher degree of swelling. This is expected, as gels made with fewer particles should have fewer crosslinks to hold the alginate chains together. At a concentration of 2x and above however, additional calcium did not result in a change in swelling, as 2x and 3x gels did not swell above their initial weight when exposed to DI water.

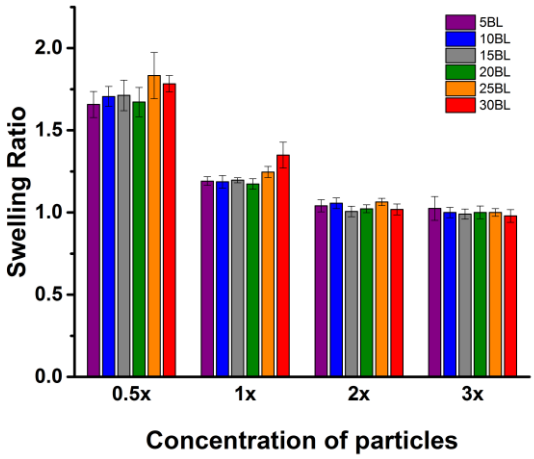

Figure 36: Swelling ratio of MPAC gels of different particle concentrations and numbers of polyelectrolyte bilayers. Error bars represent 95% confidence intervals (n=5).

The behavior observed for these gels (increasing elastic behavior and decreased swelling) agrees well with other observations of polymer systems with increasing amount of crosslinks.[182] In the case of MPAC, it seems that swelling ratio is mostly dependent on this attribute of the network. However, since swelling ratio was defined as the ratio of swollen weight to weight after gelation, the swelling ratio does not indicate density of the material.

When we look at the actual weights of the gelled material for a given punch size (2.5mm), we see that there is a dependence on bilayer number (Figure 37). In most cases, increasing numbers of bilayers results in increased punch weight and swell weight, but these effects cancel each other out when viewed as a swelling ratio. This also occurs predominantly in 0.5x and 1x gels. Based upon these data, we can say that polyelectrolyte bilayers do indeed affect the physical structure of the hydrogel as it relates to solvent interactions, even if the overall swelling ratio is not affected.

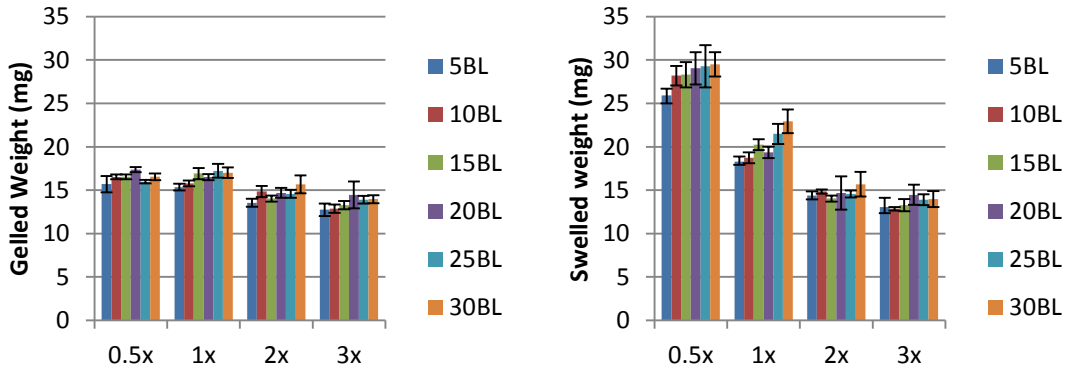

Figure 37: Left: Original (gelled) weight of 2.5mm diameter biopsy punches of MPAC hydrogels of different fabrication parameters. Right: Swelled weight of the same hydrogel punches. Error bars represent 95% confidence intervals (n=5).

4.2.4 DMA of solvent-exposed gels

While swelling behavior can give some indications of polymer physical structure, it can only give information on a base state versus an equilibrium state. It does not give us information on any changes in physical properties during the transition to equilibrium. For many hydrogel systems, it is only important to understand the equilibrium properties of the gels, as they will only be used in this state. In the case of an injectable, *in situ*-forming gel such as MPAC, it is very important to understand this interaction, as the gels will equilibrate in the environment the gel resides.

Dynamic mechanical analysis of MPAC gels gives a glimpse of the changes occurring within the hydrogels after exposure to DI H_2O. Figure 38 illustrates the general stiffening behavior (based upon the ratio of modulus to initial modulus ($E'(t)/E'_i$)) exhibited by gels of a particular concentration of particles.

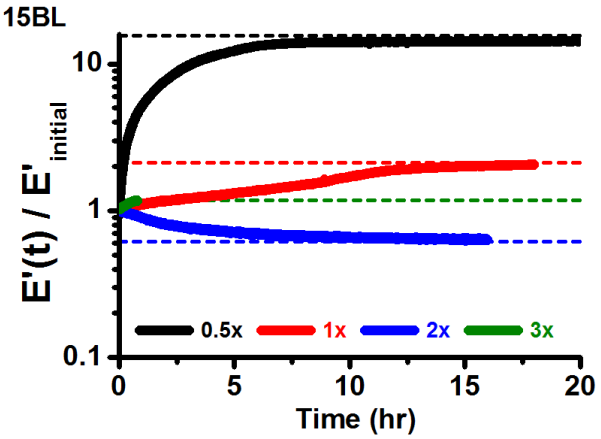

Figure 38: Representative MPAC swelling behavior shown as transient changes in E_f/E_i over time based upon particle concentration.

Here, in gels fabricated with a various particle concentrations, we see two different effects on different time scales. The first is a fast effect, which is dominant in gels with higher numbers of particles. In gels of lower particle concentration, a second slower effect dominates the equilibrium transition. At 1x concentration, gels exhibit an equilibrium transition where the two transient effects occur on separate time scales, and so are easily visible. These effects likely represent two important physical phenomena: diffusion-based solvent sorption and polymer chain relaxation. Sorption involves the movement and organization of solvent molecules in and around the polymer chains. This is a relatively fast effect, which is dependent on the diffusion of solvent through the hydrogel.[190, 191] The resulting flux of solvent molecules into the hydrogel results in initial swelling, and hence stiffening of the hydrogel. This effect is evident in all formulations of MPAC, but its relative impact on mechanical properties depends greatly on particle concentration.

The second effect, which is on a much longer timescale, most likely represents polymer chain reorganization. This involves the physical movement of polymer chains and solvent molecules within the hydrogel into a more energetically stable state.[192-194] This effect generally takes longer than solvation, as there are numerous intermediate pseudo-stable states in which the polymer can adopt.[193] This reorganization is dependent on the strength of the solvent interaction with the polymer chains and the relative conformational freedom of the polymer backbone and side chains.[194] In MPAC hydrogels with lower numbers of crosslinks, such as the 1x and 0.5x concentrations,

polymer chains will have more conformational freedom, and so theoretically will be able to reorganize more extensively.

These complex equilibrium transitions were quantified with two different descriptive values: E_f/E_i and τ. E_f/E_i represents the ratio of equilibrium modulus (E_f) to initial modulus (E_i). τ is a time constant representative of the time it takes for the gel to reach equilibrium state from initial state, and includes contributions from both $\tau_{solvation}$ and $\tau_{reorganization}$. Figure 39 depicts the relationship between E_f/E_i and concentration or bilayer number utilized in MPAC fabrication.

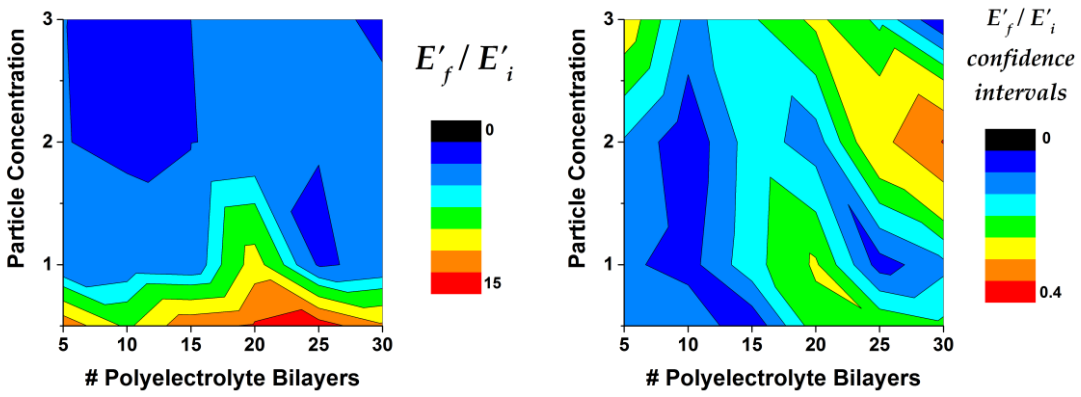

Figure 39: Left: E_f/E_i plotted against MPAC fabrication parameters of particle concentration and polyelectrolyte bilayers. Right: 95% confidence intervals as a ratio of the mean.

E_f/E_i has a strong dependence on concentration of particles utilized in the MPAC formulation. This is expected from the swelling data, as 0.5x and 1x gels exhibited significant swelling, and stiffening behavior is commonly associated with swelling.[182]

There is little dependence on bilayer numbers, which is also consistent with swelling behavior described previously.

In contrast to the stiffening behavior, equilibration times were different over a range of both concentrations and bilayer numbers. Equilibration time constants displayed strong dependence on both concentrations of particles and polyelectrolyte bilayers utilized in fabrication (Figure 40). The greatest τ values occurred at 1x particle concentrations between 10 and 20BL, with a maximum at 20BL. Samples in this region exhibit multiphasic behavior, as evident from Figure 38.

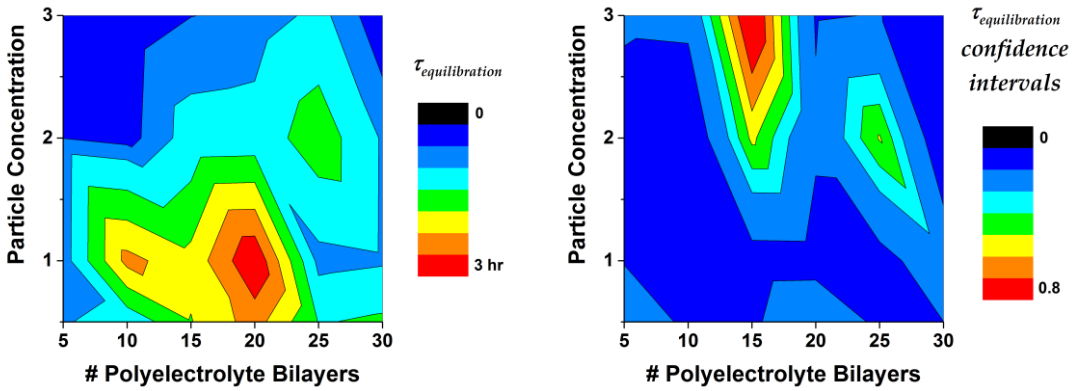

Figure 40: Left: Tau values plotted against MPAC fabrication parameters of particle concentration and polyelectrolyte bilayers. Right: 95% confidence intervals as a ratio of the mean.

As mentioned before, the time constant τ is a convolution of two different processes: solvation and matrix reorganization, each with their own time constants: $\tau_{solvation}$ and $\tau_{reorganization}$. It is important to note that in all MPACs, both solvation and matrix reorganization do occur, and so each sample will have a $\tau_{solvation}$ and $\tau_{reorganization}$

component to its equilibrium time constant. However, in cases where reorganization is infinitely slow, such as in highly crosslinked networks, the matrix reorganization component of τ is such that $\tau_{reorganization} \rightarrow \infty$. Therefore, the convolution of $\tau_{reorganization}$ and $\tau_{solvation} \rightarrow \tau_{solvation}$ and $\tau \approx \tau_{solvation}$. This is evident in gels of 2x and 3x concentrations, where τ is short. In lower crosslink concentrations, as in 0.5x MPAC, the $\tau_{solvation}$ and $\tau_{reorganization}$ are on the same timescale, and so appear as a single exponential (Figure 41).

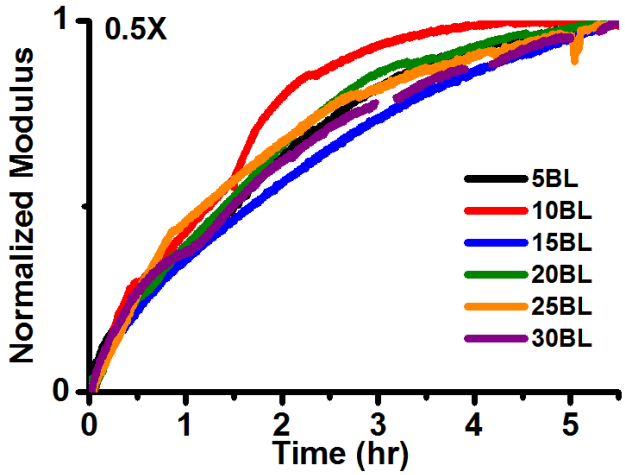

Figure 41: Representative 0.5x MPAC normalized modulus changes as a function of bilayers utilized in fabrication.

However, the most interesting behavior occurs at 1x concentrations at between 10 and 20 bilayers, where equilibrium time constants are large. This area represents an area in which solvation and matrix reorganization are occurring in different time scales (Figure 38, Figure 42). Here, matrix reorganization is much slower than in 0.5x

MPACs, and the contribution from this slow matrix reorganization causes the overall equilibration time to be very slow.

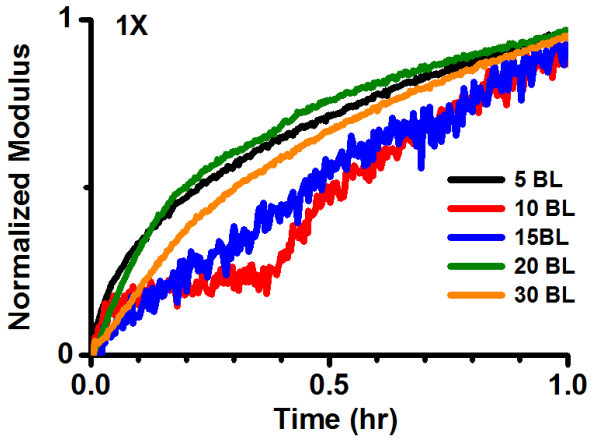

Figure 42: Representative 1x MPAC normalized modulus changes during solvation.

Overall, while equilibrium moduli ratios (stiffening) of MPAC hydrogels depend almost exclusively on concentration of particles utilized in their fabrication, the timescale to reach equilibrium is a much more sensitive property. Both particle concentration and bilayer numbers effect this transition time, predominantly at 1x concentration and from 10-20 bilayers. While this work represents the most basic solvation-reorganization model (water), it represents a basis for the study of more complex equilibration mechanisms involving protein adhesion, ion exchange, and degradation.

4.3 Conclusions

The results presented in this section reveal the impact that MPAC fabrication parameters have on the mechanical and kinetic properties of the hydrogels. Both particle/pore concentration and bilayers utilized in the composite have different effects on the gelation of the material, and hence its end properties. As such, these parameters have a definitive impact on every aspect from gelation kinetics to pH evolution. Even in the case of swelling, where nanofilm number does not seem to affect behavior, close examination with dynamic mechanical analysis reveals that nanofilms do indeed have influence.

Knowledge of the parameters that control the properties of MPAC composites is a critical step in developing a functional injectable material containing sensing or therapeutic elements. Specific design of the implantable system will rely on the knowledge of implant gelation kinetics for handling, mechanical strength for long-term residence in tissue, and swelling behavior for prediction of sensor/therapeutic response/release behavior. Additionally, experiments such as the dynamic mechanical analysis in water create a basis for the future evaluation of these systems' degradation profiles under *in vivo* conditions in which other processes such as ion exchange and hydrolytic cleavage occur.

5. SENSING MPAC HYDROGELS

In order to prove the utility of MPAC hydrogels as sensor matrix materials, MPAC hydrogels were fabricated containing oxygen and glucose sensing chemistry. Fabrication parameters including numbers of polyelectrolyte-coated $CaCO_3$ particles, polyelectrolyte nanofilm architecture, and nanofilm permeability to glucose were varied and changes in sensor response characteristics were observed. After a brief introduction to luminescence lifetime sensor theory, the fabrication, testing, and evaluation of sensor response of MPAC oxygen and glucose sensors are discussed.

Oxygen-sensitive phosphors, as explained briefly in the background section, report oxygen concentrations in their immediate environment through changes in their luminescence properties. This effect is due to the collisional quenching of the molecule by oxygen. This quenching manifests as a decrease in luminescence intensity and lifetime according to the Stern-Volmer equation[166]:

$$\frac{\tau_0}{\tau} = \frac{I_0}{I} = 1 + K_{sv} \cdot [O_2] \quad (5.1)$$

According to this relation, luminescence of the dye is dependent on two factors, oxygen concentration $[O_2]$ and the Stern-Volmer constant K_{SV}.[166] K_{SV} is an empirically-derived value and is dependent on the surrounding environment. It can be broken down into two component parts: $K_{SV} = k_q\tau_0$, with τ_0 representing the native lifetime of the dye when no quencher is present and k_q representing the bimolecular quenching constant For a two component system such as with a single dye and a single quencher, the diffusion-controlled bimolecular rate constant k_0 is given through the Smoluchowski equation:[166]

$$(5.2) \quad k_0 = \frac{4\pi N}{1000}\left(R_f + R_q\right)(D_f + D_q)$$

In this relation, k_0 is dependent on the collision radii of the fluorophore and quencher, R_f and R_q respectively and the diffusion coefficients of the two, D_f (fluorophore) and D_q (quencher). N represents Avogadro's number. k_0 can be related to the bimolecular quenching constant by $k_q = f_Q k_0$, where f_Q is the quenching efficiency.[166] Through these relationships, we can see that the quenching behavior of a dye will be dependent on the relative diffusivities of the dye and quencher, the quenching efficiency and the quenching radii of the components. Since systems using the same dye and quencher will have the same quenching radii and quenching efficiency, and temperatures will be kept constant for comparison, the main difference between different dye encapsulation/immobilization methods will be the diffusivity of the components through the matrix. As a result, K_{SV} must be determined for any new dye immobilization material in a sensor so that the sensor lifetime or intensity will accurately reflect the true oxygen concentration. This is accomplished by measuring the lifetime of a particular dye at various quencher concentrations within the sensor. These lifetime values can be plotted in the form of equation (5.1), where a linear fit can be applied to determine the slope, K_{SV}. It is important to note that this relation is the ideal case, but in reality there can be different populations of dye with different accessibility to quencher, which will cause the Stern-Volmer relationship to deviate from linearity.

Our laboratory's glucose-sensitive chemistry relies upon oxygen-sensitive phosphors in combination with the enzyme glucose oxidase.[133, 167, 168, 170, 195-197] Glucose

oxidase is a glycoenzyme which catalyzes the reaction of glucose and oxygen in the following simplified reaction:

$$\text{Glucose} + O_2 \xrightarrow{\text{GOx}} \text{Glucono-}\delta\text{-lactone} + H_2O_2 \quad (5.3)$$

The sensing chemistry works by consuming oxygen when glucose is present, which can be measured by evaluating the luminescence properties of the oxygen-sensitive dye. As glucose levels increase, the reaction depletes increasing quantities of oxygen, causing the phosphor's intensity and lifetime to increase accordingly. While the mechanism of transduction is straightforward, the tuning of sensor response is a more complicated challenge. The reaction of glucose oxidase is highly dependent on the concentration of enzyme as well as the relative concentrations of the substrates glucose and oxygen, which are turn are dependent on diffusion from their source (blood vessels *in vivo*). Thus, the correct balance of substrate flux is required in order for the sensor to function at the desired glucose concentration (40-400mg/dL).

In the past, our lab has utilized polyelectrolyte multilayers, specifically PSS and PAH, as a means to control the flux of glucose and oxygen to the sensing chemistry.[133] It has been shown that decreasing the permeability of glucose in relation to oxygen can tune the sensor response characteristics of microsphere-based sensor towards extended analytical range.[133] However, it has not been shown in bulk materials such as an MPAC hydrogel.

5.1 Theory and methods

The basic properties of the oxygen and flux-based glucose sensors are dependent on the knowledge of the quenching behavior of the oxygen-sensitive phosphor as well as the diffusional properties of the diffusion barrier material. For enzyme-based glucose sensing in particular, glucose and oxygen diffusion control is of paramount importance to the function. To ensure an effective measure of glucose concentrations as they change, glucose diffusion in the sensor must be slowed in relation to oxygen diffusion so that there is an excess of oxygen in the system. To characterize the MPAC oxygen and glucose-sensing materials, quenching behavior and glucose-dependent responses were measured for MPAC gels of different fabrication parameters including $CaCO_3$ particle concentration and numbers of polyelectrolyte bilayers. These quenching and response characteristics were compared against the diffusional properties of planar nanofilms of the same numbers of layers and architectures.

5.1.1 Materials

Poly(sodium 4-styrenesulfonate) (PSS, average M_w = 70,000 Da), poly(diallyldimethylammonium chloride) (PDADMAC, typical M_w range = 100,000-200,000Da) , poly(allylamine hydrochloride) (PAH, average M_w = 15,000 Da), poly(sodium 4-styrenesulfonate-*co*-maleic acid) (PSS-*co*-MA, 1:1 monomer ratio, average M_w = 20,000 Da), and alginic acid sodium salt from brown algae (281 cps for a 2% aqueous solution at 25 °C), were obtained from Sigma and used without further purification. Pd(II) meso-tetra(4-carboxyphenyl)porphine (PdTCPP) was obtained from

Frontier Scientific. Glucose oxidase from *Aspergillus niger* (GOx, 257 U/mg solid, 71.1% protein by Lowry, *ca.* 160 kDa) was obtained from BBI Enzymes

5.1.2 Material loading

GOx and PdTCPP loading in $CaCO_3$ microspheres is a critical variable in the formulation of oxygen and glucose-sensing MPAC gels. Loading of each of the sensing chemistry components can affect the signal intensity (affected by dye concentration) and sensor response and stability (affected by enzyme loading) of the final sensor. Because of the importance and potential utility of using different quantities of enzyme to tune sensor response characteristics, $CaCO_3$ microsphere loading efficiency was evaluated.

Both GOx and PdTCPP were encapsulated within $CaCO_3$ utilizing the coprecipitation technique described previously. Briefly, loaded $CaCO_3$ microspheres were prepared by adding 8 mL $CaCl_2$ (0.25 M) to 8 mL Na_2CO_3 (0.25 M) containing a variable amount of GOx (1-32 mg/mL), and/or 200 µL of 10 mM PdTCPP in DMSO. GOx concentrations beyond 32 mg/mL were considered impractical due to the quantity of enzyme required for their manufacture. After addition of the $CaCl_2$, the solution was stirred vigorously for 30 s, after which time the agitation was removed and the particles were allowed to mature under static conditions for 10 min. For particles to be used in PSS/PAH coatings, particles were then dropped into a 50mL beaker containing 16mL if 20 mg/mL PSS in 50 mM Tris pH 8.5 and allowed to stir for 10 minutes. The suspension was centrifuged and the supernatant was removed. The microspheres were then rinsed three times with the appropriate buffer prior to further processing.

GOx loading into $CaCO_3$ microspheres was evaluated by dissolving a known mass of dried particles in 0.1 M GDL in DI water and measuring the absorbance of the resulting solution at 370 nm. Similarly, loaded PdTCPP was quantified by measuring the absorbance of dissolved particle solutions at the 523 nm peak absorbance of the phosphor.

5.1.3 LbL fabrication and testing for glucose and oxygen-sensing MPACs

The electrostatic adsorption of polyelectrolyes on microspheres depends greatly on the surface charge of the substrate layer as well as the charge density of the polyelectrolyte. For example: a highly charged surface will attract more charge in the oppositely-charged free polyelectrolyte, leading to better adsorption of the free polyelectroyte of the surface. Three LbL pairs were employed to create layers of either high charge or layers of low permeability. PDADMAC and PSS are strong polyelectrolytes that easily adsorb to weakly charged surfaces, but do not form major diffusion barriers.[114, 134, 198, 199] Weak/strong polyelectrolyte pairs, such as PAH/ PSS-*co*-MA or PAH/PSS, form thicker, less permeable layers that can slow down small molecules such as glucose, but have much lower charge density than strong/strong pairs and tend to aggregate under low charge conditions.[105, 125, 163, 164] In this work, two different film architectures were evaluated. The first architecture tested was PSS/PAH, which was chosen due to the high degree characterization of such films, and its low glucose permeability.[113, 114, 128, 147, 181, 200] The second film, which consisted of 5 bilayers of PDADMAC/PSS and additional PAH/PSS-*co*-MA layers, provides high charge density initially which results in better charge reversal, and then utilizes the weak/strong

polyelectrolytes to provide a diffusion barrier. In addition, PAH/PSS-*co*-MA has the potential to be crosslinked, which could further decrease permeability.[201] However, this particular combination of polyelectrolytes has never before been tested.

The difference in permeability of the different layers is the central factor in not only the gelation of the MPAC matrix, but the flux-based sensor response. As such, evaluation of the glucose diffusion through these films is crucial to understanding the tunability of GOx-based MPAC sensors. $CaCO_3$ particles used in sensing MPACs were coated in two different LbL architectures described below.

5.1.3.1 PSS/PAH particles

After preparation and initial washing, a single batch of GOx and PdTCPP-loaded $CaCO_3$ microspheres (all particles from 1 coprecipitation) was dropped into 15 mL of stirring 20 mg/mL PAH in 50 mM Tris buffer (pH 8.5) in a 50 mL beaker with a triangular stir bar (25 mm). Particles were allowed to stir for 10 minutes, and then collected in a 50 mL tube, washed 3 times in 50 mM Tris buffer (pH 8.5) and resuspended in 15 mL 50 mM Tris buffer (pH 8.5). The particles were then added to 15 mL of 20 mg/mL PSS and stirred for 10 minutes similar to PAH. This process was repeated until the desired number of layers was deposited. Charge reversal at each layer was determined by zeta potential analysis.

5.1.3.2 PDADMAC/PSS + PAH/PSS-*co*-MA

One batch of particles at a time (all particles from 1 coprecipitation (either GOx + PdTCPP or PdTCPP only) was mixed with 1 mL of 20 mg/mL PDADMAC in 5 mM Na_2CO_3 pH 8.0 in a microcentrifuge tube. Stability of the initial charged layer was

evaluated after washing and over time. Once acceptably-stable conditions were determined, alternating strong polyelectrolytes (1 mL 20 mg/mL PDADMAC/PSS in 5 mM $NaHCO_3$, pH 8.0, mixed for 0.5 minutes) were deposited and evaluated for surface charge by monitoring surface charge after each additional layer. After the number of bilayers required to cause stabilization of surface charge was determined, the strong/weak polyelectrolyte combination, PSS-*co*-MA/PAH was deposited in increasing numbers from 5-25 bilayers and evaluated for charge reversal by zeta potential measurements. The PSS-*co*-MA/PAH layers were deposited in the following fashion: 1 mL (20 mg/mL PAH in 5 mM $NaHCO_3$ pH 8.0) was added to the particles and mixed for 0.5 minutes. The particles were then centrifuged down at 500 g and washed once with 1mL 5mM $NaHCO_3$ pH 7.2. After removal of the wash solution by centrifugation at 500g, 1 mL (20mg/mL PSS-*co*-MA in 5mM $NaHCO_3$ pH 7.2) was added to the particles, mixed for 0.5 minutes, and washed with 5mM $NaHCO_3$ pH 8.0 in a similar fashion. This process was repeated until the desired number of layers was achieved.

5.1.3.3 Layer-by-layer diffusion analysis

Diffusion of glucose through the polyelectrolyte multilayers was evaluated to determine the permeability of the layers to glucose. Polyelectrolyte multilayers were deposited by planar LbL technique in which polyelectrolytes are deposited on a porous, planar surface in alternating fashion. Varying numbers of polyelectrolyte multilayers were deposited on porous alumina disks (Anodisc 25, 60 μm thick, 0.02 μm pore diameter) under the same conditions as used for $CaCO_3$ particles of each LbL architecture. The LbL-coated disks were placed in PermeGear Side-bi-Side diffusion

cells. Disks were placed between feed reservoirs containing 100 mg/dL glucose and permeate reservoirs with buffer only. Samples were kept at room temperature and under constant stirring. Aliquots of solution were taken from both feed and permeate reservoirs at designated intervals of time and analyzed for glucose content using a YSI 2700 Biochemistry Analyzer. Change in concentration over time (dC/dt) of the permeate side was analyzed for films of different architectures (PDADMAC/PSS + PAH/PSS-*co*-MA and PAH/PSS) and number of polyelectrolyte bilayers (0-30 BL).

5.1.4 Oxygen-sensing MPAC

Oxygen-sensitivity of MPAC gel formulations has implications for the material's use *in vivo* oxygen sensing. Additionally, the performance of glucose-sensing MPACs will be dependent on the behavior of the oxygen-sensitive phosphors contained within. As MPAC-based oxygen or glucose sensors have never before been tested, their oxygen-dependent behavior was evaluated. Oxygen-sensing MPAC gels were evaluated for oxygen sensitivity using a custom flow-through and time-domain lifetime analysis system.

5.1.4.1 Sensor formulations

$CaCO_3$ particles used for oxygen-sensing MPAC contained only PdTCPP (no GOx). These PdTCPP-loaded $CaCO_3$ microspheres were coated with PDADMAC/PSS + PAH/PSS-*co*-MA nanofilm architecture. MPAC gels were fabricated with a 3x concentration of $CaCO_3$ microspheres of different numbers of bilayers (5, 10, 15, 20, 25, 30). Gels were cast between glass slides with 0.06" Teflon spacers. Biopsy punches

(2.5 mm) of samples were taken from the larger slab and were tested for oxygen sensitivity using a custom flow-through system (Figure 43).

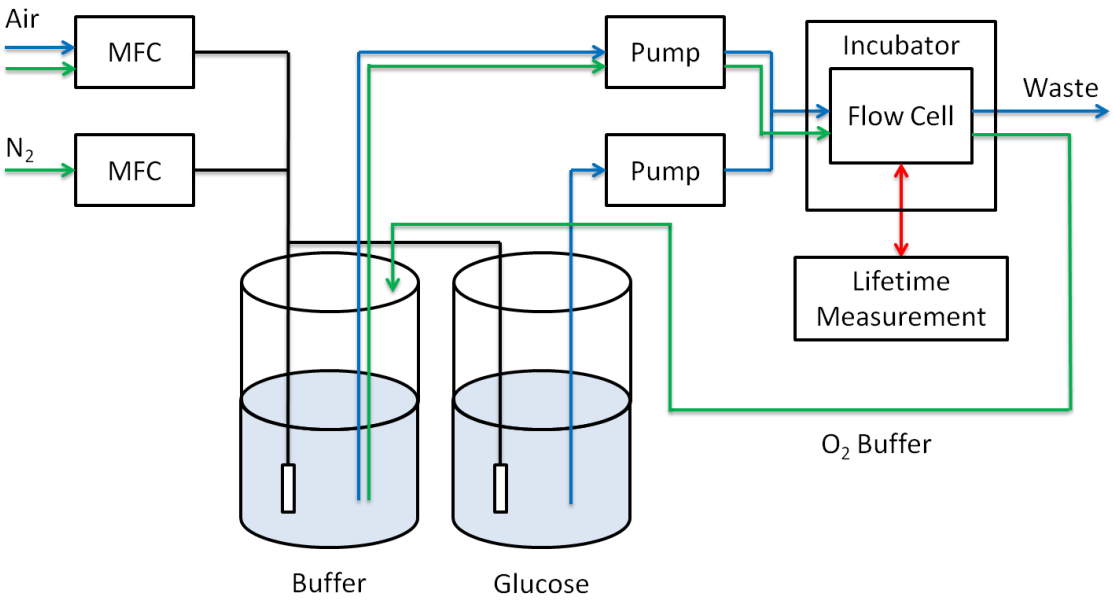

Figure 43: Schematic of the flow-through system utilized for glucose and oxygen-sensing MPAC sensors. Buffer flow during oxygen experiments (recirculating flow) is represented by green arrows. Buffer/analyte flow during glucose experiments is represented in blue.

5.1.4.2 Data collection and analysis

Sensor punches were placed in a custom flow-through cell three at a time (Figure 44). Buffer solution (10mM Tris pH 7.4) was flowed over the surface of the sensors and recirculated from a reservoir. Solution oxygen was controlled by bubbling a mixture of oxygen and nitrogen gases within the buffer reservoir. Oxygen/nitrogen mix ratios were controlled *via* mass flow controllers and solution oxygen concentration was monitored with an oxygen electrode (Unisense Ox500) to confirm changes in dissolved oxygen

within the reservoir. For 0% oxygen, a solution of extreme excess GOx (1 mg/mL) and glucose (30% wt/wt) in buffer was placed in the flow-cell and allowed to react until oxygen was eliminated from the system. Sensors within the flow cell were interrogated from below *via* a fiber bundle attached to a custom time-domain lifetime system (Figure 44).

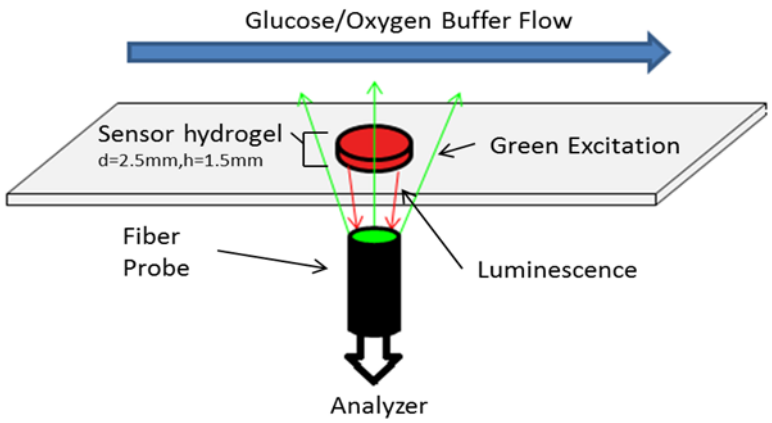

Figure 44: Schematic of the flow cell. Buffer containing varying levels of glucose or oxygen is flowed over the surface of the sensor, which is interrogated from below by a fiber bundle. [170] **© 2011 IEEE**

At each oxygen concentration, ~100 data points from each sensor in the flow cell were collected and averaged to determine the oxygen/lifetime relationship of that sensor. Oxygen concentrations were calculated by utilizing the partial pressure of the oxygen at a particular gas, assuming saturation from bubbling, and correcting this value for salinity and temperature using an oxygen solubility table provided by Unisense (salinity =1.3, temperature = 37C). Inverted measured lifetime values were plotted against oxygen

concentration in the form of equation (5.1). Each plotted sensor response was then fit linearly using a least-squares regression forced through a y-intercept of 1 in MatLab to determine its Stern-Volmer constant (K_{SV}). K_{SV} for a particular sample type was produced from an average of K_{SV} values from different samples of the same type.

5.1.5 Glucose-sensing MPAC

Glucose-sensing MPACs were fabricated from $CaCO_3$ particles loaded with GOx and PdTCPP. As glucose-sensing MPACs have never before been evaluated, the most important tunable parameters, particle concentration and bilayer number (representing permeability), were varied and evaluated for sensor response characteristics.

5.1.5.1 Sensor formulations

Two separate nanofilm architectures were used in the fabrication of glucose-sensing MPACs: PAH/PSS (described in 5.1.3.2) and PDADMAC/PSS + PAH/PSS (described in 5.1.3.3). In all glucose-sensing MPACs, $CaCO_3$ particles utilized were coprecipitated with 8 mg/mL GOx and 200 µL 10 mM PdTCPP in DMSO (refer to loading section).

For PAH/PSS architecture, MPAC gels were fabricated with varying concentrations of $CaCO_3$ microspheres (1, 2, 3, 4, 5x) of different numbers of bilayers (5, 10, 15, 20, 25, 30). Gels were cast between glass slides with 0.06" Teflon spacers. Biopsy punches (2.5 mm) of samples were taken from the larger slab and were tested for glucose sensitivity using a custom flow-through system (Figure 43). For PDADMAC/PSS + PAH/PSS architecture, 2x and 3x MPAC gels were evaluated from 10-30 BL.

5.1.5.2 *In vitro* testing apparatus and instrumentation

Individual MPAC samples were immobilized in a custom flow-through cell (Figure 44). An air-equilibrated buffer solution (10 mM Tris pH 7.4) containing different concentrations of glucose within the physiologic range (40-400mg/dL) was flowed over the surface of the sensor. Sensor sample phosphorescence was captured from below *via* a fiber optic bundle connected to a custom time-domain lifetime system (as in oxygen-sensing MPACs).

5.1.5.3 Data collection and analysis

Sensor lifetime values were recorded *via* a custom LabView program in a continuous fashion, resulting in a "stair step" response (Figure 45, top). Mean values at steady state lifetimes at each glucose concentration were used to create response curves (Figure 45, bottom).

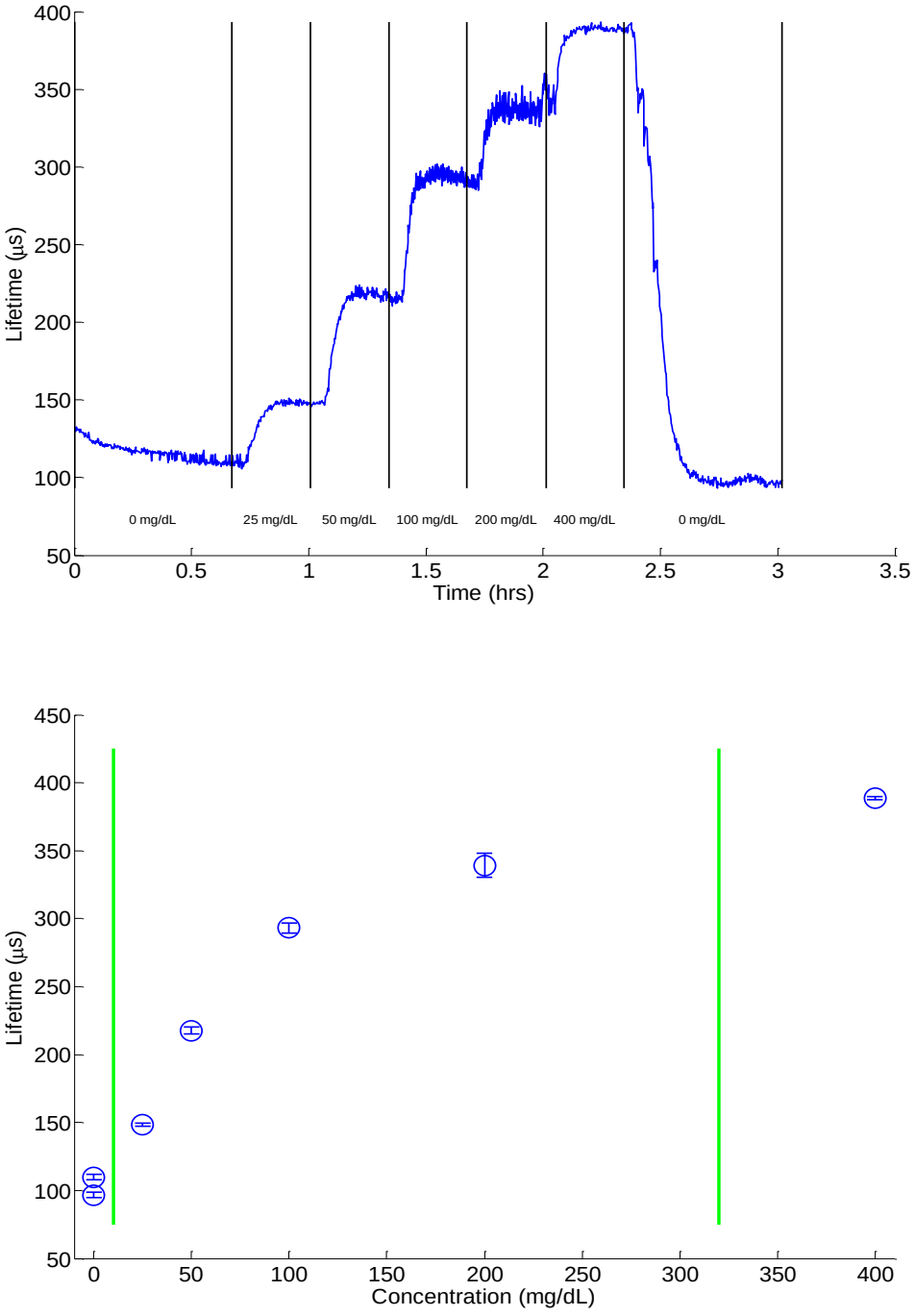

Figure 45: Top: Sample "stair-step" raw response data. Bottom: Resulting glucose response curve calculated from the average raw data steady-state values at each concentration. Increasing levels of glucose cause increased lifetime of the phosphor.

Important figures of merit calculated for each sensor formulation were limit of detection (LOD), representing the lowest detectable glucose concentration, analytical range, representing the glucose concentrations that can be accurately determined from sensor lifetime values given the variability of sensor signals, and sensitivity, representing the change in signal level over the analytical range. LOD was defined as the glucose concentration at which the corresponding lifetime value is three standard deviations above the measured baseline lifetimes (variability at 0 mg/dL glucose). The maximum differentiable glucose value (MDGV, at the top of the analytical range) was similarly defined as the glucose concentration at which the corresponding lifetime value is three standard deviations of the maximum measured lifetimes below the fitted maximum lifetime. Analytical range was defined as the difference between the MDGV and the LOD. Sensitivity was determined by taking the percent difference between fitted lifetime values at MDGV and LOD and dividing this value by the analytical range. Lastly, response time was calculated by utilizing the first transition in concentration (0 to 25 mg/dL glucose). This initial transition was chosen as a means to compare different samples as the calculation of response time is inaccurate when samples begin to saturate (there is little or no change in lifetime between concentrations) and this transition is before the saturation point in all samples. The transition is determined to begin when the measured lifetime value exceeds three times the standard deviation of the baseline and ends when the lifetime value approaches three standard deviations of the next concentration's mean lifetime value. The time of the transition from start to end points is given as the initial response time.

5.2 Results and discussion

5.2.1 GOx and PdTCPP loading

Utilizing the GOx-specific absorbance at 370 nm and the PdTCPP-specific absorbance at 523 nm, the loading of each was determined. In all particles containing PdTCPP, the same 200 µL 10 mM solution in DMSO was used as this amount resulted in sufficient phosphorescence intensity. PdTCPP loading efficiency into $CaCO_3$ particles was found to be 27 ± 9%, which corresponds to estimated concentration within a particle of 70 ±30 µM and an estimated mass dye /mass particle ratio of $1.1 \pm 0.5 \times 10^{-3}$. GOx-loaded particles showed a concentration-dependent loading (Figure 46). As GOx concentrations in the coprecipitation solution increased, loading quantity increased in a linear fashion over the concentrations tested. It is important to note that the morphology of particles changed dramatically from lower concentrations of GOx to higher concentrations of GOx (Figure 46). Particles became significantly smaller and less uniform as more GOx was used in their manufacture. A concentration of 8 mg/mL GOx was chosen for subsequent glucose-sensing MPAC testing due to the lack of morphological uniformity and impractical quantities of enzyme required beyond that concentration.

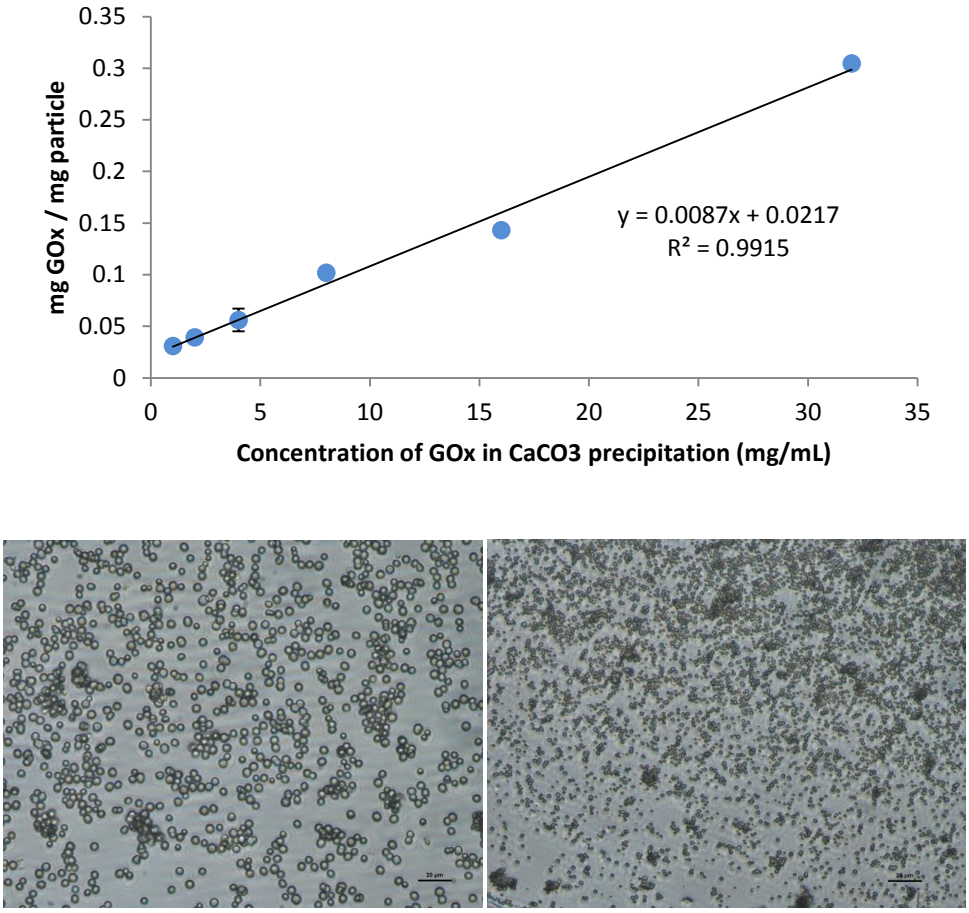

Figure 46: Top: Ratio of weight of GOx loaded per total weight of loaded $CaCO_3$ microspheres. Bottom: Morphological differences in $CaCO_3$ spheres with low levels of GOx (4 mg/mL GOx, left) and at high levels (32 mg/mL GOx, right). Error bars represent 95% confidence intervals (n=3).

5.2.2 LbL stability and permeability

5.2.2.1 LbL deposition on $CaCO_3$

Layer-by-layer on $CaCO_3$ particles containing GOx and PdTCPP resulted in charge reversal for both LbL architectures (Figure 47). However, in the case where strong polyelectrolytes were not utilized from the start, full charge reversal did not occur until about 5 bilayers. While this may seem to indicate that layers are not forming, this

is actually the result of measuring the zeta potential in excess of several hours after deposition. It was observed that there is a time-dependent loss of charge at lower polyelectrolyte numbers (Figure 48). This effect has been observed by others in the case of nanoparticle $CaCO_3$ coated in alginate polyelectrolyte.[202] Addition of polyelectrolyte to the coprecipitation solution has been shown to increase stability of the particles,[135] but utilizing polyelectrolyte in the coprecipitation results in extremely low protein loading. This is an important observation for the construction of polyelectrolyte multilayers on $CaCO_3$ microspheres not utilizing a polyelectrolyte in the coprecipitation solution. Additional polyelectrolyte layers must be deposited within a reasonable time of the deposition of the previous layer. Therefore, depositions applied in this work were conducted in rapid succession. Specifically, after assembly of a single layer, washes were completed and subsequent layers were deposited within 5 minutes of one another. Particles with below 5 bilayers of material were never left in polyelectrolyte-free solutions for extended periods of time. In addition to deposition times, zeta potential measurements of these layers must be made quickly in order to ensure an accurate surface charge measurement. This is especially important when comparing layers of different materials with different charge density, as these layers could display differences in zeta potential simply as a result of when they were measured.

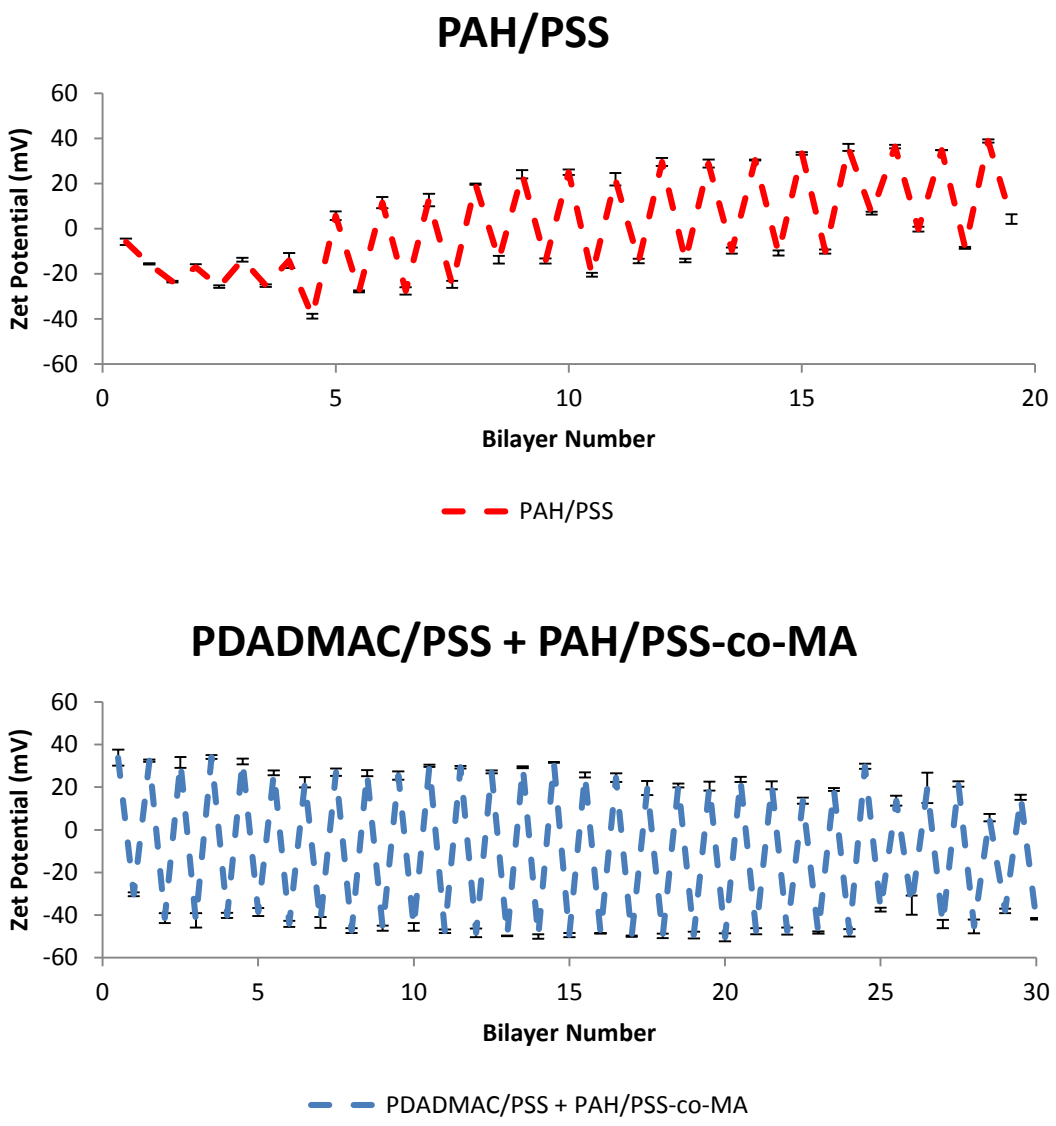

Figure 47: Top: Zeta potential of loaded $CaCO_3$ particles coated in PAH/PSS nanofilm architecture as a function of bilayer number. Bottom: Zeta potential of loaded $CaCO_3$ particles coated in PDADMAC/PSS + PAH/PSS-*co*-MA nanofilm architecture. Error bars represent 95% confidence intervals (n=3)

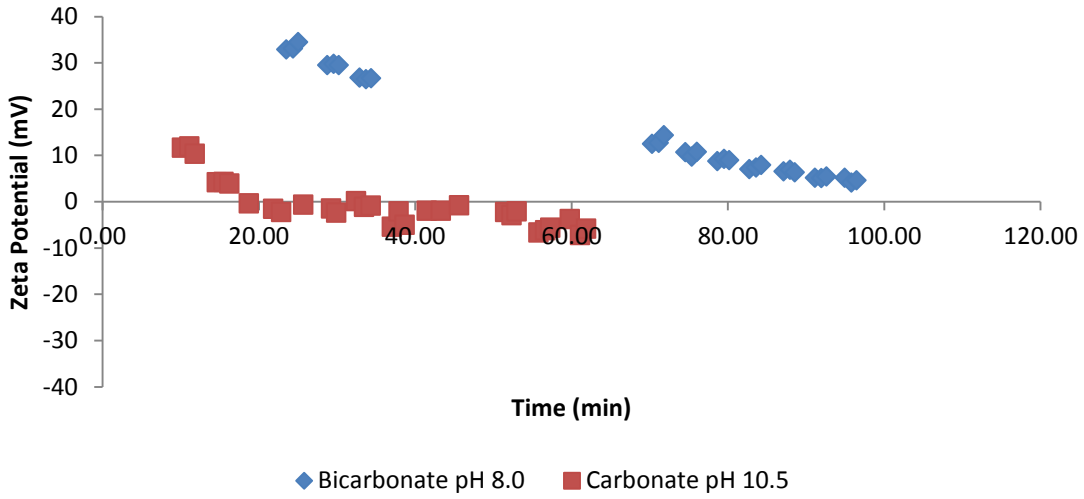

Figure 48: Stability of a single layer of PDADMAC on loaded $CaCO_3$ particles as a function of time since deposition and buffer type.

5.2.2.2 LbL permeability

Glucose permeabilities of the two nanofilm architectures utilized in glucose-sensing MPAC hydrogels were evaluated using PEMs deposited on planar porous substrates. Films were prepared with identical deposition conditions used to create capsules in an effort to closely match the film architecture and porosity. Average rates of change in concentration (dC/dt) of the permeate reservoirs were calculated by finding the slope of glucose concentration over time and averaged between three independent samples. Figure 49 shows the dC/dt values for both films and the bare substrate. The data indicate that, as expected, the strong/strong polyelectrolytes PDADMAC/PSS slow diffusion of glucose minimally.[115] Strong/weak polyelectrolyte pairs on the other hand (PAH/PSS and PAH/PSS-co-MA) slow glucose diffusion in a much more dramatic way. This is consistent to what has been reported on planar substrates, and results from

differences in thickness and porosity.[203] Layers of PAH/PSS deposited under the described conditions cause a drastic change in permeability with only the first 5 bilayers. Subsequent layers showed decreased permeability, but at a decreasing rate. Overall, PAH/PSS films were significantly less permeable than PDADMAC/PSS + PAH/PSS-*co*-MA films of similar numbers of layers. This difference could be due to two different factors: 1) the deposition pH of PAH, which has been shown to affect the thickness of layers of weak polyelectrolytes,[199] or 2) the use of PSS versus PSS-*co*-MA. While the differences in film properties due to deposition pH is a known relationship, structural differences in layers of PSS versus PSS-co-MA deposited in various conditions have not been fully characterized. Therefore, it is indeterminate how these two factors together may cause the observed differences. These observations are significant, as choosing the appropriate film architecture and therefore permeability is particularly important for flux-based microparticle glucose sensors, which have been shown to have drastically different response characteristics based upon film diffusion properties.[133]

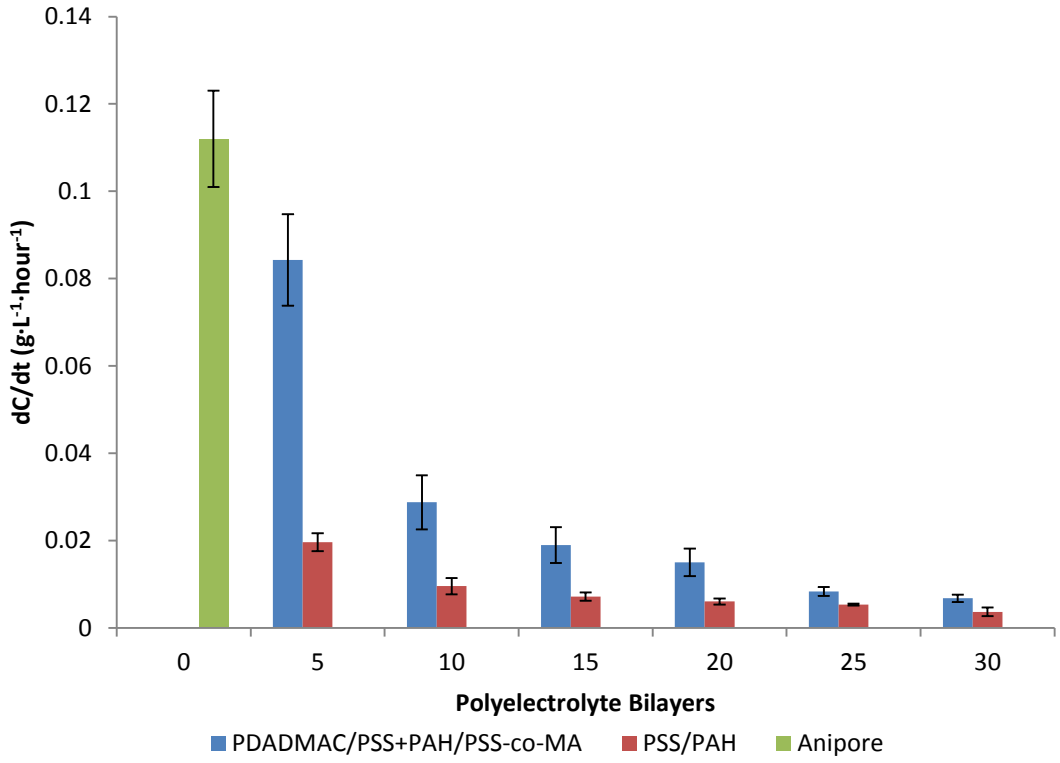

Figure 49: Change in concentration of glucose on the permeate side of the diffusion apparatus as a function of numbers of polyelectrolyte bilayers and architecture type. Error bars represent 95% confidence intervals (n=3).

5.2.3 Oxygen-sensitive MPACs

Oxygen-dependence of MPACs fabricated with different numbers of polyelectrolyte multilayers of the PDADMAC/PSS + PAH/PSS-*co*-MA architecture will be dependent on the Stern-Volmer relationship of the encapsulated phosphor and specifically, the empirically-determined Stern-Volmer constant K_{SV}. As mentioned earlier, this value is based upon inherent properties of the dye, diffusional properties of the matrix, as well as some other physical phenomena associated with the dye-quencher

interaction.[166] In the case of MPAC hydrogels, phosphor and oxygen are expected to be freely mobile within the polyelectrolyte pores (as nanoparticles were shown to be free moving),[7] and so polyelectrolyte multilayers were not expected to cause major differences in quenching behavior.

Oxygen-sensitive MPAC gels with different numbers of polyelectrolyte bilayers displayed a characteristic dependence on oxygen concentration. As oxygen concentration decreases, lifetime of the phosphor contained within the micropores of the MPAC increases with increasing sensitivity (Figure 50). When transformed into the relation $\frac{\tau_0}{\tau}$ the values exhibit a non-linear dependence on oxygen (Figure 51). This behavior has been observed for PdTCPP in certain polymer matrices and a two-site Stern-Volmer relationship better approximates the dye's interaction with oxygen in this case.[204]

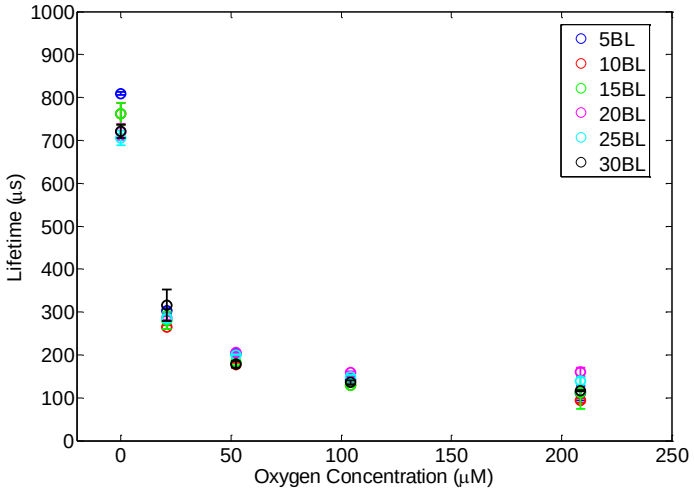

Figure 50: Average lifetime values of oxygen-sensitive 3x MPAC gels with varying numbers of polyelectrolyte bilayers. Error bars indicate standard deviations (n=3).

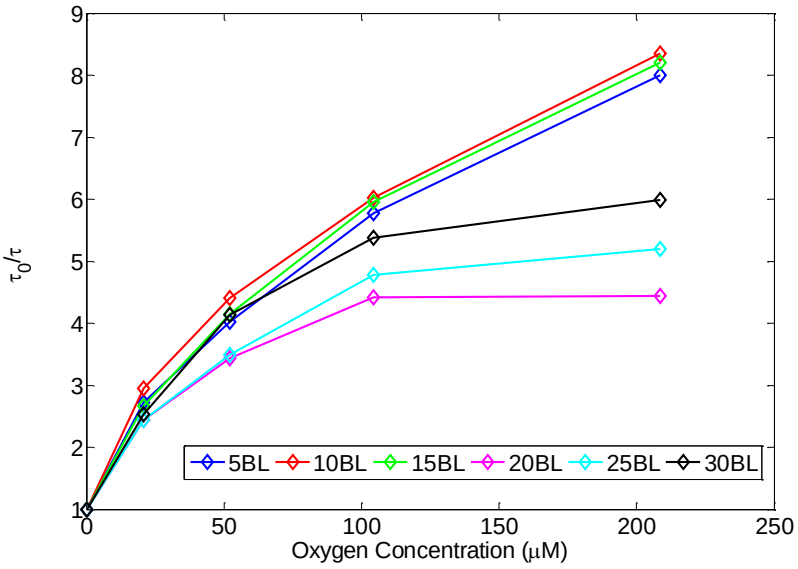

Figure 51: τ_0/τ relationship of 3x MPAC gels fabricated with different numbers of polyelectrolyte bilayers.

In this situation, the simple linear (one-site) Stern-Volmer model does not describe the quenching behavior of the dye. Instead, a multi-site equation is a better fit. Two-site Stern-Volmer relations have three components, the two Stern-Volmer constants representing the two different dye-quencher interactions (K_{SV1}, K_{SV2}) and the fraction of dye molecules in the first state (f). This relationship is given in the form:

$$\frac{\tau_0}{\tau} = \left[\frac{f}{1+K_{sv1}\cdot[O_2]} + \frac{1-f}{1+K_{sv2}\cdot[O_2]}\right]^{-1} \quad (5.4)$$

Fitting the MPAC oxygen sensing data to this equation using NLLS gives the parameters in Table 2.

Table 2: Two site Stern-Volmer parameters for oxygen-sensitive MPAC gels of different numbers of polyelectrolyte bilayers. Values are averages of different samples with 95% confidence (n=3).

Bilayer Number	K_{SV1} (μM^{-1}) (n=3, α=0.05)	K_{SV2} (μM^{-1}) (n=3, α=0.05)	*f* (n=3, α=0.05)
5	0.12 ± 0.0087	$1.41 \pm 1.55 \times 10^{-3}$	0.87 ± 0.018
10	0.15 ± 0.019	$3.12 \pm 1.37 \times 10^{-3}$	0.84 ± 0.015
15	0.13 ± 0.038	$2.42 \pm 1.33 \times 10^{-3}$	0.86 ± 0.046
20	0.15 ± 0.025	$6.81 \pm 1.24 \times 10^{-14}$	0.81 ± 0.013
25	0.12 ± 0.015	$9.40 \pm 1.34 \times 10^{-14}$	0.84 ± 0.018
30	0.11 ± 0.019	$2.31 \pm 0.098 \times 10^{-14}$	0.88 ± 0.011

Though are some significant differences between sample types, namely the K_{SV1} of 30BL samples and the *f* value of 20 BL samples are lower than all other samples and the *f* value of 30 BL is slightly lower than 10BL. Overall, K_{SV1} and *f* values for different MPAC types do not follow a strong trend and do not differ greatly in magnitude. However, K_{SV2} values do significantly differ with MPAC gels made with 20 bilayers or more. The orders of magnitude difference in K_{SV1} and K_{SV2} in these samples corresponds to the marked nonlinearity observed (Figure 51). This difference in site interaction causes these sensors to be much less sensitive to oxygen at higher

concentrations, while having relatively similar sensitivity at lower oxygen concentrations. The most likely cause for this effect is the presence of a population of unquenchable phosphor, which continues to emit at higher oxygen concentrations. This population is likely precipitated dye within the capsules, as the phosphors have limited solubility in water. However, according to the data, the population fraction of the precipitated dye (f) is very similar for all samples. This means that the accessibility of the dye, represented by K_{SV2}, is primary cause for this difference. This major difference could be due to organization of the dye precipitates, such as size, surface area or other complexation effects. The precipitation of dye, and hence the precipitate size and morphology, could be affected by the speed of dissolution of the $CaCO_3$ templates or the pH of the solution during dissolution, both of which are dependent on bilayer numbers. Regardless of the mechanism, having this unquenched population results in a lower overall sensitivity of the MPAC sensors for the entire range of oxygen concentrations. However, it does increase the relative baseline lifetime and intensity, which could be advantageous for *in vivo* measurement where any increase in signal intensity would be beneficial. Additionally, the most relevant oxygen concentrations for *in vivo* oxygen sensing lie below 100 µM, where all MPAC sensors have very high sensitivity.

5.2.4 Glucose-sensing MPAC

Glucose-sensing MPACs were fabricated with particles containing the enzyme GOx and the oxygen sensitive porphyrin PdTCPP. Sensors fabricated with two different nanofilm architectures (PAH/PSS and PDADMAC/PSS + PAH/PSS-*co*-MA), different microsphere concentrations (1x-5x) representing gel porosity and overall enzyme

concentration, and numbers of polyelectrolyte bilayers (5-30BL) representing different permeabilities were evaluated for sensor response by exposing punches of each material to glucose in the physiologic range (40-400 mg/dL) and monitoring the phosphorescence lifetime of the dye within the MPACs. Representative raw data from these experiments are given in Figure 45 (above). Glucose-sensing MPAC hydrogels were expected to have response characteristics that are dependent on bilayer number while not being dependent on porosity. With greater diffusion barrier to glucose, it was expected that sensitivities would decrease and analytical ranges to increase, as this relationship has been previously explored in systems consisting of polyelectrolyte-coated microspheres, which resemble the pores in the MPAC.[133]

MPAC gels constructed with PAH/PSS nanofilm architectures showed a glucose response dependence on both concentrations of microspheres as well as numbers of polyelectrolyte bilayers utilized in fabrication. There was a clear trend for MPACs fabricated with increasing concentrations of particles towards higher sensitivity and lower analytical range (Figure 52). The observed differences in responses represent the classic inverse relationship between sensitivity and analytical range in flux-based sensors, and can be seen quantitatively in Table 3. For maximum utility *in vivo*, the analytical range of glucose sensors must extend from low glucose < 40 mg/dL to up to 400 mg/dL, although the most important analysis region is the hypoglycemic region. Gels with the highest concentrations of particles saturated at near 50 mg/dL glucose and had an over 600% total change in lifetime while gels fabricated with the lowest concentration of particles had a nearly undetectable change in response over the range of

glucose concentrations. Gels with 2x and 3x particle concentrations maintain high sensitivity (~0.5% per mg/dL glucose) while having reasonable analytical ranges (~240 mg/dL glucose). In addition, gels of different concentrations displayed some small differences in initial response times. Gels with larger concentrations of particles had slightly longer initial response times, indicating a possible difference in bulk transport in the hydrogel. This effect would likely be due to the increase in calcium utilized in these gels, as higher crosslinker concentrations result in changes in mechanical properties as evidenced in Section 4. These changes could influence the transport through the alginate itself. It is important to note as well that in the calculation of response time, increases in variability in steady state lifetime measurements could cause decreases in calculated response times in these samples. Even so, in all cases, gels had response times lower than ten minutes, which is on the order of the delay in time between changes in blood and interstitial glucose *in vivo*, and so would allow for the accurate determination of changes in glucose.[205, 206]

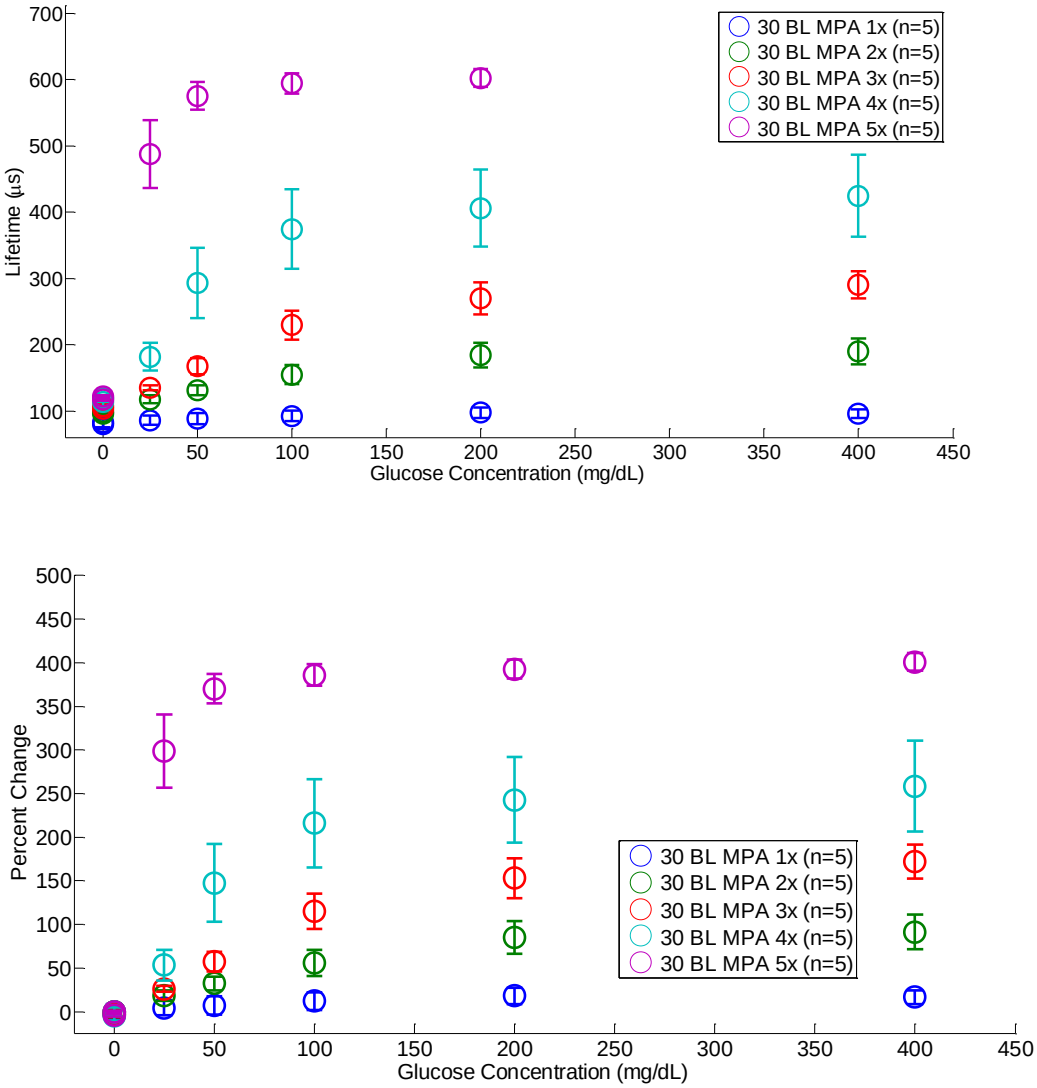

Figure 52: Response curves of 30BL MPAC gels made with different concentrations of particles (1-5x). Top: Lifetime versus glucose concentration. Bottom: Percent change versus glucose concentration. Error bars indicate standard deviations (n=5).

Table 3: Sensor figures of merit for MPAC sensors fabricated with different concentrations of $CaCO_3$ microspheres. Values represent averages of individual sensor responses with 95% confidence (n=5). *Values that could not be accurately calculated based on the formula utilized.

Concentration (30BL)	*Enzyme Concentration (mg/mL MPAC)*	*Sensitivity (% per mg/dL glucose)*	*LOD (mg/dL glucose)*	*Analytical Range (mg/dL glucose)*	*Initial Response Times (min)*
1	$0.4 \pm 0.4 \times 10^{-2}$	0.3 ± 0.04	34.2 ± 13.7	34.2 – 85.7 (51.5)	*
2	$0.9 \pm 0.7 \times 10^{-2}$	0.4 ± 0.10	6.1 ± 1.6	6.1 – 237.8 (231.7)	5.0 ± 1.8
3	$1.3 \pm 1.1 \times 10^{-2}$	0.8 ± 0.2	4.4 ± 1.8	4.4 – 246.1 (241.6)	6.5 ± 1.5
4	$1.7 \pm 1.5 \times 10^{-2}$	2.3 ± 0.7	1.9 ± 0.3	1.9 – 111.0 (109.1)	8.7 ± 1.1
5	$2.2 \pm 1.8 \times 10^{-2}$	7.2 ± 2.4	0.2 ± 0.03	0.2 – 64.3 (64.2)	8.1 ± 0.3

In an ideal case, where oxygen and glucose are supplied equally to identical individual pores, the pores will behave *independently*, and oxygen levels within the pores should not be affected by total porosity.[207] However, if pores are close enough to cause depletion of oxygen near surrounding pores, the pores will behave in a *cooperative manner*, where pores begin to affect each other's responses. In this case, the sensor

response of the entire matrix will be affected.[207] This seems to be the case in MPACs made with higher particle concentrations, where oxygen depletion (measured by luminescence lifetime) is much higher. In lower particle concentrations, increasing availability of oxygen as a result of higher oxygen concentrations around the pores lowers the observed lifetimes while extending the range of the sensors. This means that increasing quantities of glucose are required to deplete the larger quantities of oxygen available. Additionally, once the concentration of particles is low (1x), there is not enough enzyme present (Table 3) to significantly deplete oxygen within the pores, despite having large quantities of glucose. This results in the observed lowering of maximum response as particle (and hence enzyme) concentration decreases.[208] From these observations, we can conclude two things: 1) pores interact with one another in a cooperative manner (at least at high concentrations) and 2) the concentrations of GOx in combination with the number of bilayers utilized in this study do not provide an appropriate reaction/diffusion balance to allow for depletion of oxygen at low pore concentrations.

Based upon the favorable figures of merit of MPAC gels fabricated at a particle concentration of 3x, this concentration was chosen to hold constant for comparing MPAC sensor glucose response as a function of bilayer numbers (Figure 53).

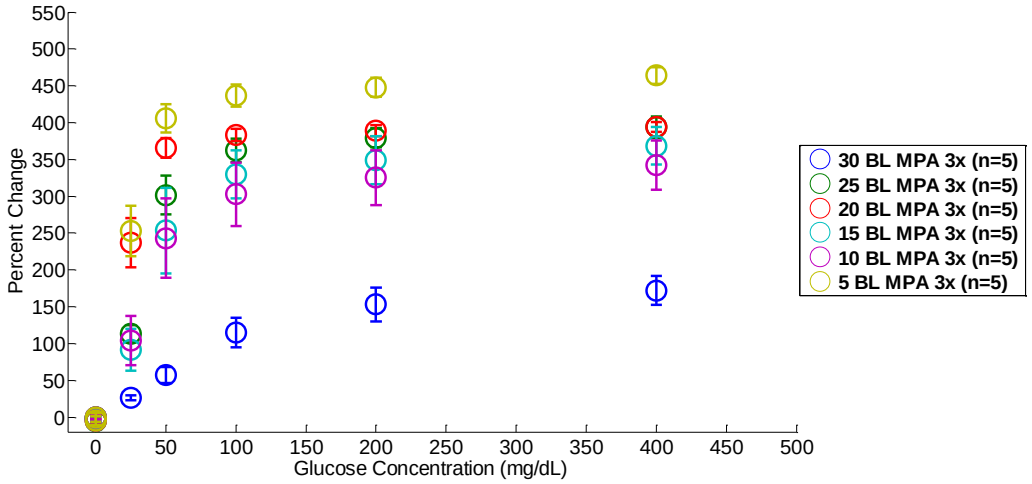

Figure 53: Response curves of 3x MPAC gels made with different numbers of polyelectrolyte bilayers. Values are given as percent change versus glucose concentration. Error bars represent standard deviations (n=5).

At 3x concentration of particles, glucose-sensing MPAC gels displayed a significant dependence on numbers of bilayers for all figures of merit except for initial response times. The initial response times of MPAC samples fabricated with different bilayer numbers showed no apparent trend, and all remained at or below ~10 minutes. Gels fabricated with lower numbers of layers generally exhibited higher sensitivity and lower analytical ranges (Table 4). This behavior resembles a similar effect seen with previous microsphere-based sensors developed in our lab.[133]

Table 4: Sensor figures of merit for MPAC sensors fabricated with different numbers of polyelectrolyte bilayers. Values represent averages of individual sensor responses with 95% confidence (n=5).

Bilayer Number (3x)	*Sensitivity (% per mg/dL glucose)*	*LOD (mg/dL glucose)*	*Analytical Range (mg/dL glucose)*	*Initial Response Time (min)*
5	6.5 ± 0.5	0.6 ± 0.2	0.6 – 65.1 (64.5)	8.5 ± 1.4
10	3.8 ± 0.9	1.6 ± 0.3	1.6 – 85.0 (83.4)	9.7 ± 1.0
15	3.9 ± 0.5	2.6 ± 0.6	2.6 – 87.5 (84.9)	8.2 ± 0.7
20	6.6 ± 0.8	0.4 ± 0.2	0.4 – 58.4 (58.0)	9.7 ± 0.7
25	4.8 ± 1.0	1.5 ± 0.2	1.5 – 78.7 (77.2)	10.3 ± 0.5
30	0.8 ± 0.2	4.4 ± 1.8	4.4 – 246.1 (241.6)	6.5 ± 1.5

When comparing diffusion of glucose through planar LbL with the sensitivities and ranges obtained from sensors fabricated with this LbL architecture (Figure 54), a clear relationship between diffusion behavior and response characteristics is evident (Figure 54). Generally, as glucose flux through the nanofilm increases, sensitivity increases and analytical range decreases. This follows a similar trend as what was observed with organo-silicate and alginate microspheres in the past,[133] and would seem to indicate that increasing film diffusion barriers are lowering the ratio of glucose and

oxygen flux (J_G/J_O), resulting in depletion of oxygen to occur over a wider range of glucose. However, based upon data collected from MPACs fabricated with different concentrations of particles we must also consider differences in cooperative effects, such as the distance between particles, the degree of oxygen depletion between particles, and the relative diffusion of glucose and oxygen through the alginate matrix. Based upon the data gathered, it can be concluded that there is indeed a relationship between nanofilm layer number (*i.e.* permeability) and sensitivity and range. Unfortunately, due to the presence of cooperative effects, comparisons to nanofilm-sensor response dependencies in the previously described one dimensional models of organo-silicate and alginate microspheres[209] are not appropriate based on the complexity of the MPAC system.

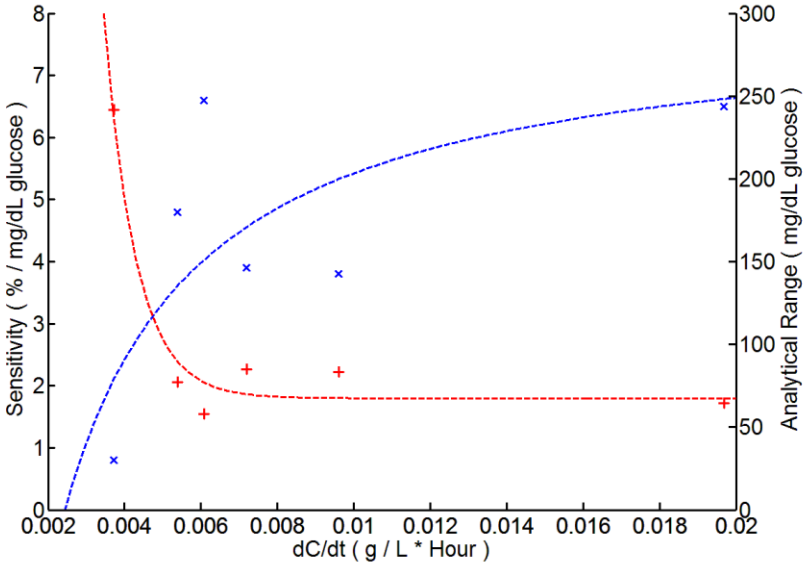

Figure 54: Sensitivity (x, blue) and analytical range (+, red) plotted against dC/dt values based upon numbers of polyelectrolyte bilayers. Fits are shown in dotted lines for sensitivity (blue) and analytical range (red).

Based upon favorable response parameters found using 2x and 3x PAH/PSS nanofilm architecture, PDADMAC/PSS + PAH/PSS-*co*-MA-based MPAC gels with varying numbers of bilayers (0-30BL) were fabricated and tested at 2x and 3x concentrations. At the 2x concentration, response characteristics of the MPAC gels had similar trends to the materials made with PAH/PSS, with decreasing sensitivity and increasing linearity with increasing numbers of bilayers (Figure 55). However, analytical ranges for high numbers of bilayers were impossible to determine, as the signal change from 0 to 400 mg/dL glucose was within baseline error (Table 5). In addition, this baseline variability prevented the accurate calculation of initial response times for these samples. With 3x concentration of particles, no clear trend in sensitivity based upon bilayer number was determined. However, analytical range trending was consistent for these samples. Overall, MPAC samples with this nanofilm architecture did not seem to be as dependent on bilayer numbers as in the case of PAH/PSS architecture, and did not have response characteristics proportional to measured difference in dC/dt.

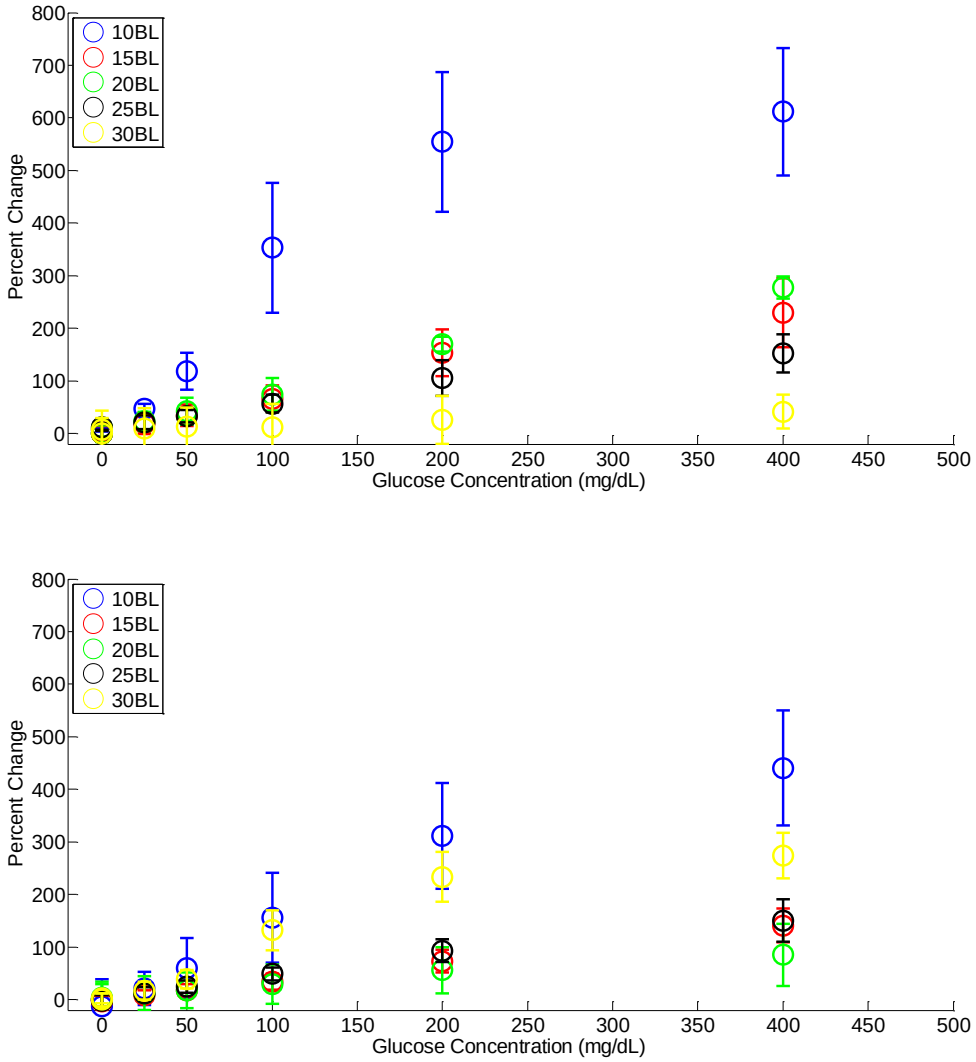

Figure 55: Response curves of 2x (top) and 3x (bottom) MPAC gels made with different numbers of polyelectrolyte bilayers. Values are given as percent change versus glucose concentration. Error bars represent standard deviations (n=3).

Table 5: Sensor figures of merit for MPAC sensors fabricated with different numbers of polyelectrolyte bilayers. Values represent averages of individual sensor responses with 95% confidence (n=5). [a]Sensors fabricated at 2x concentration. [b]Sensors fabricated at 3x concentration. *Values that could not be accurately calculated based on the formula utilized.

Bilayer Number	*Sensitivity (%)*	*LOD (mg/dL glucose)*	*Analytical Range (mg/dL glucose)*	*Initial Response Time (min)*
10	2.6 ± 0.9^{a}	9.3 ± 1.0^{a}	$9.3 - 221^{a}$ (211)	2.8 ± 1.0^{a}
	0.9 ± 0.3^{b}	8.1 ± 3.5^{b}	$8.1 - 474$ $(465)^{b}$	3.0 ± 1.5^{b}
15	0.5 ± 0.2^{a}	23.4 ± 8.3^{a}	$23.4 - 371$ $(348)^{a}$	*
	0.2 ± 0.1^{b}	26.5 ± 6.9^{b}	$26.5 - 3.4 \times 10^{3}$ $(3.3 \times 10^{3})^{b}$	*
20	0.6 ± 0.4^{a}	24.6 ± 7.6^{a}	$24.6 - 510$ $(485)^{a}$	*
	0.2 ± 0.1^{b}	35.1 ± 18.0^{b}	$24.6 - 724$ $(689)^{b}$	*
25	0.3 ± 0.1^{a}	13.7 ± 3.7^{a}	$13.7 - 477$ $(464)^{a}$	*
	0.3 ± 0.1^{b}	10.2 ± 3.3^{b}	$10.2 - 555$ $(545)^{b}$	2.1 ± 0.9^{b}
30	$0.1 \pm 1.2 \times 10^{-2}$ [a]	62.4 ± 3.7^{a}	*	*
	0.9 ± 0.2^{b}	6.1 ± 1.1^{b}	$6.1 - 271$ $(266)^{b}$	3.2 ± 0.9^{b}

Looking back at dC/dt values for both film architectures, we can see that the dC/dt values of PDADMAC/PSS + PAH/PSS-*co*-MA films were much higher than those

for PAH/PSS films. In fact, the lowest dC/dt value for PDADMAC/PSS + PAH/PSS-*co*-MA films was at 30BL, and this value was still greater than dC/dt of PAH/PSS films at 20BL. Looking at Figure 54, we see that the primary region of change in response characteristics for PAH/PSS lies below 0.004 g/L•hour. Even at 30BL, PDADMAC/PSS + PAH/PSS-*co*-MA-based films have significantly higher dC/dt than 0.004 g/L•hour. As a result, we would expect that PDADMAC/PSS + PAH/PSS-*co*-MA-based MPAC would have less dependence on the film dC/dt. Additionally, sensor response characteristics of MPACs fabricated with PDADMAC/PSS + PAH/PSS-*co*-MA displayed overall lower sensitivities than MPACs made with PAH/PSS for similar dC/dt. This seems to indicate the presence of another effect aside from diffusivity differences. Reduced sensitivity, which results from lower oxygen depletion within the sensor, could therefore plausibly be the result of increased distances between particles (swelling), or reduced enzyme activity. Due to the very small observed changes in swelling behaviors with bilayer numbers at high particle concentrations in Section 4, the reduction in sensitivity for a given dC/dt is more likely due to reduced enzyme activity. If enzyme is less active in the particles, then there would be less average active enzyme per volume of entire MPAC sensor. Due to the cooperative nature of the pores, this would manifest in a similar fashion to PAH/PSS-based MPAC gels fabricated with varying particle concentrations as seen in Figure 52; and in fact, this is what is observed. As the same $CaCO_3$ particle fabrication technique was utilized for both nanofilm architectures, it would be expected that enzyme activities would be similar at that stage.

Therefore, the most reasonable point for enzyme activity loss is during the LbL deposition.

5.3 Conclusions

The work in this section represents the foundation of the sensing application for MPAC hydrogels, with a specific focus on oxygen and glucose sensing. MPAC hydrogels were shown to function as matrices for holding oxygen and glucose sensing chemistry. Both phosphor and glucose oxidase can be encapsulated within $CaCO_3$ and can be retained within the pores, and interrogated externally using optical techniques. MPAC sensors responded to external changes in oxygen or glucose, and are highly dependent on fabrication parameters.

In the case of oxygen-sensitive MPACs, polyelectrolyte bilayers had a minor influence on sensor behavior causing increased non-linearity of the Stern-Volmer relationship, likely due to the precipitation of dye within the capsules during dissolution of the template. However, oxygen-sensitive MPAC gels all showed extremely high sensitivity to oxygen in the physiologically-relevant range (< 100 μM).

Glucose-sensing MPACs were demonstrated to have tunable sensitivity and range depending on the concentration of particles or the numbers of bilayers utilized in fabrication. However, dependence on particle concentration of MPAC gels indicates that the individual pores within the alginate matrix are interacting with each other in a *cooperative* way. If pores were truly independent reactors, the response profiles of MPACs made with different numbers of particles would have responses dependent on the polyelectrolyte multilayers only. This would make sensor response characteristics

variable for formulations in which mechanical stability is an issue (such as was observed in Section 3). This could explain the lack of clear trends in formulations utilizing PDADMAC/PSS + PAH/PSS-*co*-MA nanofilm architecture, as these films are more highly permeable. With increased diffusion barriers, the effect of cooperativity could theoretically be lowered and sensor response characteristics made more stable.

Regardless, glucose sensing MPACs were shown to be made with high sensitivity and analytical ranges within the physiologically-relevant glucose range. The response attributes of these sensing MPACs can be modulated using nanofilm permeability, though these sensors are still dependent upon cooperativity. As such, they could be susceptible to changes in effective pore concentration, which could change based upon swelling, for example. Future optimization of MPAC glucose sensors will rely not only on the knowledge of diffusional effects of the LbL nanofilms utilized, but on a more in depth understanding of the pore cooperativity, which influences the glucose and oxygen distributions within the bulk. This will require an analysis of average particle distances as well as diffusion/reaction behavior of glucose and oxygen in the bulk MPAC material within the gel utilizing both finite element modeling and *in vitro* study.

This initial work has produced formulations of MPAC sensors that will function within the desired ranges of oxygen and glucose for *in vivo* measurement. However, with the proper understanding of cooperative effects, glucose and oxygen sensing MPAC formulations could be better designed to account for, or utilize, these effects to produce optimized systems. In addition, other sensing chemistries, either flux-dependent

or independent, could similarly be incorporated into MPAC constructs for multianalyte and/or multimodal sensing applications.

6. CONCLUSIONS AND FUTURE WORK

6.1 Conclusions

This work demonstrates the fabrication, mechanical evaluation, and sensor response modulation of a novel injectable material, microporous alginate composite (MPAC). By adjusting input parameters, this system can be utilized to control the gelation rate of bulk alginate materials as well as encapsulate sensing and therapeutic agents for the monitoring and treatment of chronic disease. The properties of the composites were shown to be modulated by adjusting the porosity and numbers of polyelectrolyte bilayers used in their fabrication.

To determine the feasibility of the novel system as a *functional* injectable system, several important criteria were evaluated including the loading of model macromolecules, nanoparticles and catalytic components, retention of these components, and interaction of the catalytic components with the external environment. Utilizing the encapsulation properties of $CaCO_3$, fluorescently labeled-bovine serum albumin, various sizes of FluoSpheres (20, 100, 200 nm), and glucose oxidase were loaded into microspheres. Polyelectrolyte multilayers were deposited on the loaded-$CaCO_3$ microspheres to retain these molecules. MPAC hydrogels were fabricated using these loaded particles and the internal gelation technique utilizing glucono-δ-lactone. MPAC hydrogels fabricated in this fashion retained the functional elements within distinct pore structures, where encapsulated material could freely move and interact with externally-supplied substrates. The novel addition of polyelectrolyte multilayers to the internal

gelation of alginate matrix not only allowed for the retention of material, but also was observed to affect the gelation kinetics of the composite.

To better understand how MPAC gelation kinetics could be modulated and how these changes affect the composite after gelation, a series of experiments was performed in which MPAC fabrication parameters including the concentration of $CaCO_3$ particles and the numbers of polyelectrolyte bilayers utilized were varied. Gelation times, pH evolution, and mechanical properties of the material were evaluated for dependence on fabrication parameters. MPAC hydrogels were shown to have controllable gelation kinetics based upon particle concentration as well as numbers of bilayers, with larger numbers of layers and lower particle concentrations resulting in extended gelation times. pH changes within the composites were shown to remain within safe levels during gelation, and were similarly dependent on fabrication parameters. Utilizing easily tunable particle concentrations and polyelectrolyte multilayer architectures, future MPAC-based devices could be tailored to gel at a rate and strength suited for their application site, whether located in the subcutaneous, joint capsule, or epidural space. The mechanical stability of the hydrogels in DI water using dynamic mechanical analysis (DMA) gave insight into the physical changes happening within the hydrogel matrix as a function of fabrication parameters. Gels containing lower numbers of particles displayed the most swelling and the least stability of MPACs tested, while high concentrations of particles showed little or no change after solvent exposure. The polyelectrolyte materials utilized had minimal impact on the swelling/stability behavior

of MPACs except within highly unstable regions of the fabrication parameters (such as around 1x concentration and 10-20BL).

The DMA method, while utilized in the this work to determine general solvent stability of MPACs, is envisioned to be utilized further for assessing stability of MPAC gels under various destabilizing conditions such as in the presence of high concentrations of monovalent cations, as well as in the presence of protein and enzymes found in body fluid. These experiments will be of utmost importance in evaluating appropriate degradation profiles for *in vivo* experiments, and for potentially developing *designed* degradation profiles of the composite based upon the fabrication parameters and utilization of additional degradation strategies such as partial oxidation of alginate. In addition, incorporating degradable polyelectrolytes, such as chitosan, alginate, poly(L-lysine), or dextran sulfate could allow for the development of fully-degradable hydrogels.

In addition to showing modulation of gelation kinetics and material properties, it was shown that MPAC gels were able to function either as an oxygen or glucose-sensing material by incorporation of an oxygen-sensitive phosphor or the phosphor and glucose oxidase respectively. These two specific examples of sensor chemistry embody two different transduction mechanisms that can be utilized in a diverse set of dye and enzyme molecules. Thus, in principle, MPAC gels could be utilized to house other flux independent luminescent chemistries as well as flux/reaction dependent sensing chemistries relying on enzymes such as oxidoreductases. Of the two sensing chemistries studied, both displayed high sensitivity when incorporated within MPAC hydrogels.

Oxygen-sensitive MPAC gels were shown to be highly sensitive in the physiologically-relevant oxygen range (< 100μM), displaying great utility for tissue oxygen measurement. Glucose-sensitive MPACs displayed variable sensitivities and ranges depending on the concentration of particles utilized as well as the numbers of polyelectrolyte bilayers. Appropriate fabrication parameters were determined for high sensitivity within the physiologically relevant glucose range (40-400 mg/dL).

Due to the dependence of glucose-sensing MPACs on particle concentration, it was hypothesized that pores within the MPACs were behaving in a cooperative manner. Cooperativity has been recognized as a likely characteristic of microparticle and microdomain systems, but it has not been studied in depth in our laboratory. MPAC gels may offer a means to study this phenomenon. As MPAC gels provide a means to immobilize precise concentrations of particles with known enzyme concentrations, models comparing relative reaction rates, diffusion parameters and particle spacing could be directly compared to *in vitro* results. While highly academic in nature, the understanding of cooperative behaviors *in silico* and *in vitro* will enhance the development and testing of microparticle/microcapsule sensors, including flux-based MPAC sensors, and help future scientists design these sensors appropriately.

It is important to appreciate that the MPAC composite system has the potential to not only perform as an injectable single sensor system, but as a *multimodal* or *multifunctional* system. This is one area where MPAC hydrogels could make a significant impact in the advancement of implantable devices, providing multiple, tunable functionalities within a single construct. Future work will be focused on the

development of multiple capabilities of the composite beyond oxygen and glucose sensing. Some preliminary work has been completed to demonstrate the feasibility of MPAC-based multimodal sensors and controlled release systems. The following sections detail two examples of these: SERS-based sensing and drug delivery.

6.2 SERS-based sensing MPACs

Towards additional sensing applications, recent preliminary work has focused on implementing surface enhanced Raman spectroscopy (SERS) to serve as another sensing modality in addition to phosphorescence lifetime and intensity. The Raman-active dye 4-aminothiophenol (4-ATP) is capable of producing a change in its Raman spectrum as a result of pH change in the solution. This dye can be conjugated to gold nanoparticles to produce a SERS spectrum. Preliminary data have suggested that 4-ATP-modified gold nanoparticles can be encapsulated within $CaCO_3$, coated in polyelectrolytes, and made into an MPAC hydrogel, which can be examined using Raman spectroscopy (Appendix B.1, Figure 56). However, these results are limited to very concentrated MPAC samples, which have not been optimized. Strong SERS peaks for 4-ATP have been reported at 1587, 1078, and 391,[210] which correspond closely to peaks observed for nanoparticle-loaded MPACs (Figure 56, arrows). Additional work is required to confirm these results and optimization of the process will likely be required prior to testing of the pH sensing chemistry simultaneously with phosphorescence chemistry. This pH sensing chemistry could also be put to use in combination with glucose oxidase, which produces acid as a result of its reaction with glucose and oxygen (6.1-6.2), to create another type of glucose-sensitive chemistry.

$$\text{(6.1)}\quad \text{Glucose} + O_2 \xrightarrow{\text{GOx}} \text{Glucono-}\delta\text{-lactone} + H_2O_2$$

$$\text{(6.2)}\quad \text{Glucono-}\delta\text{-lactone} + H_2O \xleftrightarrow{k1([OH^-])} \text{Gluconate}^- + H^+ \text{ (hydrolysis)}$$

In a short span of time, oxygen, glucose and pH sensitive elements utilizing two different sensing modalities could be incorporated within an MPAC gel, creating a true multimodal sensor. In addition, other sensing systems based upon oxidoreductases such as lactate oxidase could be utilized in combination with glucose oxidase to produce a variety of different multianalyte/multimodal sensors.

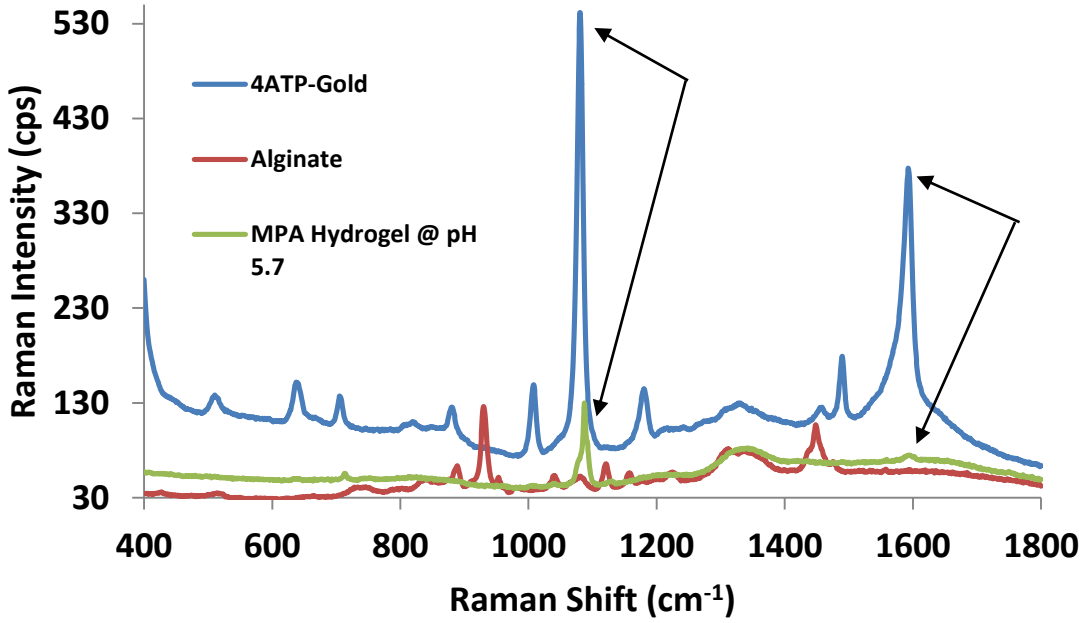

Figure 56: RAMAN spectra of 4ATP-modified gold nanoparticles (blue), alginate (red), and MPAC hydrogel containing 4-ATP-modified gold nanoparticles (green). Arrows point to 4-ATP and MPAC peaks that correspond to each other and to referenced 4-ATP peaks.

6.3 Drug delivery with MPACs

Another important application for MPAC gels is the storage and delivery of therapeutics for drug delivery applications. Future work in this area will involve the encapsulation of model therapeutics and the tuning of release profiles for both passive and stimulated release. Preliminary work (Appendix B.2) has shown some promising results in this direction. $CaCO_3$ microspheres have been shown to be capable of loading both rhodamine 101 (R101) and rhodamine B-labeled aminodextran (3k) (RBD) representing a model small molecule (R101) and peptide (RBD) respectively. MPACs fabricated with these loaded particles have shown to release the materials (Figure 57).

When utilizing highly permeable layer-by-layer consisting of PDADMAC/PSS only (Figure 57, top), release of RBD showed no diffusion inhibition due to polyelectrolytes. In the case of less permeable layers (PDADMAC/PSS + PAH/PSS-*co*-MA as in Section 5), release of R101 showed release only in 0-10 bilayers of polyelectrolyte (Figure 57, bottom) and retained loaded material above 10 bilayers (not shown). This phenomenon may have more to do with the solubility of the dye rather than its transport through the nanofilms. If dye were to precipitate after or during the dissolution of $CaCO_3$, then the release of dye would be greatly inhibited due to a large proportion of the dye being in a larger form factor. In the case of RBD, the molecule is extremely hydrophilic, and so that molecule is unlikely to precipitate. While additional studies need to be performed to confirm these hypotheses, these data do indicate the potential of MPAC gels to encapsulate and release therapeutic materials. However, a great deal of extra work will need to go into exploring the effects of coprecipitation on

specific dye/drug molecules as well as the optimization of nanofilms to create the appropriate diffusion barriers.

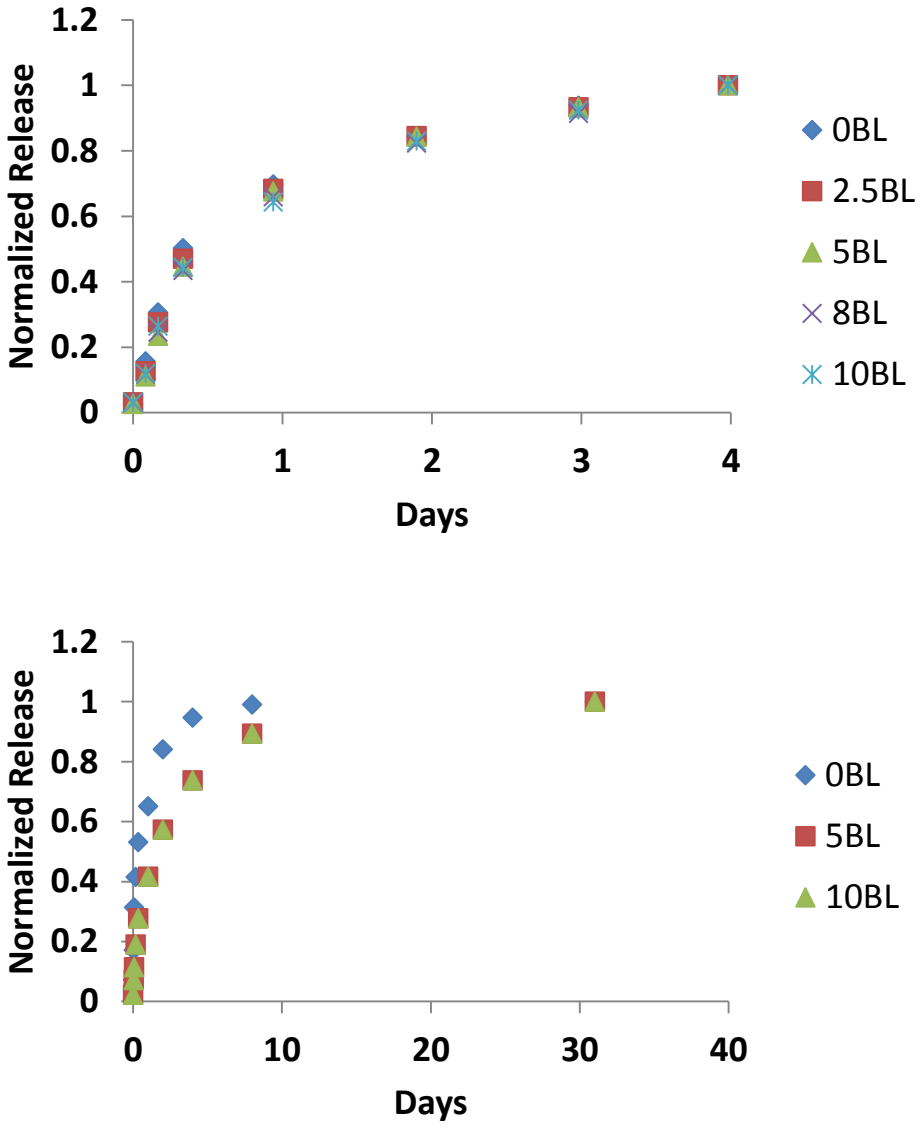

Figure 57: Preliminary release kinetics of rhodamine B-labeled aminodextran (top) and rhodamine 101 (bottom) from alginate matrices with varying numbers of polyelectrolyte bilayers. LbL used in aminodextran release was of PDADMAC/PSS architecture, while rhodamine 101 release utilized PDADMAC/PSS + PAH/PSS-*co*-MA architecture.

The last and arguably the most important future direction of MPAC development is the *in vivo* evaluation of MPAC gels. While it is likely that MPAC hydrogels will have favorable host response (alginate materials have generally been shown to be biocompatible), gelation kinetics, mechanical stability, and host reaction to the alginate matrix will need to be determined if MPAC hydrogels are going to be utilized in whole or as part of future biomedical devices. The first set of *in vivo* experiments will need to focus on the determination of gelation properties *in vivo*, degradation of implants over time, as well as the host response to the implants.

With many different potential applications, study of the MPAC material could branch out into many different areas; the previously discussed areas represent only a few of them. The work presented here confirms the tunable nature of MPAC hydrogel functionality, which gives the material advantages as a platform for different multianalyte/multimodal sensing applications. This work represents the beginning of this material's development and demonstrates its potential as a tool to improve monitoring and treatment of chronic conditions.

REFERENCES

1. P. Remington, R. C. Brownson and M. V. Wegner, *Chronic Disease Epidemiology and Control*, American Public Health Association, Washington D.C., 2010.
2. G. Anderson and J. Horvath, *Public Health Rep.*, 2004, **119**, 263-270.
3. D. J. Kuruvilla and A. K. Salem, in *Nanotechnology and Nanomedicine in Diabetes*, Science Publishers, Enfield, NH, 2012.
4. L. H. Reddy and P. Couvreur, *Journal of Hepatology*, 2011, **55**, 1461-1466.
5. D. Brambilla, B. Le Droumaguet, J. Nicolas, S. H. Hashemi, L.-P. Wu, S. M. Moghimi, P. Couvreur and K. Andrieux, *Nanomed. Nanotechnol. Biol. Med.*, 2011, **7**, 521-540.
6. N. Vij and A. Gorde, in *Pulmonary Nanomedicine: Diagnostics, Imaging, and Therapeutics*, Pan Stanford Publishing, Singapore, 2012.
7. J. R. Roberts, D. W. Ritter and M. J. McShane, *Journal of Materials Chemistry B*, 2013, **1**, 3195-3201.
8. O. Wichterle and D. Lim, *Nature*, 1960, **185**, 117-118.
9. S. R. Van Tomme, G. Storm and W. E. Hennink, *Int. J. Pharm.*, 2008, **355**, 1-18.
10. N. A. Peppas, P. Bures, W. Leobandung and H. Ichikawa, *European Journal of Pharmaceutics and Biopharmaceutics*, 2000, **50**, 27-46.
11. J. D. Kretlow, L. Klouda and A. G. Mikos, *Adv. Drug Del. Rev.*, 2007, **59**, 263-273.

12. C. B. Packhaeuser, J. Schnieders, C. G. Oster and T. Kissel, *European Journal of Pharmaceutics and Biopharmaceutics*, 2004, **58**, 445-455.

13. A. Hatefi and B. Amsden, *J. Controlled Release*, 2002, **80**, 9-28.

14. S. J. Bidarra, C. C. Barrias and P. L. Granja, *Acta Biomater.*, **10**, 1646-1662.

15. B. D. Ratner and H. A.S., in *Hydrogels for Medical and Related Applications*, American Chemical Society, Washington, D.C., 1976, 1-36.

16. K. Y. Lee and D. J. Mooney, *Chem. Rev.*, 2001, **101**, 1869-1880.

17. B. D. Ratner and S. J. Bryant, *Annu. Rev. Biomed. Eng.*, 2004, **6**, 41-75.

18. M. Patenaude, N. M. B. Smeets and T. Hoare, *Macromol. Rapid Commun.*, 2014, **35**, 598-617.

19. B. D. Mather, K. Viswanathan, K. M. Miller and T. E. Long, *Prog. Polym. Sci.*, 2006, **31**, 487-531.

20. S.-C. Han, W.-D. He, J. Li, L.-Y. Li, X.-L. Sun, B.-Y. Zhang and T.-T. Pan, *J. Polym. Sci., Part A: Polym. Chem.*, 2009, **47**, 4074-4082.

21. Y. Liang, T. W. Jensen, E. J. Roy, C. Cha, R. J. DeVolder, R. E. Kohman, B. Z. Zhang, K. B. Textor, L. A. Rund, L. B. Schook, Y. W. Tong and H. Kong, *Biomaterials*, 2011, **32**, 2004-2012.

22. Y. Lei, S. Gojgini, J. Lam and T. Segura, *Biomaterials*, 2011, **32**, 39-47.

23. C. D. Pritchard, T. M. O'Shea, D. J. Siegwart, E. Calo, D. G. Anderson, F. M. Reynolds, J. A. Thomas, J. R. Slotkin, E. J. Woodard and R. Langer, *Biomaterials*, 2011, **32**, 587-597.

24. S. Q. Liu, C. Yang, Y. Huang, X. Ding, Y. Li, W. M. Fan, J. L. Hedrick and Y.-Y. Yang, *Adv. Mater.*, 2012, **24**, 6484-6489.

25. Y. Yu, C. Deng, F. Meng, Q. Shi, J. Feijen and Z. Zhong, *Journal of Biomedical Materials Research Part A*, 2011, **99A**, 316-326.

26. M. V. Tsurkan, K. Chwalek, S. Prokoph, A. Zieris, K. R. Levental, U. Freudenberg and C. Werner, *Adv. Mater.*, 2013, **25**, 2606-2610.

27. B. Qiu, S. Stefanos, J. Ma, A. Lalloo, B. A. Perry, M. J. Leibowitz, P. J. Sinko and S. Stein, *Biomaterials*, 2003, **24**, 11-18.

28. S.-Y. Choh, D. Cross and C. Wang, *Biomacromolecules*, 2011, **12**, 1126-1136.

29. H. Zhang, A. Qadeer and W. Chen, *Biomacromolecules*, 2011, **12**, 1428-1437.

30. R. Zhang, Z. Huang, M. Xue, J. Yang and T. Tan, *Carbohydr. Polym.*, 2011, **85**, 717-725.

31. T. Ito, Y. Yeo, C. B. Highley, E. Bellas and D. S. Kohane, *Biomaterials*, 2007, **28**, 3418-3426.

32. Y. Luo, J. B. Kobler, J. T. Heaton, X. Jia, S. M. Zeitels and R. Langer, *Journal of Biomedical Materials Research Part B: Applied Biomaterials*, 2010, **93B**, 386-393.

33. C. A. DeForest, B. D. Polizzotti and K. S. Anseth, *Nat Mater*, 2009, **8**, 659-664.

34. V. Crescenzi, L. Cornelio, C. Di Meo, S. Nardecchia and R. Lamanna, *Biomacromolecules*, 2007, **8**, 1844-1850.

35. G. Testa, C. Di Meo, S. Nardecchia, D. Capitani, L. Mannina, R. Lamanna, A. Barbetta and M. Dentini, *Int. J. Pharm.*, 2009, **378**, 86-92.

36. R. Jin, C. Hiemstra, Z. Zhong and J. Feijen, *Biomaterials*, 2007, **28**, 2791-2800.

37. S. D. Fitzpatrick, M. A. Jafar Mazumder, F. Lasowski, L. E. Fitzpatrick and H. Sheardown, *Biomacromolecules*, 2010, **11**, 2261-2267.

38. J. H. Cho, S.-H. Kim, K. D. Park, M. C. Jung, W. I. Yang, S. W. Han, J. Y. Noh and J. W. Lee, *Biomaterials*, 2004, **25**, 5743-5751.

39. H. S. Choi, K. Yamamoto, T. Ooya and N. Yui, *ChemPhysChem*, 2005, **6**, 1081-1086.

40. S. E. Stabenfeldt, A. J. García and M. C. LaPlaca, *Journal of Biomedical Materials Research Part A*, 2006, **77A**, 718-725.

41. J. Berger, M. Reist, J. M. Mayer, O. Felt and R. Gurny, *European Journal of Pharmaceutics and Biopharmaceutics*, 2004, **57**, 35-52.

42. S. R. Van Tomme, B. G. De Geest, K. Braeckmans, S. C. De Smedt, F. Siepmann, J. Siepmann, C. F. van Nostrum and W. E. Hennink, *J. Controlled Release*, 2005, **110**, 67-78.

43. S. R. Van Tomme, M. J. van Steenbergen, S. C. De Smedt, C. F. van Nostrum and W. E. Hennink, *Biomaterials*, 2005, **26**, 2129-2135.

44. S. R. Van Tomme, A. Mens, C. F. van Nostrum and W. E. Hennink, *Biomacromolecules*, 2007, **9**, 158-165.

45. L. Yu, G. T. Chang, H. Zhang and J. D. Ding, *Int. J. Pharm.*, 2008, **348**, 95-106.

46. J. Berger, M. Reist, J. M. Mayer, O. Felt, N. A. Peppas and R. Gurny, *European Journal of Pharmaceutics and Biopharmaceutics*, 2004, **57**, 19-34.

47. M. G. Peter, *Journal of Macromolecular Science, Part A*, 1995, **32**, 629-640.

48. K. Y. Lee and D. J. Mooney, *Prog. Polym. Sci.*, 2012, **37**, 106-126.

49. T. Andersen, J. E. Melvik, O. Gåserød, E. Alsberg and B. E. Christensen, *Biomacromolecules*, 2012, **13**, 3703-3710.

50. A. D. Augst, H. J. Kong and D. J. Mooney, *Macromol. Biosci.*, 2006, **6**, 623-633.

51. S. K. Bajpai and S. Sharma, *React. Funct. Polym.*, 2004, **59**, 129-140.

52. Y. Cheng, X. Luo, C.-Y. Tsao, H.-C. Wu, J. Betz, G. F. Payne, W. E. Bentley and G. W. Rubloff, *Lab on a Chip*, 2011, **11**, 2316-2318.

53. A. L. Ching, C. V. Liew, P. W. S. Heng and L. W. Chan, *Int. J. Pharm.*, 2008, **355**, 259-268.

54. P. de Vos, C. G. van Hoogmoed, J. van Zanten, S. Netter, J. H. Strubbe and H. J. Busscher, *Biomaterials*, 2003, **24**, 305-312.

55. I. Donati and S. Paoletti, in *Alginates: Biology and Applications*, ed. B. H. A. Rehm, Springer, Berlin, 2009, 1-53.

56. K. Draget, K. Østgaard and O. Smidsrød, *Appl. Microbiol. Biotechnol.*, 1989, **31**, 79-83.

57. K. I. Draget, G. Skjåk Bræk and O. Smidsrød, *Carbohydr. Polym.*, 1994, **25**, 31-38.

58. K. I. Draget and C. Taylor, *Food Hydrocolloid*, 2011, **25**, 251-256.

59. J. L. Drury and D. J. Mooney, *Biomaterials*, 2003, **24**, 4337-4351.

60. C. D. Elizabeth, E. R. Nancy, L. R. Terry and L. P. Marian, *J. Cell. Physiol.*, 1992, **152**, 422-429.

61. K. B. Fonseca, S. J. Bidarra, M. J. Oliveira, P. L. Granja and C. C. Barrias, *Acta Biomater.*, in press.

62. W. R. Gombotz and S. Wee, *Adv. Drug Del. Rev.*, 1998, **31**, 267-285.

63. Y. Hori, A. M. Winans and D. J. Irvine, *Acta Biomater.*, 2009, **5**, 969-982.

64. S. M. Jay and W. M. Saltzman, *J. Controlled Release*, 2009, **134**, 26.

65. S. M. Jay, B. R. Shepherd, J. W. Andrejecsk, T. R. Kyriakides, J. S. Pober and W. M. Saltzman, *Biomaterials*, in press.

66. G. Klöck, A. Pfeffermann, C. Ryser, P. Gröhn, B. Kuttler, H.-J. Hahn and U. Zimmermann, *Biomaterials*, 1997, **18**, 707-713.

67. C. K. Kuo and P. X. Ma, in *Biomaterials for Drug Delivery and Tissue Engineering*, eds. S. Mallapragada, M. Tracy, B. Narasimhan, E. Mathiowitz and R. Korsmeyer, Cambridge University Press, New York, NY, 2001, pp. LL1.5.1-LL1.5.6.

68. C. K. Kuo and P. X. Ma, *Biomaterials*, 2001, **22**, 511-521.

69. K. Y. Lee, J. A. Rowley, P. Eiselt, E. M. Moy, K. H. Bouhadir and D. J. Mooney, *Macromolecules*, 2000, **33**, 4291-4294.

70. Y. Li, J. Rodrigues and H. Tomas, *Chem. Soc. Rev.*, 2012, **41**, 2193-2221.

71. A. Martinsen, G. Skjåk-Bræk and O. Smidsrød, *Biotechnol. Bioeng.*, 1989, **33**, 79-89.

72. A. Martinsen, I. Storro and G. Skjak-Braek, *Biotechnol. Bioeng.*, 1992, **39**, 186-194.

73. E. A. Nunamaker, K. J. Otto and D. R. Kipke, *Journal of the Mechanical Behavior of Biomedical Materials*, 2011, **4**, 16-33.

74. E. A. Nunamaker, E. K. Purcell and D. R. Kipke, *Journal of Biomedical Materials Research Part A*, 2007, **83A**, 1128-1137.

75. Z. Qinhua, L. Jianbo, H. An, Z. Dagen, X. Shasha, L. Quan, H. Yuexin, S. Yunfeng, H. Liumin and X. Wei, *Biomedical Materials*, 2012, **7**, 035012.

76. J. A. Rowley, G. Madlambayan and D. J. Mooney, *Biomaterials*, 1999, **20**, 45-53.

77. G. Skjåk-Bræk, E. Murano and S. Paoletti, *Biotechnol. Bioeng.*, 1989, **33**, 90-94.

78. O. Smidsrød and G. Skja˚k-Br┤k, *Trends Biotechnol.*, 1990, **8**, 71-78.

79. T. Andersen, J. E. Melvik, O. Gåserød, E. Alsberg and B. E. Christensen, *Carbohydr. Polym.*, 2014, **99**, 249-256.

80. C. A. McKay, R. D. Pomrenke, J. S. McLane, N. J. Schaub, E. K. DeSimone, L. A. Ligon and R. J. Gilbert, *ACS Appl. Mater. Interfaces*, 2014, **6**, 1424-1438.

81. M. Audebrand, M. Kolb and M. A. V. Axelos, *Biomacromolecules*, 2006, **7**, 2811-2817.

82. A.-L. Kjøniksen, M. Hiorth, J. Roots and B. Nyström, *The Journal of Physical Chemistry B*, 2003, **107**, 6324-6328.

83. E. Murano, *J. Appl. Ichthyol.*, 1998, **14**, 245-249.

84. S. K. Motwani, S. Chopra, S. Talegaonkar, K. Kohli, F. J. Ahmad and R. K. Khar, *European Journal of Pharmaceutics and Biopharmaceutics*, 2008, **68**, 513-525.

85. P.-L. Tremblay, F. Berthod, L. Germain and F. A. Auger, *J. Pharmacol. Exp. Ther.*, 2005, **315**, 510-516.

86. B. P. Chan, C. H. Li, K. L. Au-Yeung, K. Y. Sze and A. H. W. Ngan, *Ann. Biomed. Eng.*, 2008, **36**, 1254-1267.

87. D. W. Hutmacher, *Journal of Biomaterials Science, Polymer Edition*, 2001, **12**, 107-124.

88. J. M. McPherson, *Clinical Materials*, 1992, **9**, 225.

89. R. G. Willaert and G. V. Baron, *Rev. Chem. Eng.*, 1996, **12**, 160-205.

90. S. Sugiura, T. Oda, Y. Izumida, Y. Aoyagi, M. Satake, A. Ochiai, N. Ohkohchi and M. Nakajima, *Biomaterials*, 2005, **26**, 3327.

91. S. K. Tam, J. Dusseault, S. Bilodeau, G. Langlois, J.-P. Hallé and L. H. Yahia, *Journal of Biomedical Materials Research Part A*, 2011, **98A**, 40-52.

92. M. Menard, J. Dusseault, G. Langlois, W. E. Baille, S. K. Tam, L. Yahia, X. X. Zhu and J. P. Halle, *J. Biomed. Mater. Res. Part B*, 2010, **93B**, 333-340.

93. A. Haug and B. Larsen, *Acta Chem. Scand.*, 1962, **16**, 1908-1918.

94. A. Haug, B. Larsen and O. Smidsrød, *Acta Chem. Scand.*, 1967, **21**, 691-704.

95. B. Kloareg and R. Quatrano, *Oceanogr. Mar. Biol. Annu. Rev.*, **26**, 259-315.

96. O. Smidsrod, *Faraday Discuss. Chem. Soc.*, 1974, **57**, 263-274.

97. A. L. Haug and O. Smisrod, *Acta Chem. Scand.*, 1965, **19**, 341-351.

98. G. T. Grant, E. R. Morris, D. A. Rees, P. J. C. Smith and D. Thom, *FEBS Lett.*, 1973, **32**, 195-198.

99. W. Burchard and S. Ross-Murphy, in *Physical Networks: Polymers and Gels*, Elsevier Applied Science, New York, NY, 1990, 283-301.

100. B. T. Stokke, O. Smidsrød, F. Zanetti, W. Strand and G. Skjåk-Bræk, *Carbohydr. Polym.*, 1993, **21**, 39-46.

101. U. Remminghorst and B. Rehm, *Biotechnol. Lett*, 2006, **28**, 1701-1712.

102. P. X. Ma, in *Scaffolding in Tissue Engineering*, eds. P. X. Ma and J. Elisseeff, CRC Press, Boca Raton, FL, 2006, 13-26.

103. J. Sun and H. Tan, *Materials*, 2013, **6**, 1285-1309.

104. G. Orive, A. M. Carcaboso, R. M. Hernández, A. R. Gascón and J. L. Pedraz, *Biomacromolecules*, 2005, **6**, 927-931.

105. G. Skjåk-Bræk, H. Grasdalen and O. Smidsrød, *Carbohydr. Polym.*, 1989, **10**, 31-54.

106. M. Rajaonarivony, C. Vauthier, G. Couarraze, F. Puisieux and P. Couvreur, *J. Pharm. Sci.*, 1993, **82**, 912-917.

107. D. Poncelet, B. Poncelet De Smet, C. Beaulieu, M. L. Huguet, A. Fournier and R. J. Neufeld, *Appl. Microbiol. Biotechnol.*, 1995, **43**, 644-650.

108. P. Eiselt, J. Yeh, R. K. Latvala, L. D. Shea and D. J. Mooney, *Biomaterials*, 2000, **21**, 1921-1927.

109. L. S. C. Wan, P. W. S. Heng and L. W. Chan, *J. Microencapsulation*, 1992, **9**, 309-316.

110. G. Fundueanu, C. Nastruzzi, A. Carpov, J. Desbrieres and M. Rinaudo, *Biomaterials*, 1999, **20**, 1427-1435.

111. A. A. Antipov, G. B. Sukhorukov, S. Leporatti, I. L. Radtchenko, E. Donath and H. Mohwald, *Colloid Surf. A-Physicochem. Eng. Asp.*, 2002, **198**, 535-541.

112. A. A. Antipov and G. B. Sukhorukov, *Adv. Colloid Interface Sci.*, 2004, **111**, 49-61.

113. J. Park and M. J. McShane, *ACS Appl. Mater. Interfaces*, 2010, **2**, 991-997.

114. X. Liu and M. L. Bruening, *Chem. Mater.*, 2003, **16**, 351-357.

115. M. D. Miller and M. L. Bruening, *Langmuir*, 2004, **20**, 11545-11551.

116. R. Heuberger, G. Sukhorukov, J. Vörös, M. Textor and H. Möhwald, *Adv. Funct. Mater.*, 2005, **15**, 357-366.

117. G. Decher, *Science*, 1997, **277**, 1232-1237.

118. C. Schüler and F. Caruso, *Macromol. Rapid Commun.*, 2000, **21**, 750-753.

119. X. Zhang, K. K. Sharma, M. Boeglin, J. Ogier, D. Mainard, J.-C. Voegel, Y. Mély and N. Benkirane-Jessel, *Nano Lett.*, 2008, **8**, 2432-2436.

120. D. Volodkin, Y. Arntz, P. Schaaf, H. Moehwald, J.-C. Voegel and V. Ball, *Soft Matter*, 2008, **4**, 122-130.

121. A. R. Battle, S. M. Valenzuela, A. Mechler, R. J. Nichols, S. Praporski, I. L. di Maio, H. Islam, A. P. Girard-Egrot, B. A. Cornell, J. Prashar, F. Caruso, L. L. Martin and D. K. Martin, *Adv. Funct. Mater.*, 2009, **19**, 201-208.

122. J.-i. Anzai, H. Takeshita, Y. Kobayashi, T. Osa and T. Hoshi, *Anal. Chem.*, 1998, **70**, 811-817.

123. T. Hoshi, H. Saiki, S. Kuwazawa, C. Tsuchiya, Q. Chen and J.-i. Anzai, *Anal. Chem.*, 2001, **73**, 5310-5315.

124. E. W. Stein, P. S. Grant, H. Zhu and M. J. McShane, *Anal. Chem.*, 2007, **79**, 1339-1348.

125. E. W. Stein, S. Singh and M. J. McShane, *Anal. Chem.*, 2008, **80**, 1408-1417.

126. G. B. Sukhorukov, E. Donath, H. Lichtenfeld, E. Knippel, M. Knippel, A. Budde and H. Möhwald, *Colloids Surf. A: Physicochem. Eng. Aspects*, 1998, **137**, 253-266.

127. A. A. Antipov, G. B. Sukhorukov, S. Leporatti, I. L. Radtchenko, E. Donath and H. Mohwald, *Colloids Surf. A: Physicochem. Eng. Aspects*, 2002, **198**, 535-541.

128. J. Park and M. McShane, in *IEEE Sensors 2008*, IEEE, 2008, 562-565.

129. T. Crouzier, T. Boudou and C. Picart, *Current Opinion in Colloid & Interface Science*, 2010, **15**, 417-426.

130. C. J. Ochs, G. K. Such and F. Caruso, *Langmuir*, 2010, **27**, 1275-1280.

131. M. A. Pechenkin, H. Mohwald and D. V. Volodkin, *Soft Matter*, 2012, **8**, 8659-8665.

132. E. W. Stein, P. S. Grant, H. Zhu and M. J. McShane, *Anal. Chem.*, 2007, **79**, 1339-1348.

133. E. W. Stein, S. Singh and M. J. McShane, *Anal. Chem.*, 2008, **80**, 1408-1417.

134. X. Qiu, E. Donath and H. Möhwald, *Macromolecular Materials and Engineering*, 2001, **286**, 591-597.

135. A. T. Nagaraja, S. Pradhan and M. J. McShane, *J. Colloid Interface Sci.*, 2014, **418**, 366-372.

136. H. Cölfen and M. Antonietti, *Langmuir*, 1998, **14**, 582-589.

137. A. I. Petrov, D. V. Volodkin and G. B. Sukhorukov, *Biotechnol. Progr.*, 2005, **21**, 918-925.

138. G. B. Sukhorukov, D. V. Volodkin, A. M. Gunther, A. I. Petrov, D. B. Shenoy and H. Mohwald, *J. Mater. Chem.*, 2004, **14**, 2073-2081.

139. A. I. Petrov, D. V. Volodkin and G. B. Sukhorukov, *Biotechnol. Progr.*, 2005, **21**, 918-925.

140. D. V. Volodkin, N. I. Larionova and G. B. Sukhorukov, *Biomacromolecules*, 2004, **5**, 1962-1972.

141. D. V. Volodkin, A. I. Petrov, M. Prevot and G. B. Sukhorukov, *Langmuir*, 2004, **20**, 3398-3406.

142. W. J. Tong, W. F. Dong, C. Y. Gao and H. Mohwald, *J. Phys. Chem. B*, 2005, **109**, 13159-13165.

143. C. Y. Wang, C. Y. He, Z. Tong, X. X. Liu, B. Y. Ren and F. Zeng, *Int. J. Pharm.*, 2006, **308**, 160-167.

144. D. Halozan, U. Riebentanz, M. Brumen and E. Donath, *Colloid Surf. A-Physicochem. Eng. Asp.*, 2009, **342**, 115-121.

145. L. I. Kazakova, L. I. Shabarchina and G. B. Sukhorukov, *PCCP*, 2011, **13**, 11110-11117.

146. Z. X. Zhao, X. S. Wang, X. Qin, Q. Chen and J. Anzai, *Materials Science & Engineering C-Materials for Biological Applications*, 2012, **32**, 569-573.

147. A. A. Antipov, G. B. Sukhorukov, E. Donath and H. Möhwald, *The Journal of Physical Chemistry B*, 2001, **105**, 2281-2284.

148. D. Halozan, U. Riebentanz, M. Brumen and E. Donath, *Colloids Surf. A: Physicochem. Eng. Aspects*, 2009, **342**, 115-121.

149. M. McShane and D. Ritter, *J. Mater. Chem.*, 2010, **20**, 8189-8193.

150. D. Volodkin, *Adv. Colloid Interface Sci.*, 2014, **207**, 306-324.

151. R. A. White, L. Nolan, D. Harley, J. Long, S. Klein, K. Tremper, R. Nelson, J. Tabrisky and W. Shoemaker, *The American Journal of Surgery*, 1982, **144**, 68-75.

152. P. Byrne, *Annals of Surgery*, 1984, **200**, 159-165.

153. D. C. Klonoff, *Diabetes Care*, 2005, **28**, 1231-1239.

154. J. S. Skyler, I. A. Lasky, D. L. Skyler, E. G. Robertson and D. H. Mintz, *Diabetes Care*, 1978, **1**, 150-157.

155. P. H. Sönksen, S. L. Judd and C. Lowy, *The Lancet*, 1978, **311**, 729-732.

156. W. V. Tamborlane, R. W. Beck, B. W. Bode, B. Buckingham, H. P. Chase, R. Clemons, R. Fiallo-Scharer, L. A. Fox, L. K. Gilliam, I. B. Hirsch, E. S. Huang, C. Kollman, A. J. Kowalski, L. Laffel, J. M. Lawrence, J. Lee, N. Mauras, M. O'Grady, K. J. Ruedy, M. Tansey, E. Tsalikian, S. Weinzimer, D. M. Wilson, H. Wolpert, T. Wysocki and D. Xing, *The New England Journal of Medicine*, 2008, **359**, 1464-1476.

157. T. D. C. a. C. T. R. Group, *New Engl. J. Med.*, 1993, **329**, 977-986.

158. Y. Onuki, U. Bhardwaj, F. Papadimitrakopoulos and D. J. Burgess, *Journal of Diabetes Science and Technology*, 2008, **2**, 1003-1015.

159. S. Vaddiraju, D. J. Burgess, I. Tomazos, F. C. Jain and F. Papadimitrakopoulos, *Journal of Diabetes Science and Technology*, 2010, **4**, 1540-1562.

160. J. C. Pickup, F. Hussain, N. D. Evans, O. J. Rolinski and D. J. S. Birch, *Biosens. Bioelectron.*, 2005, **20**, 2555-2565.

161. O. S. Wolfbeis, *J. Mater. Chem.*, 2005, **15**, 2657-2669.

162. R. J. McNichols and G. L. Cote´, *J. Biomed. Opt.*, 2000, **5**, 5-16.

163. S. A. Vinogradov, L. W. Lo, W. T. Jenkins, S. M. Evans, C. Koch and D. F. Wilson, *Biophys. J.*, 1996, **70**, 1609-1617.

164. D. F. Wilson, W. M. F. Lee, S. Makonnen, O. Finikova, S. Apreleva and S. A. Vinogradov, *J. Appl. Physiol.*, 2006, **101**, 1648-1656.

165. D. Wilson, O. Finikova, A. Lebedev, S. Apreleva, A. Pastuszko, W. F. Lee and S. Vinogradov, in *Oxygen Transport to Tissue XXXII*, eds. J. C. LaManna, M. A. Puchowicz, K. Xu, D. K. Harrison and D. F. Bruley, Springer, New York, NY 2011, 53-59.

166. J. R. Lakowicz, *Principles of Fluorescence Spectroscopy*, Springer, New York, NY, 2007, 97-155.

167. J. R. Roberts, J. Park, K. Helton, N. Wisniewski and M. McShane, *Journal of Diabetes Science and Technology*, 2012, **6**, 1267–1275.

168. J. Q. Brown, R. Srivastava and M. J. McShane, *Biosens. Bioelectron.*, 2005, **21**, 212-216.

169. M. Fang, P. S. Grant, M. J. McShane, G. B. Sukhorukov, V. O. Golub and Y. M. Lvov, *Langmuir*, 2002, **18**, 6338-6344.

170. J. Roberts, B. B. Collier and M. J. McShane, in *2011 IEEE Sensors*, IEEE, 2011, 1245-1248.

171. S. M. Borisov and O. S. Wolfbeis, *Chem. Rev.*, 2008, **108**, 423-461.

172. G. S. Wilson and R. Gifford, *Biosens. Bioelectron.*, 2005, **20**, 2388-2403.

173. K. J. Ziegler, *Trends Biotechnol.*, 2005, **23**, 440-444.

174. J. Jaremko and O. Rorstad, *Diabetes Care*, 1998, **21**, 444-450.

175. M. C. Frost and M. E. Meyerhoff, *Curr. Opin. Chem. Biol.*, 2002, **6**, 633-641.

176. G. M. Lemperle, Vera B.; Pestonjamasp, Vasumati; Gallo, Richard L., *Plastic & Reconstructive Surgery*, 2004, **113**, 1380-1390.

177. J. J. G. Marler, Amrita; Rowley, Jonathan B.S.; Koka, Rahul B.S.; Mooney, David; Upton, Joseph; Vacanti, Joseph P., *Plastic & Reconstructive Surgery*, 2000, **105**, 2049-2058.

178. D. Verdoes, R. C. Van Landschoot and G. M. Van Rosmalen, *J. Cryst. Growth*, 1990, **99**, 1124-1129.

179. A. Romoser, D. Ritter, R. Majitha, K. E. Meissner, M. McShane and C. M. Sayes, *PLoS ONE*, 2011, **6**, e22079.

180. H. U. Bergmeyer, K. Gawehn and M. Grassl, *Methods of Enzymatic Analysis*, Academic Press, New York, NY, 1974, 574-690.

181. J. J. Harris, J. L. Stair and M. L. Bruening, *Chem. Mater.*, 2000, **12**, 1941-1946.

182. K. S. Anseth, C. N. Bowman and L. Brannon-Peppas, *Biomaterials*, 1996, **17**, 1647-1657.

183. N. A. Peppas, *J. Bioact. Compatible Polym.*, 1991, **6**, 241-246.

184. H. H. Winter and F. Chambon, *Journal of Rheology*, 1986, **30**, 367-382.

185. H. H. Winter, *Polymer Engineering & Science*, 1987, **27**, 1698-1702.

186. C. L. Bell and N. A. Peppas, *Polymer Engineering & Science*, 1996, **36**, 1856-1861.

187. J. E. Babensee, J. M. Anderson, L. V. McIntire and A. G. Mikos, *Adv. Drug Del. Rev.*, 1998, **33**, 111-139.

188. J. M. Anderson, *Annual Review of Materials Research*, 2001, **31**, 81-110.

189. N. Annabi, J. W. Nichol, X. Zhong, J. Chengdong, S. Koshy and A. Khademhosseini, *Tissue Engineering Part B: Reviews*, 2010, **16**, 371-383.

190. H. Fujita, *Fortschritte der Hochpolymeren-Forschung*, 1961, **3**, 1-47.

191. R. G. W. Davidson III and N. A. Peppas, *J. Controlled Release*, 1986, **3**, 243-258.

192. S. Jeck, P. Scharfer, W. Schabel and M. Kind, *J. Membr. Sci.*, 2012, **389**, 162-172.

193. A. Keller and S. Z. D. Cheng, *Polymer*, 1998, **39**, 4461-4487.

194. S. Candau, J. Bastide and M. Delsanti, in *Polymer Networks*, ed. K. Dušek, Springer, Berlin, 1982, 27-71.

195. M. J. McShane, J. Q. Brown, K. B. Guice and Y. M. Lvov, *Journal of Nanoscience and Nanotechnology*, 2002, **2**, 411-416.

196. S. Singh and M. McShane, *Biosens. Bioelectron.*, 2010, **25**, 1075-1081.

197. B. B. Collier and M. J. McShane, *Proc. SPIE*, 2013, **8591**, pp. 859104-859108.

198. J. D. Mendelsohn, C. J. Barrett, V. V. Chan, A. J. Pal, A. M. Mayes and M. F. Rubner, *Langmuir*, 2000, **16**, 5017-5023.

199. S. S. Shiratori and M. F. Rubner, *Macromolecules*, 2000, **33**, 4213-4219.

200. J. Park and M. McShane, in *IEEE Sensors 2009*, IEEE, 2009, 1208-1211.

201. J. Park, Transport-Controlling Nanoscale Multilayers for Biomedical Devices, Doctoral dissertation, Texas A&M University, College Station, 2011.

202. D. Zhao, R.-X. Zhuo and S.-X. Cheng, *Molecular BioSystems*, 2012, **8**, 753-759.

203. W. Jin, A. Toutianoush and B. Tieke, *Appl. Surf. Sci.*, 2005, **246**, 444-450.

204. B. B. Collier and M. McShane, *IEEE Sens. J.*, 2014, **PP**, 943-946.

205. K. Rebrin, G. M. Steil, W. P. van Antwerp and J. J. Mastrototaro, *Am. J. Physiol.*, 1999, **277**, E561-E571.

206. E. Kulcu, J. A. Tamada, G. Reach, R. O. Potts and M. J. Lesho, *Diabetes Care*, 2003, **26**, 2405-2409.

207. S. Ali, Finite Element Modeling of Dermally-implanted Enzymatic Microparticle Glucose Sensors, Master's thesis, Texas A&M University, College Station, 2011.

208. J. K. Leypoldt and D. A. Gough, *Anal. Chem.*, 1984, **56**, 2896-2904.

209. S. Singh, Enhancement of the Response Range and Longevity of Microparticle-based Glucose Sensors, Doctoral dissertation, Texas A&M University, College Station, 2010.

210. X. Hu, T. Wang, L. Wang and S. Dong, *The Journal of Physical Chemistry C*, 2007, **111**, 6962-6969.

APPENDIX A

AUTOMATED ANALYSIS FOR OXYGEN AND GLUCOSE SENSORS

Automated code was utilized to quickly analyze large quantities of data produced by the custom time domain lifetime system for oxygen and glucose experiments. The code, written in MatLab script, is shown below. Each part of the code is explained in line with comments marked using the "%" symbol and is displayed in green.

A.1 Two-site Stern Volmer fitting code for oxygen sensors

```
%%%%
%MPA O2 Sensor Analysis
%%%
clear all
close all
%%File Names
BL=cellstr(['5 '; '10'; '15'; '20'; '25'; '30']); %file designations referring to the number of
bilayers in sample
air=cellstr(['GG  '; '10% '; '25% '; '50% '; '100%']); %file designations referring to the
concentration of air bubbled in the reservoir
samp=cellstr(['1'; '2'; '3']); %file designations referring to sample number
filepath='filepath';
%%Oxygen values
O2equil=  208.7; %Corrected O2 concentration (uM) at equilibrium (37C and
1.3%salinity)
O2=[0,.1, .25, .5, 1]*O2equil; %Corrected O2 concentration array
%%Loading and averaging raw data
for i=1:length(BL)
   for j=1:length(air)
      for k=1:length(samp)
      loadfile = strcat(filepath, '\', char(BL(i,1)), 'BL3x', char(air(j,1)), '-s',
char(samp(k,1)),'.xls'); %read data file
      data = dlmread(loadfile);
      for a=length(data):-1:length(data)-30
         lt(length(data)-a+1,k)=data(a,4); %resize data matrix, cutting out extra cells
```

```
        end
        ltavg(j,k)=mean(lt(:,k)); %calculate the mean lifetime at a single oxygen
concentration within a sample
        end

        BLavg(i,j)=mean(ltavg(j,:)); %mean array containing each sample type and oxygen
concentration
        BLconf(i,j)=std(ltavg(j,:))*1.96/3^.5;%confidence interval for each mean


    end

%%Two-site SV fit:
        ft = fittype( '((f/(1+Ksv1*x))+((1-f)/(1+Ksv2*x)))^-1', 'independent', 'x', 'dependent',
'y' ); %fit equation defined
        opts = fitoptions( ft );
        opts.StartPoint = [1 0.002 0.8]; %initial guesses for parameters
        opts.Lower = [0 0 0]; %lower bounds for parameters
        opts.Upper = [Inf Inf 1]; %upper bounds for parameters
        fitresult= fit( O2', tinv(:,k), ft, opts );
        plot(fitresult)
        Ksv1(i,k)=fitresult.Ksv1; %Ksv1 values in array
        Ksv2(i,k)=fitresult.Ksv2; %Ksv2 values in array
        f(i,k)=fitresult.f; %f value in array

        end
        SVavg(:,i)=mean(SV(i,:));
        SVconf(:,i)=std(SV(i,:))*1.96/3^0.5;
    save(savefile);
    tinvtot{1,i}=tinv;

end
%Calculate means and confidence intervals for two-site parameters
Ksv1conf=(std(Ksv1')*1.96/3^0.5)';
Ksv2conf=(std(Ksv2')*1.96/3^0.5)';
fconf=(std(f')*1.96/3^0.5)';
Ksv1avg=mean(Ksv1,2);
Ksv2avg=mean(Ksv2,2);
favg=mean(f,2);
```

A.2 Figure of merit analysis code for glucose sensors

A.2.1 Raw data input and response calculations

```
%%%%%
%Raw data input and response calculations
%%%%%
clear all
close all
clc
file = 'filepath';
fn = 'filename'
data = dlmread([file '\' fn '.xls']); %Load raw data from instrument output file
for i=2:length(data)
data(i,1)=data(i-1,1)+10;
end
lt = data(:,4)'; %Lifetime data
i1 = data(:,5)'; %Intensity data
c = data(:,3)'; %Concentration data
time = data(:,1)'; %Time data
time = time./3600; %Convert time to hours from seconds
int_t = 0.1; %Use last 0.1 hours as steady state response
samp_t = 15; %Seconds between samples
num = int_t*3600/samp_t; %Determines number of measurements in steady state
response time

conc(1) = data(1,3); %First concentration
for i=1:length(data(:,3))
   if(conc(length(conc))~=data(i,3))
      conc(length(conc)+1)=data(i,3); %Generates concentrations utilized
   end
end
 c = data(:,3)';
j=1;
for i=1:length(c)-1
   if(c(i)~=c(i+1))
      index2(j) = i; %Determines at what point concentrations change
      index1(j) = i-num;
      j=j+1; %Logs place in array
   end
end
index2(j) = i;
index1(j) = i-num;
[M, F] = mode(conc);
```

```
row = F-1;
col = ceil(length(conc)/row);
k=1;
for i=1:row %For each concentration and number of runs, determine average lifetime
and standard deviation for values in the steady state (determined by index1 and index2)
   for j=1:col
      values = lt(index1(k):index2(k));
      m(i, j) = mean(values);
      n(i, j)=length(values);
      st(i, j)=std(values);
      e(i, j)=st(i)/sqrt(n(i));
      k = k+1;
   end
   k=k-1;
end
for i=1:row%Determine the percent change for each concentration at steady state
   for j=1:col
      p(i, j)=(m(i, j)-m(i, 7))/m(i, 1)*100;
      pst(i, j) = ((st(i, j)+m(i, j))-m(i, 7))/m(i, 7)*100-p(i, j);
   end
end
clear c
```

A.2.2 Concentration analysis

```
%%%%%%
%Glucose sensor analysis based upon concentration
%%%%%%
clear all
close all
clc


%Find number of files
set(0,'DefaultFigureWindowStyle','docked')
r=0;
nfile = 'filepath';
for k=1:10
    fn=['MPA 30 BL ' num2str(k) 'x 1.mat'];
    q=[nfile '\' fn];
    if(~exist(q))
        break;
    end
    r=r+1;
end
z=zeros(r,5);
for s=1:r
    for j=1:5
    fn1 = ['MPA 30 BL ' num2str(s) 'x ' num2str(j) '.mat'];
    q1= [nfile '\' fn1];
    if(~exist(q1))
        break;
    end
    z(s,j)=1;
end
end
%%Load files
for w=1:r
for y=1:sum(z((w),:))
    fn =  ['MPA 30 BL ' num2str(w) 'x ' num2str(y) '.mat'];
     q= [nfile '\' fn];
    load(q);
    MPA(y,:) = m; %Lifetime values
    MPAst(y,:)=st; %Standard deviation in lifetime
    c1(y,:)=c; %Glucose concentrations
    MPAp(y,:)=p; %Percent change
    MPAstp(y,:)=pst; %Standard deviation in percent change
```

```
    %insert fit
    [xData, yData] = prepareCurveData( c, m );

%%Set up sigmoidal fit and options.
    ft = fittype( 'a/(1+b*exp(c*x))+d', 'independent', 'x', 'dependent', 'y' );
    opts = fitoptions( ft );
    opts.Display = 'Off';
    opts.Lower = [-1000 0 0 0];
    opts.StartPoint = [-300 0.6 0.02 300];
    opts.Upper = [0 10 5 1000];

%%Fit model to data
    [fitresult, gof] = fit( xData, yData, ft, opts );

%%Response time calculations
    lt = data(:,4);%Load lifetime
    i1 = data(:,5)';%Load glucose concentrations
    c = data(:,3)';
    time = data(:,1);%Load time data
    time = time./3600;%Change time to hours
    moveavgpt=20;%Determine number of points to average in moving average
%%Smoothing spline for RAW
    [xData, yData] = prepareCurveData(time, lt);

    % Set up fittype and options.
    ft = fittype( 'smoothingspline' );%Smooth curve for response time analysis
    opts = fitoptions( ft );
    opts.SmoothingParam = 0.999999;

    % Fit model to data.
    [fitresult2, gof] = fit( xData, yData, ft, opts );
    y1= feval(fitresult2,time);
%%Determine response time
    for e=1:length(index2)-2%index2 represents where concentrations change in time
    for v=1:length(y1)
        if v+index2(1,e)+moveavgpt/2 > length(y1)%Breaks code if limit in length reached
(no solution)
            start=index2(1,e);
        break
        end
        moveavg=sum(y1(v+index2(1,e)-
(moveavgpt/2):(v+index2(1,e)+(moveavgpt/2)),1))/moveavgpt;
        if moveavg > 3*st(1,e)+y1(index2(1,e),1)%If value in lifetime exceed three times
the standard deviation of the previous average lifetime, set as start of response
```

```
            start=v+index2(1,e);

        break
        end
    end
     for en=1:length(y1)
        if en+index2(1,e)+moveavgpt/2 > length(y1)%Breaks code if limit in length
reached (no solution)
            ends=index2(1,e);
            break
        end
        moveavg2=sum(y1(en+start-
(moveavgpt/2):(en+start+(moveavgpt/2)),1))/moveavgpt;
        if moveavg2 > m(1,e+1)-3*st(1,e+1)%If lifetime approaches 3 times the standard
deviation below the next average lifetime, call this the end point
            ends=en+start;

        break
        end
     end
     tr(1,e)=time(ends,1)-time(start,1);%Response time is determined as the difference in
time of the end and start points
     resp(y,w)={tr};
    end


%%FOM calcs
    MPAmax(y,w)=fitresult.d; %Highest lifetime value (asymtote)
    sigmabase3(y,w)=st(1,1)*3; %Standard deviation in baseline
    sigmatop3(y,w)=st(1,6)*3; %Standard deviation at highest glucose concentration
    baseline(y,w)=(m(1,1)+m(1,7))/2; %Averaged baseline lifetime values (before and
after glucose)
    LODy(y,w)=baseline(y,w)+sigmabase3(y,w); %Limit of detection y coordinate
    LOD(y,w)=log(((fitresult.a/(LODy(y,w)-fitresult.d))-1)/fitresult.b)/fitresult.c;
%Corresponding limit of detection
    ARtopy(y,w)=fitresult.d-sigmatop3(y,w); %Top of the analytical range y coordinate
    ARtop(y,w)=log(((fitresult.a/(ARtopy(y,w)-fitresult.d))-1)/fitresult.b)/fitresult.c;
%corresponding top of analytical range
    AR(y,w)=ARtop(y,w)-LOD(y,w); %Analytical range
    sense(y,w)=((ARtopy(y,w)-LODy(y,w))/LODy(y,w)*100)/AR(y,w);%Sensitivity
end


%%Log data per sample
```

```
MPAm(w,:) = mean(MPA); %Mean lifetime values at each glucose concentration and
sample type
MPAstm(w,:)=std(MPA);%Standard deviation of mean lifetime values at each glucose
concentration and sample type
MPAconf(w,:)=std(MPA)*(1.96/(sum(z((w),:))).^.5);%95% confidence intervals of
mean lifetime values at each glucose concentration and sample type

MPAmp(w,:)=mean(MPAp);%Mean percent change values at each glucose
concentration and sample type
MPAstmp(w,:)=MPAstm(w,:)/MPAm(1,1)*100;%Standard deviation of percent change
values at each glucose concentration and sample type
MPAconfp(w,:)=MPAconf(w,:)/MPAm(w,1)*100;%95% confidence intervals of percent
change values at each glucose concentration and sample type


clear MPA MPAst MPAp MPAstp
end
%%initial response time calculations
clear c1
for i=1:5
    c1(i,:)=resp{i,5}*60; %concentration 1x response times
    c2(i,:)=resp{i,4}*60;  %concentration 2x response times
    c3(i,:)=resp{i,3}*60; %concentration 3x response times
    c4(i,:)=resp{i,2}*60; %concentration 4x response times
    c5(i,:)=resp{i,1}*60; %concentration 5x response times
end
c1m=mean(c1,1); %Mean response times
c2m=mean(c2,1);
c3m=mean(c3,1);
c4m=mean(c4,1);
c5m=mean(c5,1);

c1s=std(c1,1); %Standard deviation of response times
c2s=std(c2,1);
c3s=std(c3,1);
c4s=std(c4,1);
c5s=std(c5,1);

c1conf=std(c1,1)*1.96/(5^0.5); %95% confidence intervals of response times
c2conf=std(c2,1)*1.96/(5^0.5);
c3conf=std(c3,1)*1.96/(5^0.5);
c4conf=std(c4,1)*1.96/(5^0.5);
c5conf=std(c5,1)*1.96/(5^0.5);
```

```
initresp(1,1)=c1m(1,1); %Mean initial response times
initresp(1,2)=c2m(1,1);
initresp(1,3)=c3m(1,1);
initresp(1,4)=c4m(1,1);
initresp(1,5)=c5m(1,1);

initrespconf(1,1)=c1conf(1,1); %95% confidence intervals of initial response times
initrespconf(1,2)=c2conf(1,1);
initrespconf(1,3)=c3conf(1,1);
initrespconf(1,4)=c4conf(1,1);
initrespconf(1,5)=c5conf(1,1);

%%Means and confidence intervals for figures of merit
LODavg=mean(LOD,1); %Limit of detection means
LODconf=std(LOD,1)*1.96/5^0.5;%Limit of detection 95% confidence intervals
ARtopavg=mean(ARtop,1);
ARtopconf=std(ARtop,1)*1.96/5^0.5;
senseavg=mean(sense,1);%Mean sensitivities
senseconf=std(sense,1)*1.96/5^0.5;
ARavg=mean(AR);
ARconf=std(AR)*1.96/5^0.5;
```

A.2.3 Bilayer analysis

```
%%%%%%
%Glucose sensor analysis based upon bilayer numbers
%%%%%%
clear all
close all
clc


%%Find files of data
set(0,'DefaultFigureWindowStyle','docked')
r=0;
nfile = 'filepath';
z=zeros(r,6);
aa=0;
for s=1:6 %
    h=35-s*5;
    aa=aa+1;
    for j=1:5
    fn1 = ['MPA ' num2str(h) ' BL 3x ' num2str(j) '.mat'];
    q1= [nfile '\' fn1];
```

```
    if(~exist(q1))
        break;
    end
    z(aa,j)=1;
end
end
b=0;
%%Load files
for w=1:size(z,1)
    g=35-w*5;
    b=b+1;
for y=1:sum(z((b),:))
    fn =  ['MPA ' num2str(g) ' BL 3x ' num2str(y) '.mat'];
     q= [nfile '\' fn];
    load(q);
    MPA(y,:) = m;%Lifetime values
    MPAst(y,:)=st;%Standard deviation in lifetime
    c1(y,:)=c;%Glucose concentrations
    MPAp(y,:)=p;%Percent change
    MPAstp(y,:)=pst;;%Standard deviation in percent change
%%Set up sigmoidal fit and options.
    [xData, yData] = prepareCurveData( c, m );
    ft = fittype( 'a/(1+b*exp(c*x))+d', 'independent', 'x', 'dependent', 'y' );
    opts = fitoptions( ft );
    opts.Display = 'Off';
    opts.Lower = [-1000 0 0 0];
    opts.StartPoint = [-300 0.6 0.02 300];
    opts.Upper = [0 10 5 1000];

    % Fit model to data.
    [fitresult, gof] = fit( xData, yData, ft, opts );

%%Response time calculations
    lt = data(:,4);%Load lifetime data
    c = data(:,3)';%Load glucose concentrations
    time = data(:,1);%Load time data
    time = time./3600;%Convert time to hours
    moveavgpt=20; %Number of points in moving average
    %Smoothing spline for raw data
    [xData, yData] = prepareCurveData(time, lt);

    % Set up fittype and options.
    ft = fittype( 'smoothingspline' );
    opts = fitoptions( ft );
```

```
    opts.SmoothingParam = 0.999999;

    % Fit model to data.
    [fitresult2, gof] = fit( xData, yData, ft, opts );
    y1= feval(fitresult2,time);
    %%Determine start and end times for response changes
    for e=1:length(index2)-2
    for v=1:length(y1)
        moveavg=sum(y1(v+index2(1,e)-
(moveavgpt/2):(v+index2(1,e)+(moveavgpt/2)),1))/moveavgpt;
        if moveavg > 3*st(1,e)+y1(index2(1,e),1) %If lifetime exceed three times the
standard deviation of the previous mean lifetime, set as start of response
            start=v+index2(1,e);

        break
        end
    end
     for en=1:length(y1)
        moveavg2=sum(y1(en+start-
(moveavgpt/2):(en+start+(moveavgpt/2)),1))/moveavgpt;
        if moveavg2 > m(1,e+1)-3*st(1,e+1)%If lifetime exceeds the next mean lifetime
value minus three times the standard deviation of that mean , set as end of response
            ends=en+start;

        break
        end
     end
     tr(1,e)=time(ends,1)-time(start,1);%Response is the difference in time from the star
tto the end of response
     resp(y,w)={tr};
    end


%%FOM calcs
    MPAmax(y,w)=fitresult.d;%Highest lifetime value (asymptote)
    sigmabase3(y,w)=st(1,1)*3;%Standard deviation in baseline
    sigmatop3(y,w)=st(1,6)*3;%Standard deviation at highest glucose concentration
    baseline(y,w)=(m(1,1)+m(1,7))/2;%Averaged baseline lifetime values (before and
after glucose)
    LODy(y,w)=baseline(y,w)+sigmabase3(y,w);%Limit of detection y coordinate
    LOD(y,w)=log(((fitresult.a/(LODy(y,w)-fitresult.d))-
1)/fitresult.b)/fitresult.c;%Corresponding limit of detection
    ARtopy(y,w)=fitresult.d-sigmatop3(y,w);%Top of the analytical range y coordinate
```

```
    ARtop(y,w)=log(((fitresult.a/(ARtopy(y,w)-fitresult.d))-
1)/fitresult.b)/fitresult.c;%Corresponding top of analytical range
    AR(y,w)=ARtop(y,w)-LOD(y,w); %Analytical range
    sense(y,w)=((ARtopy(y,w)-LODy(y,w))/LODy(y,w)*100)/AR(y,w);%Sensitivity

end

%%Log data per sample
MPAm(b,:) = mean(MPA);%Mean lifetime values at each glucose concentration and
sample type
MPAstm(b,:)=std(MPA);%Standard deviation of mean lifetime values at each glucose
concentration and sample type
MPAconf(b,:)=std(MPA)*(1.96/(sum(z((b),:))).^.5);%95% confidence intervals of mean
lifetime values at each glucose concentration and sample type

MPAmp(b,:)=mean(MPAp);%Mean percent change values at each glucose
concentration and sample type
MPAstmp(b,:)=MPAstm(b,:)/MPAm(1,1)*100;%Standard deviation of percent change
values at each glucose concentration and sample type
MPAconfp(b,:)=MPAconf(b,:)/MPAm(b,1)*100;%95% confidence intervals of percent
change values at each glucose concentration and sample type

sampnum(b,1)=sum(z((b),:));
clear MPA MPAst MPAp MPAstp
end
for i=1:5
    b5(i,:)=resp{i,6}*60; %5BL response times
    b10(i,:)=resp{i,5}*60; %10BL response times
    b15(i,:)=resp{i,3}*60; %15BL response times
    b20(i,:)=resp{i,3}*60; %20BL response times
    b25(i,:)=resp{i,2}*60; %25BL response times
    b30(i,:)=resp{i,1}*60; %30BL response times
end
b5m=mean(b5,1); %Mean response times
b10m=mean(b10,1);
b15m=mean(b15,1);
b20m=mean(b20,1);
b25m=mean(b25,1);
b30m=mean(b30,1);

b5s=std(b5,1); %Standard deviation of response times
b10s=std(b10,1);
b15s=std(b15,1);
b20s=std(b20,1);
```

```
b25s=std(b25,1);
b30s=std(b30,1);

b5conf=std(b5,1)*1.96/(5^0.5); %95% confidence intervals of response times
b10conf=std(b10,1)*1.96/(5^0.5);
b15conf=std(b15,1)*1.96/(5^0.5);
b20conf=std(b20,1)*1.96/(5^0.5);
b25conf=std(b25,1)*1.96/(5^0.5);
b30conf=std(b25,1)*1.96/(5^0.5);

initresp(1,1)=b5m(1,1); %Mean initial response times
initresp(1,2)=b10m(1,1);
initresp(1,3)=b15m(1,1);
initresp(1,4)=b20m(1,1);
initresp(1,5)=b25m(1,1);
initresp(1,6)=b30m(1,1);

initrespconf(1,1)=b5conf(1,1); %95% confidence intervals of initial response times
initrespconf(1,2)=b10conf(1,1);
initrespconf(1,3)=b15conf(1,1);
initrespconf(1,4)=b20conf(1,1);
initrespconf(1,5)=b25conf(1,1);
initrespconf(1,6)=b30conf(1,1);

%%Means and confidence intervals for figures of merit
LODavg=mean(LOD,1); %Limit of detection means
LODconf=std(LOD,1)*1.96/5^0.5;%Limit of detection 95% confidence intervals
ARtopavg=mean(ARtop,1);
ARtopconf=std(ARtop,1)*1.96/5^0.5;
senseavg=mean(sense,1);%Mean sensitivities
senseconf=std(sense,1)*1.96/5^0.5;
ARavg=mean(AR);
ARconf=std(AR)*1.96/5^0.5;
```

APPENDIX B

METHODS UTILIZED IN PRELIMINARY WORK

B.1 SERS-based sensing MPACs

B.1.1 Materials

Poly(sodium 4-styrenesulfonate) (PSS, average M_w = 70,000 Da), poly(diallyldimethylammonium chloride) (PDADMAC, typical M_w range = 100,000-200,000Da) , poly(allylamine hydrochloride) (PAH, average M_w = 15,000 Da), poly(sodium 4-styrenesulfonate-*co*-maleic acid) (PSS-*co*-MA, 1:1 monomer ratio, average M_w = 20,000 Da), alginic acid sodium salt from brown algae (281 cps for a 2% aqueous solution at 25 °C), and 4-aminothiophenol (4-ATP), were obtained from Sigma and used without further purification. Citrate-stabilized gold nanoparticles (20nm) were obtained from Nanopartz.

B.1.2 Methods

B.1.2.1 ATP-modified gold

A solution was made by dissolving solid 4-ATP in 200 proof ethanol to a concentration of 0.5 mg/mL. This solution was added to stock gold NP solution at a 1:1 volume ratio. The particles/4-ATP solution was then allowed to react overnight. After reaction, particles were sonicated for 1 hour and washed 3 times by centrifuge filtration using 30 kDa Nanosep (Pall) filters (5,000 g, 2 minutes) and subsequent addition of ethanol. Particles were then centrifuged down a final time (5,000 g, 2 minutes) and resuspended in 5 mM $NaHCO_3$ (pH 8.0).

B.1.2.2 Loading of gold nanoparticles into $CaCO_3$

An aliquot of 400 µL of 4-ATP gold NPs (~2 x 10^{12} particles/mL) was added to 6 mL of 0.2 M Na_2CO_3 in a 20 mL beaker and stirred with a 25 mm triangular stir bar. A 6 mL solution of 0.2 M $CaCl_2$was then added to the gold NP solution under stirring. The mixture was stirred for 30 seconds. Stirring was then ceased and particles were allowed to mature over 10 minutes. Particles were then centrifuged (250 g, 1 minute) and resuspended in 5 mM $NaHCO_3$ buffer at pH 8.0 prior to layer-by-layer deposition.

For LbL coatings, the particle suspension in 1 mL of 5 mM $NaHCO_3$ (pH 8.0) was centrifuged at 500 g for 30 seconds and resuspended in 1 mL 5 mM $NaHCO_3$ (pH 8.0) with 20 mg/mL PDADMAC and allowed to incubate for 30 seconds. The particles were then centrifuged down at 500 g, supernatant removed, and washed once with 1 mL 5 mM $NaHCO_3$ (pH 8.0). The washed particles were centrifuged down again and resuspended in 1 mL 5 mM $NaHCO_3$ (pH 8.0) with 20 mg/mL PSS and allowed to incubate for 30 seconds. This process was repeated until there were 5 bilayers of PDADMAC/PSS. After these layers, PAH and PSS-*co*-MA were deposited. A 1 mL solution of 20 mg/mL PAH in 5 mM $NaHCO_3$ (pH 8.0) was added to the packed particles with 5 bilayers, mixed, and allowed to incubate 30 seconds. Particles were then centrifuged at 500 g and resuspended in 5 mM $NaHCO_3$ (pH 7.2). Washed particles were then centrifuged and resuspended in 5 mM $NaHCO_3$ (pH 7.2) with 20mg/mL PSS-*co*-MA and allowed to incubate 30 seconds. PSS-*co*-MA-coated particles were then centrifuged, washed, and resuspended in 5mM $NaHCO_3$ (pH 8.0). This alternating process was repeated until 10 total bilayers were deposited.

B.1.2.3 MPAC fabrication and testing

To ensure high signal intensity in Raman spectroscopy, highly concentrated MPAC gels (~8x) were fabricated. For each gel, 6.8 mg of 4-ATP-loaded $CaCO_3$ particles were centrifuged down and resuspended in 25 µL DI water. To this solution, 50 µL of 3% (w/v) alginate was added and mixed. A 25 µL solution of GDL (533 mg/mL) was then added to the alginate/$CaCO_3$ solution and mixed well. The resulting pregel solution was immediately deposited into 3 separate wells (20 µL each) in a 30 µL well plate. After gelation, gels were washed 3 times with 10 mM MES buffer (pH 5.7) and examined using a Renishaw System 1000 Raman spectrometer coupled to a Leica DMLM microscope (Schaunberg, IL) for Raman spectral characteristics.

B.2 Drug delivery with MPACs

B.2.1 Materials

Poly(sodium 4-styrenesulfonate) (PSS, average M_w = 70,000 Da), poly(diallyldimethylammonium chloride) (PDADMAC, typical M_w range = 100,000-200,000Da) , poly(allylamine hydrochloride) (PAH, average M_w = 15,000 Da), poly(sodium 4-styrenesulfonate-*co*-maleic acid) (PSS-*co*-MA, 1:1 monomer ratio, average M_w = 20,000 Da), alginic acid sodium salt from brown algae (281 cps for a 2% aqueous solution at 25 °C), rhodamine 101, and rhodamine B isothiocyanate (RITC) were obtained from Sigma and used without further purification. Aminodextran (M_w = 3 kDa) was obtained from Life Technologies.

B.2.2 Methods

B.2.2.1 Aminodextran labeling with rhodamine B

To produce rhodamine B-labeled aminodextran (3 kDa) (RITC-dextran 3k), a simple isothiocyanate reaction was utilized. Aminodextran 3 kDa (50 mg) was added to 10 mL 0.1 M $NaHCO_3$buffer at pH 9.0. To this solution, 35.7 mg RITC was added and stirred at room temperature for 1 hour. Isopropyl alcohol was added until the labeled aminodextran was precipitated. The precipitate was centrifuged, resuspended in a small quantity of water, and precipitated with IPA 5 additional times to remove any excess rhodamine B. The final precipitate was then resuspended in water and lyophilized after flash freezing in liquid nitrogen.

B.2.2.2 Loading of material into $CaCO_3$

$CaCO_3$ microspheres were prepared by precipitation. Briefly, Na_2CO_3 (0.25 M, 8mL) containing either 1 mg/mL rhodamine 101 or RITC-dextran 3k was stirred vigorously in a 25 mL beaker with a 10 mm triangular stirbar. $CaCl_2$ (0.25 M, 8 mL) was then added to the solution under stirring. The solution was stirred for 30 seconds after mixing, and then agitation was removed and the colloid was allowed to rest for 10 minutes thereafter for particle maturation. Particles were then collected, centrifuged and washed in 5 mM Na_2CO_3 pH 8.0 prior to layer-by-layer deposition.

For LbL coatings, the particle suspension in 1 mL of 5 mM $NaHCO_3$ (pH 8.0) was centrifuged at 500 g for 30 seconds and resuspended in 1 mL 5 mM $NaHCO_3$ (pH 8.0) with 20 mg/mL PDADMAC and allowed to incubate for 30 seconds. The particles were then centrifuged down at 500 g, supernatant removed, and washed once with 1 mL

5 mM $NaHCO_3$ (pH 8.0). The washed particles were centrifuged down again and resuspended in 1 mL 5 mM $NaHCO_3$ (pH 8.0) with 20 mg/mL PSS and allowed to incubate for 30 seconds. This process was repeated until desired number of bilayers was acheived (from 0 to 10 for RITC-dextran and 5 for rhodamine 101). For rhodamine 101-loaded particles, additional layers of PAH and PSS-*co*-MA layers were deposited. In this case, a 1 mL solution of 20 mg/mL PAH in 5 mM $NaHCO_3$ (pH 8.0) was added to the packed particles with 5 bilayers, mixed, and allowed to incubate 30 seconds. Particles were then centrifuged at 500 g and resuspended in 5 mM $NaHCO_3$ (pH 7.2). Washed particles were then centrifuged and resuspended in 5 mM $NaHCO_3$ (pH 7.2) with 20 mg/mL PSS-*co*-MA and allowed to incubate 30 seconds. PSS-*co*-MA-coated particles were then centrifuged, washed, and resuspended in 5 mM $NaHCO_3$ (pH 8.0). This alternating process was repeated until the desired number of bilayers was achieved

B.2.2.3 MPAC fabrication and testing

All gels for release testing were manufactured at 1x relative concentration. Gel precursors were made by centrifuging the appropriate amount of $CaCO_3$ particles (3.4 mg), removing the storage buffer (5 mM $NaHCO_3$, pH 8.0), and adding deionized water (200uL). Alginate (400 µL of 3% (w/v) in DI water) was then added and mixed. GDL solution (66 mg/mL, 200 µL) was then added and the solution was mixed vigorously. Aliquots (200 µL) of each gel type were placed in individual well of a 96 well plate and allowed to gel for 24 hours.

After 24 hours of gelation time, 150 µL release buffer (10 mM HEPES, pH 7.4) was then deposited on the surface of the gel. At intermittant time points, 100 µL of

release buffer was taken from the wells and deposited in empty wells. After removal of sample release buffer, the remaining release buffer in the MPAC wells was removed and replaced with 150 µL fresh release buffer. Emission intensity was then read from the sample release buffer using a Tecan model Infinite M200 Pro plate reader to determine quantity of released material.